PAUL SCHERRER INSTITUT

PSI

Annual Report 2004

Electrochemistry Laboratory

http://ecl.web.psi.ch

Cover Photo

Center: HY-LIGHT on the formula 1 race track in Shanghai on the occasion of the Challenge Bibendum 2004.

Left: Microstructured flow field for a micro fuell cell.

PAUL SCHERRER INSTITUT

Electrochemistry Laboratory

Annual Report 2004

With excerpts from the 2004 Annual Scientific Report of
the PSI Research Department General Energy (ENE)

Hardcopies of this report are available from:
Isabella Kalt (isabella.kalt@psi.ch)
Paul Scherrer Institut
5232 Villigen PSI
Switzerland

A full version of this report is also available on the web:
http://ecl.web.psi.ch

Paul Scherrer Institut
Electrochemistry Laboratory
5232 Villigen PSI
Switzerland

Secretary
Phone +41 (0)56 310 29 19
Fax +41 (0)56 310 44 15

TABLE OF CONTENTS

EDITORIAL

Günther G. Scherer

"The result of the HY-LIGHT Project is a real highlight". This was the comment of Prof. Dr. Louis Schlapbach, Director of the Swiss Federal Laboratories for Materials Testing and Research (EMPA) and Member of the PSI General Energy Research Department's Research Advisory Committee on the occasion of its Annual Meeting on October 25, 2004.

Indeed, only two weeks earlier on the occasion of Challenge Bibendum at Shanghai, China, the result of Paul Scherrer Institut's collaboration with our industrial partner Construction Développment Michelin (CDM), Switzerland, was presented and reached attention in the scientific community around the world. A light weight 4-seater car had been presented with a hybrid configuration for the power train, comprising a H_2/O_2 fuel cell and a supercapacitor. Considerable progress could be demonstrated with this car with respect to fuel consumption (less than 2.5 l gasoline equivalent/ 100 km, NEFZ) and range of around 400 km.

This less than two years development could only be achieved on the basis of the Laboratory's broad expertise on electrochemical energy conversion and storage devices, covering materials research, cell design, and systems development, which had been built-up over several years.

In addition, the Electrochemistry Laboratory continuously provides expertise and innovative solutions in the fields of batteries, fuel cells, supercapacitors, electrolysis, electrocatalysis, electrochemical material science, and modern methods for electrochemical interface analysis. With this particular research effort Paul Scherrer Institut's Electrochemistry Laboratory, as the leading institution in this area in Switzerland, contributes to the long-term development of zero emission converters and energy storage systems in the context of a sustainable development.

Besides the HY-LIGHT Project, many other projects were addressed within the frame of our five research groups Fuel Cells, Fuel Cell Systems, Batteries, Capacitors, and Materials. The 40 contributions within this Annual Report highlight these research efforts and their results.

Our involvement in PSI's large facilities, like SINQ or SLS, is steadily increasing, including the design and construction of the IR-beamline at SLS through co-workers of the Electrochemistry Laboratory.

Again, we look back to a successful year of collaborations with industrial partners. With many of them, we will continue our joint efforts also during the upcoming year 2005. Due to the fact that many of these collaborations have medium-term goals; results will be published in the future. Nevertheless, we record close to 50 peer-reviewed publications contributed to the scientific literature by colleagues of the Electrochemistry Laboratory.

During the past year, we organized two of our successful international One-Day-Symposia on topics of electrochemical R&D. The 19th Symposium, held on January 16, addressed topics in the area of "Advanced Characterization Methods for Electrochemical Cells" with contributions from K. Edström (Uppsala), O. Haas, (Villigen), D. Fermín (Bern), J. Behm (Ulm), N. Wagner (Stuttgart), and D. Landolt (Lausanne). On September 15, we celebrated our 20th Symposium with 6 speakers delivering lectures to the general topic "Novel Trends in Electrochemistry". F. Endres (Clausthal) discussed Ionic liquids as novel solvents for electrochemistry. New possibilities using mesoscopic systems in electrochemistry and photoelectrochemistry were presented by M. Grätzel (Lausanne). U. Stimming (München) and N. Alonso-Vante (Poitiers) covered nanoscale effects in electrochemistry and electrocatalysis. Intriguing results and challenges in electrochemical microstructuring were presented by R. Schuster (Berlin) and M. Rohnke (Giessen) introduced the rather novel field of electrochemistry in plasmas.

In particular, these events allow us to invite internationally renowned colleagues, to present to them the facilities and activities of the laboratory, and most important, to establish personal contacts.

As a further means of education, in particular to our 20 PhD-students, serves our Monday's Electrochemistry Seminar, with 39 presentations during the last year, including 11 external speakers.

We can look back to a successful year 2004. Also during the up-coming year 2005 we will make our contributions to the field of Electrochemistry and strengthen our collaborations with industrial partners. Education of students in our scientific area is an equally important and continuing task. Sustainable Energy Development has been identified by the Domain of the Swiss Federal Institutes of Technology as an utmost important goal and we are committed to contribute our share to a successful outcome.

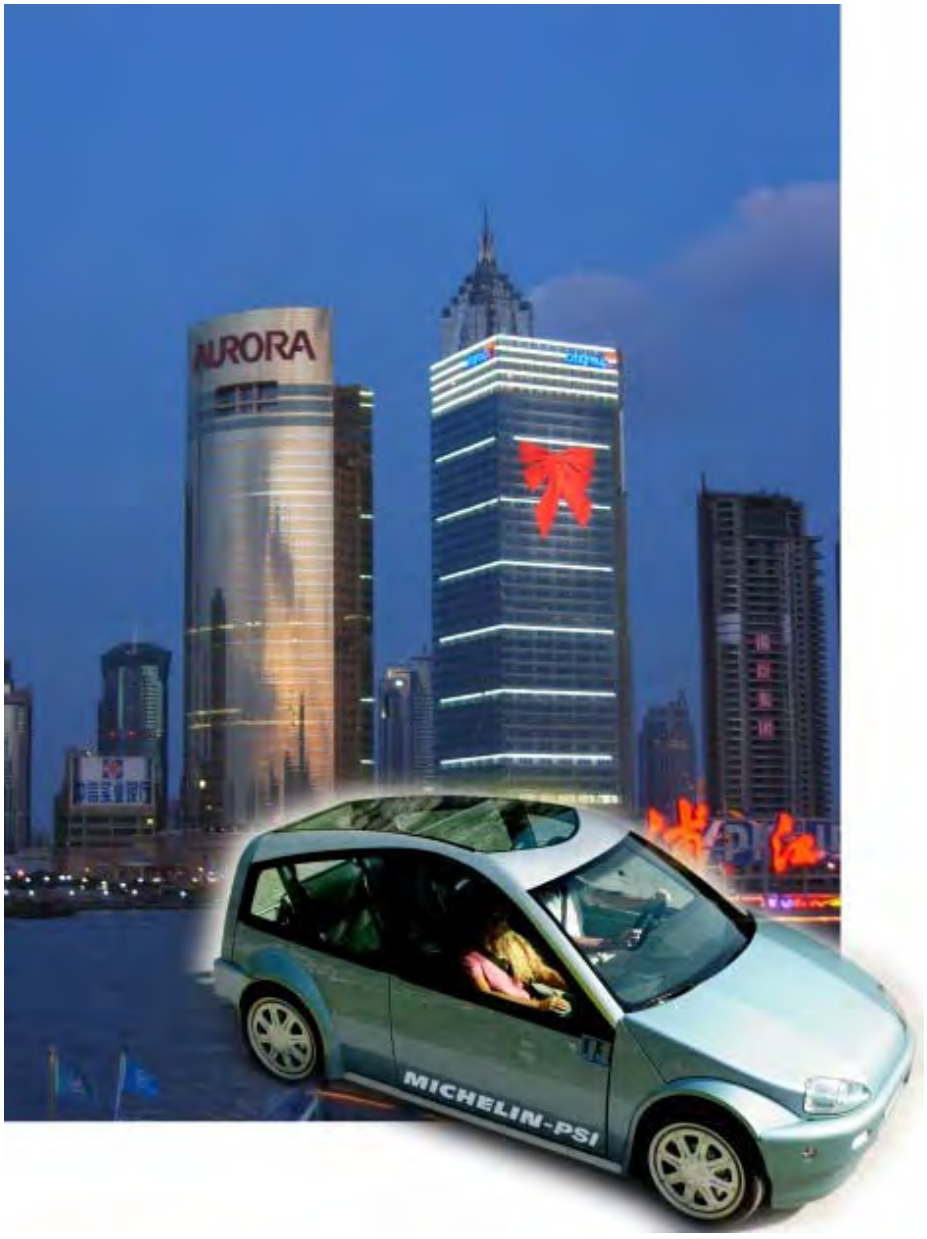

The HY-LIGHT Passenger Car in Front of the Shanghai Skyline

HY-LIGHT, a lightweight passenger car with a H_2/O_2 fuel cell – supercapacitor hybrid power train, was presented to the public in the Chinese city of Shanghai on the occasion of the 6th Challenge Bibendum in October 2004. It represents the successful collaboration of our Laboratory with our industrial partner Construction Développment Michelin (CDM), Switzerland.

THE ELECTROCHEMISTRY LABORATORY

STRUCTURE

Electrochemistry Laboratory

G.G. Scherer (head)
R. Kötz (deputy head)
I. Kalt (secretary)

Fuel Cells

G.G. Scherer

Clean Energy Conversion with high efficiency
Optimized components and cells

Fuel Cell Systems

F. Büchi

Optimisation of system efficiency
Novel stack concepts

Batteries

P. Novak

High energy density
Compact 4V cells

Capacitors

R. Kötz

High power density complementary storage device
High capacitance and cycle life

Materials

Th. Lippert

Design of functional materials
Fundamental understanding of interfacial processes

Interface Analysis

R. Kötz

In situ and *ex situ* characterization of the electrochemical interface

ECL-PERSONNEL

Staff

Alkan Gürsel Selmiye, Dr. ◆ **A**rcaro Manuel ◆ **B**üchi Felix, Dr. ◆ **B**uqa Hilmi, Dr. ◆ **D**eiss Erich, Dr. ◆ **F**oelske Annette, Dr. (since June) ◆ **G**eiger Friederike ◆ **G**loor Thomas (since April) ◆ **G**ubler Lorenz, Dr. ◆ **H**ahn Matthias, Dr. ◆ **H**olzapfer Michael, Dr. ◆ **K**aiser Hermann ◆ **K**alt Isabella, ◆ **K**ötz Rüdiger, Dr. ◆ **L**ippert Thomas, Dr. ◆ **M**army Christian ◆ **N**ovak Petr, Dr. ◆ **P**aganelli Gino ◆ **P**eter Sandra (until March) ◆ **R**aimondi Fabio (until July) ◆ **S**auter Jean-Claude ◆ **S**cheifele Werner ◆ **S**cherer Günther G., Dr. ◆ **S**chneider Ingo, Dr. ◆ **S**chnyder Bernhard, Dr. (until February) ◆ **S**teiger Beat, Dr. ◆ **S**tössel-Sittig Caroline, Dr. (until April) ◆ **T**obler Martina (until July) ◆ **T**sukada Akinori ◆ **U**fheil Joachim, Dr. ◆ **V**etter Jens, Dr. ◆ **W**ambach Jörg, Dr. ◆

PhD Students

Beck-Lempola Nina ◆ **C**ampana Flavio ◆ **C**anulescu Stela (since March) ◆ **D**umont Thomas ◆ **E**rnst Frank ◆ **F**reunberger Stefan ◆ **H**ajbolouri Fia (until May) ◆ **H**auer Marc (until April) ◆ **H**ardwick Laurence ◆ **K**opitkovas Giedrius ◆ **K**ramer Denis ◆ **K**uhn Holger ◆ **K**uhnke Markus ◆ **M**ontenegro Macarena ◆ **P**iotto Piotto Andrea (until May) ◆ **R**einer Andreas ◆ **R**eum Mathias (since October) ◆ **S**antis Marco ◆ **S**laski Michal ◆ **U**rech Lukas ◆ **W**immer Jean ◆ **W**ürsig Andreas ◆

AWARDS

Macarena Montenegro

Can thin perovskite film materials be applied as model systems for battery applications
Young Scientiest Award for the best paper presented in Symposium N. E-MRS Spring meeting, Strasbourg, France, May 2004.

M. Bosco, T.-B. Truong, E. De Boni, F. Vogel, F. Hajbolouri, G.G. Scherer

"Shift-less" fuel processing unit to produce hydrogen from gasoline for fuel cell systems
2nd prize Poster Award at the 15th World Hydrogen Energy Conference, Session 5-4. Hydrogen from Fossil Fuels, Yokohama, Japan, June 27 - July 2, 2004.

THESE PHD STUDENTS FROM ECL GRADUATED IN 2004

Dr. Fia Haibolouri

Polymer electrolyte fuel cells:
Contributions to the understanding of CO-tolerance
Ph.D. Thesis, Nr. 15525, ETH Zürich, April 2004.

Advisor at university:	Prof. A. Wokaun
Advisors at PSI:	Prof. A. Wokaun
	Dr. G.G. Scherer

Dr. Marc Hauer

Laser ablation of polymers studied by time resolved methods
PhD Thesis No. 15422, ETH Zürich, January 2004.

Advisor at university:	Prof. A. Wokaun
Advisors at PSI:	Prof. A. Wokaun
	PD Dr. T. Lippert

Dr. Andrea Piotto Piotto

New electroactive material for lithium-Ion rechargeable batteries
Ph.D. Thesis No. 15659, ETH Zürich, July 2004.

Advisor at university:	Prof. R. Nesper
Advisor at PSI:	PD Dr. P. Novak

EXCHANGE STUDENTS, DIPLOMA THESES, SUMMER STUDENTS

M. Papra
Untersuchungen zum Tieftemperaturverhalten von PE-Brennstoffzellen
Fachhochschule Wismar, October 2003 – February 2004 and July – September 2004.

D. Meyer
Dimensionierung und Bau einer segmentierten Flussfeldplatte für Brennstoffzellen
ETH Zürich and PSI Villigen, October 2003 - March 2004.

T. Meier
Ortsaufgelöste Impedanzspektroskopie an einer segmentierten Brennstoffzelle
Fachhochschule beider Basel Nordwestschweiz, Muttenz, October 2003 - January 2004.

N. Prost
Charakterisierung von strahlengepfropften Membranen auf Basis von Poly(Ethylen-alt-Tetrafluorethylen) für die Polymerelektrolyt-Brennstoffzelle
Fachhochschule beider Basel Nordwestschweiz, Muttenz, October 2003 - January 2004.

V. Bammerlin
Untersuchung von Elektrolytvariationen in Direkt-Methanol-Brennstoffzellen
ETH Zürich, November 2003 - March 2004.

A. Bessat
Synthesis and characterization of radiation-grafted membranes: Investigation of the effect of reactor type on grafted film and membrane properties
Université de Genève and PSI Villigen, November 2003 - April, 2004.

S. Deubelbeiss
Einfluss der Kompression der Diffusionsmedien in der Direkt-Methanol-Brennstoffzelle
ETH Zürich, December 2003 – March 2005.

R. Wälchli
Characterising the water balance of proton conducting membranes in polymer electrolyte fuel cells
ETH Zürich, January – February 2004.

G. Cassina
Experimentelle Untersuchungen an Direkt-Methanol-Brennstoffzellen und Leitfähigkeitsmessungen an protonenleitenden Membranen
ETH Zürich, March – May 2004.

H. Zellweger
Experimentelle Untersuchungen und Methodenentwicklung im Bereich der ortsaufgelösten Impedanzspektroskopie an PEFCs
ETH Zürich, April – June 2004.

T. Finsterwald
Untersuchungen zur Protonenleitfähigkeit verschiedener Brennstoffzellen-Membranen
ETH Zürich, April – July 2004.

R. Randegger
In situ Untersuchungen zum Wasserstransport in verschiedenen Brennstoffzellen-Membranen und *Aufbau eines automatischen Wägesystems*
ETH Zürich, July – October 2004.

A. Epiney
Methodenentwicklung im Bereich der Impedanzspektroskopie an PEFCs in der Zeitdomäne (PSI-Strompulsgeber) und der ortsaufgelösten Impedanzspektroskopie an PEFCs
EPF Lausanne, July – October 2004.

SEMINAR, INVITED SPEAKERS

P.H. Rodatz
ETH Zürich
Dynamik einer Polymerelektolyt-Brennstoffzelle: Experimente und Modell-basierte Analysen
January 19, 2004.

Dr. R. Imhof
Renata AG, Itingen
Als Elektrochemiker in der Industrie – Einblick in den Arbeitsalltag
January 26, 2004.

Prof. R. Nesper
ETH Zürich
From refractory to nano materials-synthesis and properties of selected solids
February 02, 2004.

M. Lanz
Mettler Toledo, Greifensee
Coulombmetrische Karl-Fischer-Titration
April 05, 2004.

Y. Müller
EMPA Dübendorf
Mikroelektrochemie
April 19, 2004.

C.-H. Dustmann
MES-DEA, Stabio
ZEBRA, eine sehr elegante Batteriechemie mit vielen offenen Fragen
April 26, 2004.

V. Graf
DaimlerChrysler, Stuttgart, Germany
Impedanzspektroskopie an PEFC
May 05, 2004.

B. Bürgler
ETH Zürich
Single chamber solid oxide fuel cells
July 05, 2004.

M. Höckel, P. Walther
Fachhochschule Biel
Brennstoffzellenprojekte an der HTI Biel
August 16, 2004.

Dr. I. Potapova
Universität Bern
Untersuchungen zur Gasentwicklung an Lithium-Ionen-Batterien
September 27, 2004.

Dr. M. Döbeli
ETH Zürich and PSI
MeV Ionenstrahlanalyse
October 04, 2004.

CONFERENCES - WORKSHOPS

Advanced Characterization Methods for Electrochemical Cells
19th One-Day-Symposium
January 16, 2004
Organizers: G.G. Scherer and R. Kötz

With contributions from:

Prof. Dr. K. Edström, Uppsala University, Sweden
Dr. O. Haas, PSI, Villigen
Prof. Dr. D. Fermín, Universität Bern
Prof. Dr. J. Behm, Universität Ulm, Germany
Dr. N. Wagner, Deutsches Zentrum für Luft- und Raumfahrt, Stuttgart, Germany
Prof. Dr. D. Landolt, EPF, Lausanne

Novel Trends in Electrochemistry
20th One-Day-Symposium
September 15, 2004
Organizer: G.G. Scherer

With contributions from:

Prof. Dr. F. Endres, Technische Universität Clausthal, Germany
Prof. Dr. M. Grätzel, EPF Lausanne
Prof. Dr. U. Stimming, Technische Universität München, Germany
Prof. Dr. N. Alonso-Vante, Université de Poitiers, France
Dr. R. Schuster, Fritz-Haber-Institut der MPG, Berlin, Germany
Dr. M. Rohnke, Universität Giessen, Germany

2nd Infrared Workshop, National Science Foundation
Bern, December 7, 2004
Organizer and Chairman: J. Wambach

REVIEW ACTIVITIES OF THE LABORATORY FOR THE FOLLOWING JOURNALS

Applied Physics A ◆ **A**pplied Physics Letters ◆ **A**pplied Surface Science ◆ **A**nalytical Chemistry ◆ **A**ngewandte Chemie ◆ **C**atalysis Communications ◆ **E**lectrochimica Acta ◆ **E**lectrochemistry Communications ◆ **E**lectrochemical Solid State Letters ◆ **E**urophysics Letters ◆ **F**uel Cells ◆ **I**EEE Transactions on Plasma Science ◆ **J**ournal of Applied Electrochemistry ◆ **J**ournal of Applied Physics ◆ **J**ournal of Electroanalytical Chemistry ◆ **J**ournal of the Electrochemical Society ◆ **J**ournal of Fuel Cell Science and Technology ◆ **J**ournal of Materials Chemistry ◆ **J**ournal of Microlithography ◆ **M**icrofabrication and Microsystems ◆ **J**ournal of Photochemistry Photobiology A: Chemistry ◆ **J**ournal of Physical Chemistry ◆ **J**ournal of Power Sources ◆ **L**ab-on-a-Chip ◆ **O**ptical Materials ◆ **O**ptics Communications ◆ **P**hysical Chemistry Chemical Physics ◆ **Z**eitschrift für Physikalische Chemie ◆

REVIEW ACTIVITIES OF THE LABORATORY FOR THE FOLLOWING ORGANISATIONS

Alexander von Humboldt-Stiftung, Germany ◆ **E**PF Lausanne, Switzerland ◆ **E**uropean Science Foundation (ESF) ◆ **I**WT Flanders, Belgium ◆ **M**istra, Sweden ◆ **P**rognis AG, Switzerland ◆ **P**SI FOKO, Switzerland ◆ **U**niversität Ulm, Germany ◆ **U**S-Israel Binational Science Foundation, Israel ◆

CO-REFEREE'S REPORT FOR DISSERTATIONS

M. **H**auer, PSI/ETH Zürich ◆ F. **H**ajbolouri, ETH Zürich ◆ V.M. **G**raubner, TU Munich, Germany ◆ M. **G**uillong, ETH Zürich ◆ A. **P**iotto Piotto, PSI/ETH Zürich ◆ L. **S**teuernagel, ETH Zürich ◆ G. **S**udant, University of Amiens, France ◆ B. **T**oftman, University of Southern Denmark, Odense, Denmark ◆

INDUSTRIAL PARTNERS

The Laboratory had the pleasure to collaborate with the following industrial partners during the year 2004:

Agie SA, Losone, Switzerland ◆ ***A***VL List GmbH, Graz, Austria ◆ **B**ASF AG, Ludwigshafen, Germany ◆ Robert **B**osch GmbH, Stuttgart, Germany ◆ **C**onstruction Développment Michelin SA (CDM), Givisiez, Switzerland ◆ **D**egussa, Creavis Technology & Innovation, Marl, Germany ◆ **D**uPont Corp., Le Grand Saconnex, Switzerland ◆ **D**yconex AG, Bassersdorf, Switzerland ◆ **F**erro GmbH, Frankfurt/Main, Germany ◆ **G**APC-Opel AG, Rüsselsheim, Germany ◆ W.L. **G**ore & Associates, Inc., Elkton, USA ◆ **M**axwell Technologies SA, Rossens, Switzerland ◆ **N**issan Motors Co., Ltd. Yokosuka, Japan ◆ **P**EMEAS GmbH, Frankfurt, Germany ◆ **R**iwisa AG, Hägglingen, Switzerland ◆ **T**IMCAL AG, Bodio, Switzerland ◆

PROJECTS, TEACHING ACTIVITIES, SCIENTIFIC CONTRIBUTIONS TO JOURNALS AND CONFERENCES, PATENT APPLICATIONS AND MEMBERSHIPS

PROJECT COLLABORATIONS WITH EXTERNAL PARTNERS

BBW

Projektleiter: F.N. Büchi
HYTRAN (Hydrogen and Fuel Cell Technologies for Road Transport)
EU-Projekt

Projektleiter: P. Novák
ALiSTORE (Advanced lithium energy storage systems based on the use of nano-powders and nano-composite electrodes/electrolytes)
EU-Projekt (Network of Excellence)

Projektleiter: P. Novák
CAMELiA (Calendar life mastering of Li-ion accumulator)
EU-Projekt

Projektleiter: P. Novák
LiBERAL (Lithium battery evaluation and research – accelerated life test direction)
EU-Projekt

Projektleiter: P. Novák
SLiON (Solvent-free lithium polymer starter battery)
EU-Projekt

BFE

Projektleiter: F.N. Büchi
Numerische Modellierung von PE Brennstoffzellen mit der FE-Methode
mit ZHW, Winterthur

Projektleiter: F.N. Büchi
Untersuchung des Temperaturverhaltens von PE Brennstoffzellen im Bereich 0 bis -10 °C

Projektleiter: R. Kötz
Integrated micro-supercapacitor

Projektleiter: G.G. Scherer
Polymer Elektrolyt Brennstoffzellen mit H_2 und Methanol als Brennstoff

EOARD

Projektleiter: T. Lippert
Polymers used as fuel in laser plasma thrusters for small satellites

EU AND INDUSTRY (CRAFT)

Projektleiter: P. Novák
High performance active smart card with contactless charging
EU-Projekt

INDUSTRY

Projektleiter: P. Dietrich
HY-LIGHT: Development of hybrid fuel cell – supercapacitor power train for passenger car
Construction Développment Michelin SA (CDM), Givisiez

Projektleiter: L. Gubler
Membranen für die Direkt Methanol Brennstoffzelle
Chemische Industrie

Projektleiter: L. Gubler
CO-Toleranz von Polymerelektrolyt-Brennstoffzellen
Robert Bosch GmbH, Tamm bei Stuttgart, Germany

Projektleiter: L. Gubler
Membranen für Brennstoffzellen
Chemische Industrie

Projektleiter: P. Novák
Elektrochemische Charakterisierung von Oxiden für Lithiumionen-Batterien
Ferro GmbH, Frankfurt (Main), Germany

Projektleiter: P. Novák
Entwicklung eines Batterieseparators auf Basis der keramischen Membranfolie der CREAVIS
CREAVIS Gesellschaft für Technologie und Innovation mbH, Marl, Germany

Projektleiter: P. Novák
Behandlung der Graphite für die negative Elektrode der Lithiumionen-Batterie
TIMCAL AG, Bodio

Projektleiter: P. Novák
Characterization of electrochemical processes
Nissan Motor Co. Ltd., Yokohama, Japan

Projektleiter: P. Novák
Characterization of graphite electrodes (Project No. 1)
Nissan Motor Co. Ltd., Yokohama, Japan

Projektleiter: P. Novák
Characterization of graphite electrodes (Project No. 2)
Nissan Motor Co. Ltd., Yokohama, Japan

Projektleiter: G.G. Scherer
Diagnostics of polymer electrolyte fuel cells
Nissan Motor Co. Ltd., Yokohama, Japan

Projektleiter: G.G. Scherer
Membranenentwicklung für Brennstoffzellen
Chemische Industrie

KTI

Projektleiter: R. Kötz
Optimized electrochemical capacitors

Projektleiter: R. Kötz
Synthesis of supported nanostructured high porosity carbon as electrode material

Projektleiter: B. Schnyder
Corrosion aspects of the EDM process

NATIONALFONDS

Projektleiter: R. Kötz
Scanning probe microscopy of the solid electrolyte interface

Projektleiter: P. Novák
Synthesis and characterization of advanced electroactive materials for electrodes of rechargeable lithium-ion batteries (Project No. 1)

Projektleiter: P. Novák
Synthesis and characterization of advanced electroactive materials for electrodes of rechargeable lithium-ion batteries (Project No. 2)

Projektleiter: A. Wokaun, T. Lippert
Comparison of the mechanisms of laser ablation and laser-induced material transfer

TEACHING ACTIVITIES

University Level Teaching

PD. Dr. T. Lippert
Mikro- und Nanostrukturen: Laseranwendungen in Industrie und Forschung
ETH Zürich, WS 2004/05.

PD Dr. P. Novák, Prof. Dr. A. Wokaun
Technische Elektrochemie
ETH Zürich, WS 2004/2005.

PD Dr. P. Novák
Technische Elektrochemie
Praktikum, ETH Zürich, SS 2004.

Prof. Dr. A. Wokaun, Dr. J. Gass, Dr. G.G. Scherer
Technik erneuerbarer Energien, Teil 2
ETH Zürich, WS 2004/2005.

Contributions to Courses at Universities, Universities of Applied Sciences, and Other Institutes

A. Reiner, Prof. E. Jochem[1]
What are the costs for a fuel cell? Today and tomorrow.
Beitrag zum energiewirtschaftlichen Doktorierenden-Seminar, ETH Zürich, March 4, 2004.
[1] ETH Zürich

Dr. G.G. Scherer
Four lectures on electrochemical energy conversion and storage
Workshop on Energy Conversion and Storage, International Center for Condensed Matter Physics, University of Brasilia, Brazil, November 22-26, 2004.

PUBLICATIONS

Books and Reviewed Book Chapters

T. Lippert, editor
Polymers and light
(ISBN: 3-540-40471-6), Springer Series Advances in Polymer Science **168** (2004).

T. Lippert
Laser applications of polymers
Polymers and Light
(ISBN: 3-540-40471-6), Advances Polymer Science **168**, 51-246 (2004).

T. Lippert, I.W. Boyd, D.B. Chrisey, E. Millon
Photonic processing of surfaces, thin films & devices
(ISSN: 0040-6090), E-MRS Symposia Proceedings, Elsevier, Amsterdam **150** (2004).

M.J. Montenegro, T. Lippert, A. Weidenkaff[1], A. Wokaun
Thin epitaxial oxide films as model systems for electrocatalysts
Nanophotonics: Integrating Photochemistry, Optics, and Nano/Bio-Materials Studies
Eds. H. Masuhara, S. Kawata, Elsevier Science, ISBN: 0444517650, Amsterdam 251-273 (2004).
[1] University of Augsburg, Germany

Peer Reviewed Papers

B. Andreaus, G.G. Scherer
Proton-conducting polymer membranes in fuel cells-humidification aspects
Solid State Ionics **168**, 311-320 (2004).

H.P. Brack, D. Ruegg[1], H. Bührer[1], M. Slaski, S. Alkan, G.G. Scherer
Differential scanning calorimetry and thermo-gravimetric analysis investigation of the thermal properties and degradation of some radiation-grafted films and membranes
J. Polym. Sci. Part. B: Polym. Phys. **42**, 2612-2624 (2004).
[1] Zürich University of Applied Sciences, Winterthur

H.P. Brack, C. Padeste, M. Slaski, S. Alkan, H.H. Solak
Preparation of micro- and nano-patterns of polymer chains grafted onto flexible polymer substrates
J. Am. Chem. Soc. **126**, 1004-1005 (2004).

H.P. Brack, M. Slaski, L. Gubler, G.G. Scherer, S. Alkan, A. Wokaun
Characterization of fuel cell membranes as a function of drying by means of contact angle measurements
Fuel Cells **4**, 141-146 (2004).

A. Braun, J. Kohlbrecher, M. Bärtsch, B. Schnyder, R. Kötz, O. Haas, A. Wokaun
Small-angle neutron scattering and cyclic voltammetry study on electrochemically oxidized and reduced pyrolytic carbon
Electrochim. Acta **49,** 1105–1112 (2004).

F.N. Büchi, J.F. Affolter[1], S. Camenzind[2], N. Chmielewski[3], P. Dietrich, M. Höckel[4], M. Ruge[4], M. Santis
PEFC: Stacks, systems, and applications
Chimia **58**, 869-878 (2004).
[1] EIVD Yverdon
[2] Esoro AG, Fällanden
[3] MES-DEA SA, Stabio
[4] FH Bern, Biel

R. Dominko[1], M. Gaberscek[1], M. Bele[1], J. Drofenik[1], E.M. Skou[2], A. Würsig, P. Novák, J. Jamnik[1]
Understanding the role of gelatin as a pretreating agent for use in Li-ion batteries
J. Electrochem. Soc. **151**, A1058-A1062 (2004).
[1] National Institute of Chemistry, Ljubljana, Slovenia
[2] University of Southern Denmark, Odense, Denmark

T. Dumont, T. Lippert, A. Wokaun, P. Leyvraz[1]
Laser writing of 2D data matrices in glass
Thin Solid Films **453**, 42-45 (2004).
[1] Frewitt Printing SA, Corminboeuf

Th. Dumont, S. Lazare[1], T. Lippert, A. Wokaun
Changes in the etch rate of photosensitive polymers as a function of the pulse number
Appl. Phys A **79**, 1271-1274 (2004).
[1] University of Bordeaux, France

A.B. Geiger, R. Eckl[1], A. Wokaun, G.G. Scherer
An approach to measuring locally resolved currents in polymer electrolyte fuel cells
J. Electrochem. Soc. **151**, A394-A398 (2004).
[1] TU Munich, Germany

D. Goers, M. Holzapfel, W. Scheifele, E. Lehmann, P. Vontobel, P. Novák
In situ neutron radiography of lithium-ion batteries: The gas evolution on graphite electrodes during the charging
J. Power Sources **130**, 221-226 (2004).

V.-M. Graubner[1], R. Jordan[1], O. Nuyken[1], B. Schnyder[1], T. Lippert, R. Kötz, A. Wokaun
Photochemical modification of crosslinked poly(dimethylsiloxane) by irradiation at 172 nm
Macromolecules **37**, 5936-5943 (2004).
[1] TU Munich, Germany

L. Gubler, H. Kuhn, T.J. Schmidt, G.G. Scherer, H.P. Brack, K. Simbeck
Performance and durability of membrane electrode assemblies based on radiation-grafted fep-g-polystyrene membranes
Fuel Cells **4**, 196-207 (2004).

L. Gubler, S. Alkan Gürsel, F. Hajbolouri, D. Kramer, N. Beck-Lempola, A. Reiner, B. Steiger, G.G. Scherer, A. Wokaun, B. Rajesh[1], K.R. Thampi[1]
Materials for polymer electrolyte fuel cells PEFC
Chimia **58**, 826-836 (2004).
[1] EPF Lausanne

M. Hahn, M. Baertschi, O. Barbieri, J.-C. Sauter, R. Kötz, R. Gallay[1]
Interfacial capacitance and electronic conductance of activated carbon double-layer electrodes
Electrochemical and Solid-State Letters **7**, A33-A36 (2004).
[1] Maxwell Technologies SA, Rossens

F. Hajbolouri, B. Andreaus, G.G. Scherer, A. Wokaun
CO Tolerance of commercial Pt and PtRu gas diffusion electrodes in polymer electrolyte fuel cells
Fuel Cells **4**, 160-168 (2004).

M. Hauer, D.J. Funk[1], T. Lippert, A. Wokaun
Time resolved study of the laser ablation induced shockwave
Thin Solid Films **453**, 584-588 (2004).
[1] Los Alamos National Laboratory, USA

M. Hauer, T. Lippert, A. Wokaun
Ns-surface interferometry measurements on designed and commercial polymers
Appl. Phys. A **79**, 1215-1218 (2004).

M. Holzapfel, C. Jost[1], P. Novák
Stable cycling of graphite in an ionic liquid based electrolyte
Chem. Commun., 2098-2099 (2004).
[1] Degussa AG, Marl, Germany

G. Kopitkovas, T. Lippert, C. David, A. Wokaun, J. Gobrecht
Surface micromachining UV-transparent materials
Thin Solid Films **453**, 31-35 (2004).

G. Kopitkovas, T. Lippert, C. David, S. Canulescu, A. Wokaun, J. Gobrecht
Fabrication of beam homogenizers in quartz by laser micromachining
J. Photochem. Photobiol. A: Chem. **166**,135-140 (2004).

G. Kopitkovas, T. Lippert, C. David, R. Sulcas[1], J. Hobley[2], A. Wokaun, J. Gobrecht
Laser micromachining of optical devices
SPIE Proc. **5662**, 515-525 (2004).
[1] EKSPLA Ltd., Vilnius, Lithuania
[2] Tohoku University, Sendai, Japan

D. Kramer, A.J. McEvoy[1], I. Schneider, H. Kuhn, A. Wokaun, G.G. Scherer
Test and measurements methods for fuel cell technology
Chimia **58**, 851-856 (2004).
[1] EPF Lausanne

M. Kuhnke, Th. Lippert, E. Ortelli[1], C. David, G.G. Scherer, A. Wokaun
Microstructuring of glassy carbon: Comparison of laser machining and reactive ion etching
Thin Solid Films **453**, 36-41 (2004).
[1] Dyconex AG, Bassersdorf

I. Mantzaras, S.A. Freunberger, F.N. Büchi, M. Roos[1], W. Brandstätter[2], M. Prestat[3], L.J. Gauckler[3], B. Andreaus, F. Hajbolouri, S.M. Senn[3], D. Poulikakos[3], A.K. Chaniotis[3], D. Larrain[4], N. Autissier[4], F. Maréchal[4]
Fuel cell modeling and simulations
Chimia **58**, 857-868 (2004).
[1] ZHW Winterthur
[2] Christian-Doppler-Laboratorium, Leoben, Austria
[3] ETH Zürich
[4] EPF Lausanne

K. Meissner, T. Lippert, A. Wokaun, D. Guenther[1]
Analysis of trace metal: Comparison of laser induced breakdown spectroscopy with LA-ICP-MS
Thin Solid Films **453**, 316-322 (2004).
[1] ETH Zürich

M.J. Montenegro, M. Döbeli[1], T. Lippert, S. Mueller[2], A. Weidenkaff[3], P. R. Willmott[4], A. Wokaun
Microstructures and film properties of $La_{0.7}Ca_{0.3}CoO_3$ produced by pulsed reactive crossed-beam laser ablation
Thin Solid Films **453**, 182-186 (2004).
[1] ETH Zürich and PSI
[2] Euresearch Bern
[3] University of Augsburg, Germany
[4] University of Zürich and PSI

C. Padeste, H.H. Solak, H.P. Brack, M. Slaski, S. Alkan Gürsel, G.G. Scherer
Patterned grafting of polymer brushes onto flexible polymer substrates
J. Vac. Sci. Technol. B **22**, 3191-3195 (2004).

C. Padeste, B. Steiger, A. Grubelnik, L. Tiefenauer
Molecular assembly of redox-conductive ferrocene-streptavidin conjugates – towards bio-electrochemical devices
Biosens. Bioelectron. **20**, 545-552 (2004).

S. Park, H. Schift, C. Padeste, B. Schnyder, R. Kötz
Anti-adhesive layers on nickel stamps for nanoimprinting lithography
Microelectronic Engineering **73,** 196-201 (2004).

C.R. Phipps[1], J.R. Luke[2], T. Lippert
Laser ablation of organic coatings as a basis for micropropulsion
Thin Solid Films **453-454**, 573-583 (2004).
[1] Photonic Associates, Santa Fe, USA
[2] NMT Albuquerque, USA

C.R. Phipps[1], J.R. Luke[2], T. Lippert, M. Hauer, A. Wokaun
Micropropulsion using laser ablation
Appl. Phys. A **79**, 1385-1389 (2004).
[1] Photonic Associates, Santa Fe, USA
[2] NMT Albuquerque, USA

C.R. Phipps[1], J.R. Luke[2], T. Lippert, M. Hauer, A. Wokaun
Micropropulsion using a laser ablation jet
J. Prop. Power **20**, 1000-1011 (2004).
[1] Photonic Associates, Santa Fe, USA
[2] NMT Albuquerque, USA

C.R. Phipps[1], J.R. Luke[2], D.J. Funk[3], D.S. Moore[3], J. Glownia[3], T. Lippert
Measurements of laser impulse coupling at 130 fs
Proc. SPIE, **5448**, 1201-1209 (2004).
[1] Photonic Associates, Santa Fe, USA
[2] NMT Albuquerque, USA
[3] Los Alamos National Laboratory, USA

T. Rager
Parameter study for the pre-irradiation grafting of styrene/divinylbenzene onto poly(tetrafluoroethylene-co-hexafluoropropylen) from isopropanol solution
Helv. Chim. Acta **87**, 400-407 (2004).

P. Rodatz[1], F.N. Büchi , C. Onder[1], L. Guzzella[1]
Operational aspects of a large PEFC stack under practical conditions
J. Power Sources **128**, 208-217 (2004).
[1] ETH Zürich

M. Santis, D. Schmid[1], M. Ruge[1], S. Freunberger, F.N. Büchi
Modular stack-internal air humidification concept-verification in a 1kW stack
Fuel Cells **4**, 214-218 (2004).
[1] ETH Zürich

B. Schnyder, C. Stössel-Sittig, R. Kötz, S. Hochstrasser-Kurz[1], S. Virtanen[1], Ch. Jaeggi[2], N. Eichenberger[2], H. Siegenthaler[2]
Investigation of the electrochemical behaviour of tungsten carbide with electrochemical and surface analytical methods
Surf. Sci. **566-568**, 1240-1245 (2004).
[1] ETH Zürich
[2] University of Bern

C.K. Shin[1], B. Andreaus, G. Maier[1], G.G. Scherer
Block copolymer ionomers for ion conductive membranes
J. Membr. Sci. **245**, 147-161 (2004).
[1] TU Munich, Germany

C.K. Shin[1], G. Maier[1], G.G. Scherer
Acid functionalized poly(arylene ether)s for proton-conducting membranes
J. Membr. Sci. **245**, 163-173 (2004).
[1] TU Munich, Germany

M.E. Spahr[1], T. Palladino[1], H. Wilhelm[1], A. Würsig, D. Goers, H. Buqa, M. Holzapfel, P. Novák
Exfoliation of graphite during electrochemical lithium insertion in ethylene carbonate-containing electrolytes
J. Electrochem. Soc. **151**, A1383-A1395 (2004).
[1] TIMCAL SA, Bodio

C. Stössel-Sittig, B. Schnyder, R. Kötz
XPS and AES surface characterisation of WC-Co after electro-discharge machining
Surface and Interface Analysis **36,** 777-779 (2004).

T. Vad[1], F. Hajbolouri, H.-G. Haubold[1], G.G. Scherer, A. Wokaun
Anomalous small-angle X-ray scattering study on the nanostructure of Co-sputtered platinum/carbon layers
J. Phys. Chem B **108**, 12442-12449 (2004).
[1] FZ Jülich, Germany

J. Van herle[1], A. Schuler[2], L. Dammann[3], M. Bosco, T.B. Truong, E. De Boni, F. Hajbolouri, F. Vogel, G.G. Scherer
Fuels for fuel cells: Requirements and fuel processing
Chimia **58**, 887-895 (2004).
[1] EPF Lausanne
[2] Sulzer HEXIS, Winterthur
[3] ZHW, Winterthur

A. Weidenkaff[1], C. Diecker[1], T. Lippert, M.J. Montenegro
Nucleation and growth of epitaxial $La_{1-x}Ca_xCoO_{3-\delta}$ films on single crystalline substrates by pulsed reactive crossed beam laser ablation
Thin Solid Films **453-454**, 406-410 (2004).
[1] University of Augsburg, Germany

D. Wolffframm[1], M. Ratzke[1], M. Kappa[2], M.J. Montenegro, M. Döbeli[3], T. Lippert, J. Reif
Pulsed laser deposition of thin Pr_xO_y films on Si(100)
Materials Science & Engineering B **109**, 24 (2004).
[1] IHP, BTU JointLab, Cottbus, Germany
[2] BTU Cottbus, Germany
[3] ETH Zürich and PSI

Other Papers

N.K. Beck, B. Steiger, G.G. Scherer, A. Wokaun
Methanol tolerant oxygen reduction catalysts derived from electrochemically pre-treated $Bi_2Pt_{2-y}Ir_yO_7$ pyrochlores
Proc. 2nd France-Deutschland Fuel Cell Conference, Belfort, France, November 29 – December 2 (2004).

L. Gubler, N. Prost, S. Alkan Gürsel, D. Kramer, G.G. Scherer
Radiation grafted proton exchange membranes based on ETFE-g-polystyrene for low temperature fuel cells
Proc. 2nd France – Deutschland Fuel Cell Conference, Belfort, France, November 29 – December 2 (2004).

M. Hahn, M. Baertschi, O. Barbieri, J-C. Sauter, R. Kötz
Kapazität und elektronische Leitfähigkeit von Aktivkohle-Doppelschicht-Elektroden.
Elektrochemie und Materialforschung, K. Jüttner und J. Russow (Edt.), Gesellschaft Deutscher Chemiker, GDCH Monographie **29**, 2003, 120-129 (2004).

M. Hahn, O. Barbieri, M. Campana, R. Gallay[1] R. Kötz
Charge-induced dimensional changes in electrochemical double layer capacitors
Proc.14th International Seminar on Double Layer Capacitors and Hybrid Energy Storage Devices, Deerfield Beach, USA, December 6–8 (2004).
[1] Maxwell Technologies SA, Rossens

F. Hajbolouri, S. Abholhassani-Dadras, B. Schnyder, M. Horisberger, T. Vad[1], G.G. Scherer, A. Wokaun
Characterization of Co-sputtered Pt/C films
Proc. 2nd France-Deutschland Fuel Cell Conference, Belfort, France, November 29 – December 2 (2004).
[1] FZ Jülich, Germany

F. Hajbolouri, B. Andreaus, G.G. Scherer, A. Wokaun
CO-poisoning in polymer electrolyte fuel cells studied by AC-impedance spectroscopy
Proc. 2nd France-Deutschland Fuel Cell Conference, Belfort, France, November 29 – December 2 (2004).

E. Harzfeld[1], R Gallay[1], M. Hahn, R. Kötz
Capacitance and series resistance determination in high power ultracapacitors
Proc. 1st European Symposium on Super Capacitors & Applications, Belfort, France, November 5 (2004).
[1] Maxwell Technologies, Rossens

H. Kuhn, B. Andreaus, A. Wokaun, G.G. Scherer
Advances in the investigation of polymer electrolyte fuel cells by electrochemical impedance spectroscopy
Proc. 2nd France-Deutschland Fuel Cell Conference, Belfort, France, November 29 – December 2 (2004).

T. Lippert
Preface from the Editor
Thin Solid Films **453-454**, 1-2 (2004).

A. Reiner, B. Steiger, A. Wokaun, G.G. Scherer
Influence of the morphology on the platinum electrode surface activity
Proc. 2nd France-Deutschland Fuel Conference, Belfort, France, November 29 – December 2 (2004).

G.G. Scherer
Fuel cells in Switzerland – a brief retrospective view
Chimia **58**, 824-825 (2004).

L. Urech, M. Hauer, T. Lippert, C.R. Phipps[1], E. Schmid, A. Wokaun, I. Wysong[2]
Designed polymers for laser-based microthrusters – correlation of thrust with material, plasma, and shockwave properties
Proc. SPIE **5448**, 52-64 (2004).
[1] Photonic Associates, Santa Fe, USA
[2] EOARD London, UK

F. Vogel, G.G. Scherer
Nachhaltige Verfahren der Wasserstofferzeugung und –nutzung
SATW-Bulletin 4/03, 21-27 (2004).

A. Würsig, H. Buqa, M.E. Spahr[1], P. Novák
Exfoliation of graphite negative electrode material in lithium-ion batteries: The in situ approach
GDCh-Monographie **29**, 110-119 (2004).
[1] TIMCAL SA, Bodio

TALKS

Invited Talks

F.N. Büchi
Brennstoffzellen: Technologie, Anwendungen, Perspektiven
Energieagentur der Wirtschaft, Kreuzlingen, March 9, 2004.

F.N. Büchi
Potenzial von Brennstoffzellen in mobilen Anwendungen
Impulstag Brennstoffzellen, Biel, November 12, 2004.

H. Buqa
SEI film formation on highly crystalline graphitic materials
IBA 2004, Graz, Austria, April 20, 2004.

S.A. Freunberger
Model approaches for the description of lateral effects in PE fuel cells
Seminar on Fuel Cell Modeling, Zürich, March 20-21, 2004.

R. Kötz
Supercapacitor electrodes based on carbonaceous materials
International Battery Materials Association - Battery and Fuel Cell Materials Symposium, Graz, Austria, April 18-22, 2004.

R. Kötz
Battery or ultracapacitor?
4th BOOSTCAP Meeting, Fribourg, April 29, 2004.

R. Kötz
Temperature behavior and impedance fundamentals of supercapacitors
19th Ulm Electrochemical Talks, UECT, Ulm, Germany, May 17-18, 2004.

R. Kötz
Grundlagen und Wirkungsweise von Doppelschicht-kondensatoren
Supercaps - Energiespeicher mit hoher Leistungsdichte, Haus der Technik, Essen, Germany, June 23–24, 2004.

R. Kötz
The solide side of the double-layer: Capacitance limits of carbon based supercapacitors.
Keynote Lecture, Annual ISE Meeting 2004, Thessaloniki, Greece, September 19-24, 2004.

T. Lippert
The poor man's star war: Laser ablation und ihre Anwendungen
Technical University Munich, Germany, January 2004.

T. Lippert
Chemical and Spectroscopic Aspects of Laser Ablation: Spectroscopic Features and Novel Directions
APS (American Physical Society) Spring Meeting, Montreal, Canada, March 2004.

T. Lippert
Laser interaction with materials: From thin film deposition to laser plasma thrusters
- Los Alamos National Laboratory, Los Alamos, USA, April 2004.
- IBM Research Laboratories, Rüschlikon, June 2004.

T. Lippert
Designed polymers for laser-based microthrusters: correlation of thrust with material, plasma and shockwave properties
Plenary session talk at the SPIE Symposium on High Power Laser Ablation (HPLA 2004), Taos, USA, April 2004.

T. Lippert
Laser micromachining of optical devices
- 5th International Symposium on Laser Precision Microfrabrication (LPM2004), Nara, Japan, May 2004.
- SOPRA Laser, Paris, France, July 2004.

T. Lippert
Pulsed laser deposition of thin oxide films: Model systems for electrochemical studies
Nonmetallic Inorganic Materials, ETH Zürich, June 2004.

T. Lippert
Direct laser structuring of polymers
Workshop on Bridging Direct Write Technology Dimensions, Seward, Alaska, USA, June 2004.

P. Novák
Batterien
PEMEAS GmbH, Frankfurt (Main), Germany, December 14, 2004.

P. Novák
Die Lithiumionen-Batterie
Batterieseminar der Hochschule für Technik und Informatik Biel, September 1, 2004.

P. Novák
Gas evolution from lithium-ion battery electrodes
Nissan Research Center, Nissan Motor Co., Ltd., Yokosuka, Japan, July 5, 2004.

P. Novák
Advanced in situ characterization methods applied to carbonaceous electroactive materials
12th Int. Meeting on Lithium Batteries, Nara, Japan, June 28, 2004.

P. Novák
Electrochemistry of materials for lithium-ion batteries
Seminar of the Particle Technology Laboratory, ETH Zürich, April 6, 2004.

P. Novák
Raman spectroscopic mapping of electrodes for lithium-ion batteries
55th Annual ISE Meeting, Thessaloniki, Greece, September 19-24, 2004.

G. Paganelli
La pile à combustibles PEFC appliqué à la motorisation automobile
Voiture et cité de demain, EPF Lausanne, March 31, 2004

G.G. Scherer
Materials aspects of polymer electrolyte fuel cells
SINO-European Bilateral Meeting on Material Aspects for Future Energy Supply, Nice, France, December 6-8, 2004.

G.G. Scherer, D. Kramer, H. Kuhn, I. Schneider, B. Andreaus, A. Wokaun
In situ diagnostic methods for polymer electrolyte fuel cells
Annual ISE Meeting 2004, Thessalonikki, Greece, September 19-24, 2004.

G.G. Scherer
Ageing and degradation of polymer electrolyte fuel cells
Nissan Research Center, Yokohama, Japan, February 19, 2004.

G.G. Scherer
Recent progress in polymer electrolyte fuel cell research at Paul Scherrer Institut
Asahi Glass Corp., Yokohama, Japan, February 18, 2004.

G.G. Scherer
Some materials research & development activities in the area of polymer electrolyte fuel cell at Paul Scherrer Institut
Yokohama National University, Prof. Dr. K. Ohta, Yokohama, Japan, February 18, 2004.

G.G. Scherer
An overview on the research and development activities in the area of polymer electrolyte fuel cells at Paul Scherrer Institut
Yamanashi University, Prof. Dr. W. Watanabe, Kofu, Japan, February 17, 2004.

G.G. Scherer
Electrocatayis for polymer electrolyte fuel cells, R & D at Paul Scherrer Institut
AIST, Prof. Okada, Tsukuba, Japan, February 16, 2004.

J. Wambach
The SLS IR Beamline
Seminar at the Molecular Kinetics And Spectroscopy Group; Prof. M. Quack; Departement Chemie und Angewandte Biowissenschaften, ETH Zürich, February 12, 2004.

J. Wambach
"NanoKat"; Heterogeneous catalysis on an atomic level
Seminar in Experimentalphysik, Physik-Institut der Universität Zürich, December 16, 2004.

Contributions to Media

P. Dietrich et al.
Projekt Integral
10 vor 10 Beitrag über HY-LIGHT
SF-DRS, October 2004.

Other Talks

S. Alkan Gürsel, L. Gubler, G.G. Scherer
Radiation grafted membranes for fuel cells
IRaP 2004, 6th International Symposium on Ionizing Radiation and Polymers, Houffalize, Belgium, September 25-30, 2004.

O. Barbieri
Influence of micropores size on the double layer capacitance of wood-based carbon materials for electrochemical capacitors.
Annual ISE Meeting 2004, Thessaloniki, Greece, September 19-24, 2004.

N.K. Beck, B. Steiger, G.G. Scherer, A. Wokaun
Methanol tolerant oxygen reduction catalysts derived from electrochemically pre-treated $Bi_2Pt_{2-y}Ir_yO_7$ pyrochlores
2nd France-Deutschland Fuel Cell Conference, Belfort, France, November 29 – December 2, 2004.
[1] UMIST, Manchester, UK

L. Gubler, N. Prost, S. Alkan Gürsel, D. Kramer, G.G. Scherer
Radiation grafted proton exchange membranes based on ETFE-g-polystyrene for low temperature fuel cells
Solid State Proton Conductors – 12, Uppsala, Sweden, August 15-19, 2004.

M. Hahn
The evolution of the electrical double layer in nanoporous electrodes
GDCH-Tagung, Angew. Elektrochemie, Graz, Austria, September 8-10, 2004.

L. Hardwick
Detection of surface disorder on graphite electrodes using Raman microscopy
GDCh-Tagung, Angew. Elektrochemie, Graz, Austria, September 8-10, 2004.

M. Holzapfel
The study of graphite negative electrodes for lithium-ion batteries with the help of in situ X-ray diffraction methods
SLS Users' Meeting 2004, PSI Villigen, October 4-5, 2004.

R. Kötz
Charge-induced dimensional changes in electrochemical double layer capacitors
14th International Seminar on Double Layer Capacitors and Hybrid Energy Storage Devices, Deerfield Beach, USA, December 6–8, 2004.

D. Kramer
Two-phase flow and electrochemical characteristics of polymer electrolyte fuel cells investigated by in situ neutron imaging
Fuel Cells – Science & Technology, Munich, Germany, October 6-7, 2004.

D. Kramer
Untersuchung von Flutungseffekten und zweiphasiger Strömung in PEFC mittels Neutronenradiographie
Workshop „Neue Perspektiven der Brennstoffzellen-technologie", Glaubitz, Germany, November 9, 2004.

D. Kramer (given by K.N. Clausen)
On-line studies of electric fuel cell assemblies by neutron imaging methods
American Conference on Neutron Scattering, College Park, Maryland, USA, June 6-10, 2004.

D. Kramer (given by E. Lehmann)
The on-line study of the fuel cell behaviour with thermal neutrons
ITMNR-5, Garching, Germany, July 26-30, 2004.

H. Kuhn, B. Andreaus, A. Wokaun, G.G. Scherer
Electrochemical impedance spectroscopy applied to polymer electrolyte fuel cells with a pseudo reference electrode arrangement
6th International Symposium on Electrochemical Impedance Spectroscopy, Cocoa Beach, Florida, USA May 16-21, 2004.

M.J. Montenegro, M. Döbeli[1], T. Lippert, S. Müller[2], A. Weidenkaff[3], P.R. Willmott[4], A. Wokaun
Can thin perovskite film materials be applied as model systems for battery applications
E-MRS Symposium Laser Interactions in Materials: Nanoscale to Mesoscale, Strasbourg, France, May 2004.
1 ETH Zürich and PSI
2 Euresearch, Bern
3 University of Augsburg, Germany
4 University of Zürich and PSI

M. Santis, F.N. Büchi
Optimization of current density distribution in polymer electrolyte fuel cells of technical relevance
55th Annual ISE Meeting, Thessaloniki, Greece, September 19-24, 2004.

G.G. Scherer, P. Dietrich
Globale Mobilitätsbedürfnisse und ein potenzieller Lösungsansatz für die individuelle Mobilität
Energie Apéro Mobilität, Lenzburg, January 27, 2004.

G.G. Scherer
Chancen und Risiken von Polymerelektrolyt-Brennstoffzellen – Systeme für den Einsatz im Hausbereich
novatlantis bauforum: Brennstoffzellen, Bio-Informatik und Nanotechnologie – Von der Hoffnung zur Realität: Technologien, Produkte und Komponenten für zukunftsfähige Gebäude, Basel, November 18, 2004.

I.A. Schneider, H. Kuhn, A. Wokaun, G.G. Scherer
Ortsaufgelöste Impedanzspektroskopie an Polymerelektrolyt-Brennstoffzellen
Kronacher Impedanztage 2004, Kronach, Germany, May 3-5, 2004.

I.A. Schneider, H. Kuhn, A. Wokaun, G.G. Scherer
Fast locally resolved electrochemical impedance spectroscopy in polymer electrolyte fuel cells 2004
Joint International Meeting of the Electrochemical Society, Honolulu, Hawaii, October 3-8, 2004.

J. Ufheil
Maleic anhydride as film-forming electrolyte additive in gamma butyrolactone solutions based lithium-ion batteries
5th Advanced Batteries and Accumulators – ABA-2004, Brno, Czech Republic, June 12-16, 2004.

J. Vetter
Understanding the graphite failure mechanism in lithium-ion batteries: A multiple technique approach
206th Electrochem. Soc. Meeting, Hawaii, USA, October 3-8, 2004.

J. Wambach
The SLS Infrared beamline; progress report
SLS-SAC Meeting, PSI SLS, September 26, 2004.

J. Wambach
Katalyseforschung, Schwingungsspektroskopie und die Infrarot-Strahllinie: Einblick in die Dynamik der Moleküle
PSI Herbstschule, October 6, 2004.

A. Würsig
Electrolyte degradation and film formation on positive electrodes of Li-ion batteries: An in situ DEMS study
205th Electrochem. Soc. Meeting, San Antonio, Texas,

POSTERS

S. Alkan Gürsel, C. Padeste, H.H. Solak, G.G. Scherer
Microstructured polymer films by X-ray lithographic exposure and grafting
IRaP 2004, 6th International Symposium on Ionizing Radiation and Polymers, Houffalize, Belgium, September 25-30, 2004.

S. Alkan Gürsel, C. Padeste, H.H. Solak, G.G. Scherer
Preparation of microstructured polymer films and membranes
20th Anniversary Meeting, Polymer Group of Switzerland (PGS), ETH Zürich, November 12, 2004.

S. Alkan Gürsel, L. Gubler, G.G. Scherer
ETFE based radiation grafted membranes for low temperature fuel cells
20th Anniversary Meeting, Polymer Group of Switzerland (PGS), ETH Zürich, November 12, 2004.

M. Bosco, T.-B.Truong, E. De Boni, F. Vogel, F. Hajbolouri, G.G. Scherer
"Shift-less" fuel processing unit to produce hydrogen from gasoline for fuel cell systems
15th World Hydrogen Energy Conference, Session 5-4, Hydrogen from Fossil Fuels, Yokohama, Japan, June 27 - July 2, 2004.

H. Buqa, A. Würsig, D. Goers, P. Novák, F. Krumeich[1], M.E. Spahr[2]
Behavior of highly crystalline graphites in lithium-ion cells with propylene carbonate containing electrolytes
12th Int. Meeting on Lithium Batteries, Nara, Japan, June 27 – July 2, 2004.
[1] ETH Zürich
[2] TIMCAL SA, Bodio

F. Campana, R. Kötz, P. Novák, H. Siegenthaler[1]
In situ AFM-measurement of the intercalation/de-intercalation process of Li^+-ions in organic electrolyte solution
International Conference on Electrified Interfaces 2004, Spa, Belgium, July 11-16, 2004.
[1] University of Bern

Th. Dumont, R. Bischofberger[1], T. Lippert, A. Wokaun
Gravimetric and profilometric measurements of the ablation rates of photosensitive polymers at different wavelengths
E-MRS Symposium Laser Interactions in Materials: Nanoscale to Mesoscale, Strasbourg, France, May 2004.
[1] applied microSWISS GmbH, Buchs

Th. Dumont, R. Bischofberger[1], T. Lippert, A. Wokaun
Gravimetric and profilometric measurements of the ablation rates of photosensitive polymers at different irradiation wavelengths
20th Anniversary Meeting, Polymer Group of Switzerland (PGS), ETH Zürich, November 12, 2004.
[1] applied microSWISS GmbH, Buchs

S.A. Freunberger, F.N. Büchi
Model approaches for the description of lateral effects in large scale PEFC
9th Ulm ElectroChemical Talks, Ulm, Germany, May 17-18, 2004.

L. Gubler, R. Wälchli[1], R. Randegger[1], G.G. Scherer
Water management aspects of radiation grafted fuel cell membranes
Fuel Cell Science & Technology, Munich, Germany, October 6-7, 2004.
[1] ETH Zürich

F. Hajbolouri, G.G. Scherer, T. Vad[1], S. Abolhassani-Dadras, B. Schnyder, M. Horisberger, A. Wokaun
Characterization of co-sputtered Pt/C-films deposited by DC magnetron sputtering
SAOG 2004, Fribourg, January 30, 2004.
[1] FZ Jülich, Germany

D. Kramer, J. Zhang[1], R. Shimoi[1], E. Lehmann, A. Wokaun, K. Shinohara[1], G.G. Scherer
In situ diagnostic of two-phase flow phenomena in polymer electrolyte fuel cells by neutron imaging
Gordon Research Conference on Fuel Cells, Bristol RI, USA, July 25-30, 2004.
[1] Nissan Motor Co. Ltd, Yokohama, Japan

J. Krüger[1], S. Martin[1], H. Mädebach[1], L. Urech, T. Lippert, A. Wokaun, W. Kautek[1]
Femto- and nanosecond laser treatment of doped polymethylmethacrylate
E-MRS Symposium Laser Interactions in Materials: Nanoscale to Mesoscale, Strasbourg, France, May 2004.
[1] Federal Institute for Materials Research and Testing, Berlin, Germany

H. Kuhn, B. Andreaus, I. Schneider, G.G. Scherer, A. Wokaun
Simultaneous locally resolved electrochemical impedance spectroscopy in polymer electrolyte fuel cells
6th International Symposium on Electrochemical Impedance Spectroscopy, Cocoa Beach, Florida, USA May 16-21, 2004.

M. Kuhnke, T. Lippert, G.G. Scherer, A. Wokaun
Microfabrication of flow field channels in glassy carbon by a combined laser and reactive ion etching process
9th International Conference on Plasma Surface Engineering, Garmisch-Partenkirchen, Germany, September 2004.

T. Lippert, J. Bonse[1] ,S.M. Wiggins[1], J. Solis[1]
Phase change dynamics in a polymer thin film upon femtosecond and picosecond laser irradiation
E-MRS Symposium Laser Interactions in Materials: Nanoscale to Mesoscale, Strasbourg, France, May 2004.
[1] CSIC, Madrid, Spain

G.G. Scherer, S. Alkan Gürsel, M. Slaski, D. Kramer, A. Wokaun, L. Gubler
Radiation grafted membranes for polymer electrolyte fuel cells: State of the art at Paul Scherrer Institut
Fuel Cell Seminar, San Antonio, USA, November 1-5, 2004.

L. Urech, M. Hauer, T. Lippert , C.R. Phipps[1], A. Wokaun, I. Wysong[2]
Designed polymers for laser-based microthrusters – correlation of thrust with material, plasma, and shockwave
Polymer Sciences in Switzerland Symposium of the Swiss Polymer Society, Zürich, November 2004.
[1] Photonic Associates, Santa Fe, USA
[2] EOARD London, UK

J. Vetter, H. Buqa, M. Holzapfel, P. Novák
Impact of co-solvent chain branching on lithium-ion battery performance
12th Int. Meeting on Lithium Batteries, Nara, Japan, June 27 - July 2, 2004.

PATENT APPLICATIONS

H. Buqa, S. Peter, J. Vetter, P. Novák
A non-aqueous electrolyte for a rechargeable electrochemical cell
Patent Application No. EP 04 006 038.6, 2004.

C. Jost[1], M. Holzapfel, P. Novák, A. Prodi-Schwab[1], V. Hennige[1], Ch. Hying[1]
Elektrolytzusammensetzung sowie deren Verwendung als Elektrolytmaterial für elektrochemische Energiespeichersysteme
Patent Application No. DE 10 2004 018 929.3, 2004.
[1] Degussa AG, Marl, Germany

F.-M. Petrat[1], M. Holzapfel, P. Novák
Nanoskalige Siliziumpartikel in negativen Elektrodenmaterialien für Lithiumionen-Batterien
Patent application No. DE 10 2004 016 766.4, 2004
[1] Degussa AG, Marl, Germany

CONFERENCES, WORKSHOPS & EXHIBITIONS

R. Kötz
1st European Symposium on Supercapacitors & Applications,
Belfort, France, November 4-5, 2004.
Member, International Scientific Committee

T. Lippert
E-MRS 2004 Conference Symposium on Laser Interactions in Materials: Nanoscale to Mesoscale
Strasbourg, France, May 2004.
Member, International Advisory Committee

T. Lippert
3rd International Conference on Mathematical Modeling and Computer Simulation of Material Technologies –MMT 2004
Ariel, Israel, September 2004.
Member, International Advisory Committee

P. Novák
International Scientific Committee of the "International Meeting on Lithium Batteries" conferences
Member

M. Santis, A. Tsukada, F.N. Büchi
PowerPac, a portable fuel cell system
Impulstag Brennstoffzellen, Biel, November 12, 2004.
Exhibitors

G.G. Scherer
2nd France-Deutschland Fuel Cell Conference
Belfort, France, November 29 – December 2 (2004).
Member, Scientific Committee

G.G. Scherer
European Fuel Cell Forum
Member, Advisory Board

MEMBERSHIPS IN EXTERNAL COMMITTEES

F.N. Büchi
International Society of Electrochemistry
Regional Representative Switzerland

R. Kötz
International Society of Electrochemistry
Chair of Div. 3, Electrochemical Energy Storage and Conversion

T. Lippert
E-MRS
Board of Delegates

T. Lippert
European Science Foundation, Assessement for extraploratory workshops
External Expert

P. Novák
International Society of Electrochemistry
Member of Executive Committee (Treasurer) and Council

P. Novák
Alexander von Humboldt Foundation
External Expert

G.G. Scherer
Neuartige Schichtstrukturen für Brennstoffzellen
Deutsche Forschungsgemeinschaft, Mitglied der Prüfungsgruppe für das Schwerpunktprogramm

G.G. Scherer
Beirat Forschungsallianz Brennstoffzellen Baden-Württemberg, Germany
Deputy Speaker

G.G. Scherer
Maturitätsprüfungskommission der Kantonsschulen Baden, Wettingen und Wohlen
Mitglied

G.G. Scherer
MISTRA, The Swedish Foundation for Strategic Environmental Research
Member International Advisory Board

SCIENTIFIC CONTRIBUTIONS FROM THE ELECTROCHEMISTRY LABORATORY FOR THE PSI SCIENTIFIC REPORT 2004 VOLUME V, GENERAL ENGERGY, ISSN 1423-7342

Please note that the following page numbers refer to the original page numbers in the PSI Scientific Report 2004, Volume V, General Energy.

Please cite the following contributions as indicated:

Author, Title, ISSN No., page

For example:

P. Dietrich
CONCEPT AND DESIGN OF THE HY-LIGHT® FUEL CELL VEHICLE
PSI Scientific Report 2004 / Volume V, ISSN 1423-7342, p. 91

CONCEPT AND DESIGN OF THE HY-LIGHT® FUEL CELL VEHICLE

P. Dietrich, D. Laurent (Michelin)

To demonstrate the potential of electrical powertrain technologies for a more sustainable mobility Michelin and PSI joined forces to realize a passenger vehicle on a white sheet of paper approach to maximize the opportunities of a polymer electrolyte fuel cell system and a pure electrical powertrain. The concept vehicle HY-LIGHT has been presented in October 2004 in Shanghai at the "Challenge Bibendum". PSI developed the fuel cell system and the double layer capacitor unit and Michelin was responsible for the development and realisation of all other components and systems of the HY-LIGHT.

1 INTRODUCTION

Since the mid 1990ies the research and development of passenger car vehicles has produced a variety of different concepts based on a fuel cell systems as the source for the electrical power to drive the vehicle. Some of these vehicles were fuelled by methanol, others had hydrogen stored on board, as compressed gas or as a cryogenic liquid. All these cars used oxygen from the air for the electro-oxidation of the fuel [1]. Tremendous progress has been made in reducing the volume needed for the fuel cell system and the storage of the fuel. Therefore cars without interference of the powertrain with the passenger compartment and offering the volume in trunk space the customer expects have been developed.

If the different cars are compared it can be seen, that the mass of the vehicles is still significantly higher than those of vehicles which are equipped with internal combustion engines.

2 CONCEPT OF THE HY-LIGHT

The purpose of the vehicle was to reflect the possibilities of a white paper approach for a car which is propelled by electricity.

The production of the electrical power is realized by a fuel cell system. The electricity can be transported by cables within the car quite flexibly. The power electronics adjust the current for the electric motors. These motors generate the mechanical energy to drive the car, but also to control the suspension and to manage the chassis stability. The power transfer by electrical cables offers flexibility to allocate space differently and more efficiently.

Another aim was to combine several functions within one part to reduce the mass of the vehicle. The light weight approach helps to reduce resources for the production of the vehicle, but even more important, mass is the most important single factor for fuel consumption.

Combining all these aims, the vehicle shall be a light weight vehicle, purpose designed for the most efficient fuel transformer which is a fuel cell system. The vehicle shall be a 4 seater and have a reasonable range.

Fig. 1: The concept car HY-LIGHT with light weight construction, fuel cell system and advanced in wheel electric motors for driving and suspension control.

3 DESIGN OF THE HY-LIGHT

The key specifications of the vehicle are shown in Table 1.

The structure of the chassis is based on an aluminium structure, with integrated storage tank for the hydrogen. The fuel cell system is positioned in the front compartment. The power electronics are located between the driver and the front passenger.

To cover the peak power demand and to profit from the characteristics of the electric motors to recuperate braking energy, a double-layer-capacitor is integrated in the system.

Two in-wheel motors in the front wheels are driving the vehicle. With a further electromotor in each of the four wheels the suspension is controlled as well as the relative position of the chassis to the road.

The vehicle is shown in Figure 1.

	value	unit
Curb weight	850	kg
Top speed	130	km/h
Acceleration 0-100 km/h	<12	sec
Vehicle range*	400	km
Seating capacity	4	passenger
Emissions	No	Local pollutants

* At a constant speed of 80 km/h

Table 1: Main characteristics of the fuel cell driven concept car HY-LIGHT.

4 FUEL CELL SYSTEM

The vehicle includes a polymer electrolyte fuel cell system, which is transforming hydrogen and oxygen into electricity.

The system delivers continuously 30 kW electrical DC-power output. The change from air to pure oxygen as oxidation medium offers the possibility to reduce the auxiliaries, increase power density and enhance the dynamics of the fuel cell system.

5 FUEL STORAGE

The hydrogen and the oxygen are stored as compressed gases up to 350 bars.

The storage of the hydrogen is integrated in the floor of the vehicle. The construction is based on small volume tubes which are connected by capillaries [2]. This construction offers a high stiffness of the structure of the chassis and prevents the storage from exploding in case of an injury-damage by an accident. The storage will be discharged in a controlled way, limited by the flow through the capillaries. The principle is shown in Figure 2.

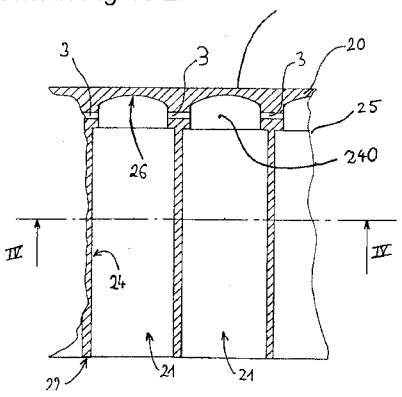

Fig. 2: Principle of the hydrogen storage which is an integral structure of the chassis.

The oxygen is stored in a tank which is located below the rear seats.

The fuelling of the hydrogen and oxygen is made at two locations at the vehicle, but for further developments it can be imagined that the fuelling can be realized with a combined fuelling adapter.

6 ELECTRICAL POWERTRAIN

The development of highly efficient power electronics and compact electric motors opens up a new approach of in wheel motors for traction power. The vehicle is equipped with 2 wheel motors of 30 kW with a mass of 7 kg each, keeping the unsprung mass small.

A second electric motor is integrated in each wheel to realize an electric suspension control. These same motors can also be used for electric anti-roll and anti-pitch control. This offers new safety and comfort in curve-driving. The arrangement can be seen in Figure 3. The power electronics to control the motors are located between the front seats.

Fig. 3: View of the wheel with integrated electric motor for active suspension and chassis control with anti-roll and anti-pitch functions. In the same wheel the electric motor for propulsion and electric braking is integrated.

7 SHORT TIME ENERGY STORAGE

To fulfil the maximal power demand for cruising and acceleration, a module of double-layer-capacitors (supercaps) is added to the electrical circuit.

The developed module can deliver or recover up to 32 – 45 kW for 15 – 20 seconds. This is enough to collect most of the braking energy in average driving and to deliver additional power for the acceptable performance of the vehicle. The advantage of the supercap module is its ability to be charged and discharged in a way compatible with a passenger car's life time.

8 ACKNOWLEDGEMENT

The project was a collaboration between Michelin and PSI. Financial support by Michelin is gratefully acknowledged by PSI.

9 REFERENCES

[1] W. Vielstich, A. Lamm, H. A. Gasteiger, Handbook, John Wiley & Sons, ISBN 0-471-49926-9, Fuel Cells **4**, 1163-1198 (2003).

[2] European patent application EP 1 431 096 A2, Réservoir pour le stockage à haute pression d'un carburant sur un véhicule (2002).

ON THE EFFICIENCY OF H_2 / O_2 AUTOMOTIVE PE FUEL CELL SYSTEMS

F.N. Büchi, S.A. Freunberger, M. Reum, A. Delfino (Michelin)

The use of pure oxygen, instead of air, has a prominent influence on the power density and the efficiency of polymer electrolyte fuel cell systems. The main differences are the superior specific power in the stack and the greatly reduced parasitic power in the balance of plant of the oxygen vs. the air system. The analysis shows that for a vehicle application the tank to power efficiency of the oxygen system is higher by about 20 percentage points than that of the air system. When including the well to tank energy requirement of oxygen, the efficiency advantage of the oxygen system is reduced, but still significant.

1 INTRODUCTION

Efficiency is the key argument for the application of polymer electrolyte fuel cells in automotive applications. The efficiency of the fuel cell system depends on a number of interdependent parameters. These are on the one hand the properties of the electrochemical components as well as the chosen operating conditions, i.e. gas pressures, gas compositions and cell temperature. On the other hand efficiency of the complete system also strongly depends on the characteristics of the balance of plant components (BoP).

It seems probable, that future production of hydrogen will go through routes of water splitting either by electrolysis or thermochemical pathways. Pure oxygen will be a byproduct of those hydrogen generation processes. This opens up the possibility to use pure oxygen instead of air for the conversion of hydrogen to electricity in fuel cells. This paper investigates the use of pure oxygen on overall fuel cell system efficiency for the automotive application as compared to air.

2 EFFICIENCY CONSIDERATIONS

Losses occurring through overvoltages in the cell reaction and parasitic power in the BoP reduce the theoretically high efficiency of conventional H_2/air low temperature fuel cell systems in the automotive application. The main sources of the losses, and thus the main potential efficiency gains are the following:

1) Electrocatalytic overvoltage of the oxygen reduction reaction (ORR) at the cathode.
2) Ohmic overvoltage of the membrane.
3) Power consumption of the balance of plant.

Items 1) and 2) call for improvement in the fuel cell stack. Item 3) has to be optimized within the complete fuel cell system concept. For all of these three main losses in the fuel cell system, improvement is possible, if, instead of air, pure oxygen is used as the oxidant.

The use of pure oxygen reduces the ORR overvoltage, as the oxygen partial pressure can easily be increased from typically 0.4 bar by an order of magnitude.

The use of pure oxygen also eliminates the need for an air compressor, the main power consumer in the BoP.

3 STACK POWER DENSITY

The power density of the fuel cell stack is strongly dependent on the specific power in the active area. Figure 1 shows the relative increase of cell voltage as function of oxidant and gas pressure relative to the base case of H_2/air at 2bar(abs), a condition typical for automotive systems. It can be seen that at 1 A/cm^2, almost a 30% increase in specific performance and efficiency can be obtained by the use of pure oxygen and a moderate pressure increase. Results in Figure1 have been obtained under conditions of low gas hu-

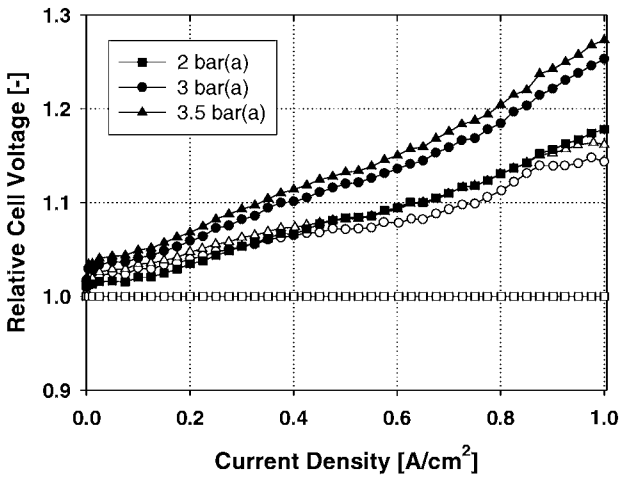

Fig. 1: Relative performance of cell of technical size for operation with H_2/O_2 (■●▲) and H_2/air (○△) relative to H_2/air at 2 bar_a (□) as the base case.

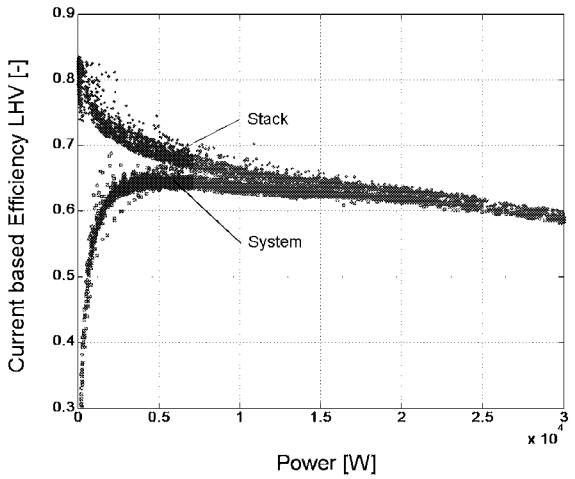

Fig. 2: Fuel cell stack and fuel cell system efficiency of the HY-LIGHT H_2/O_2 fuel cell system as function of net power. Data obtained in car.

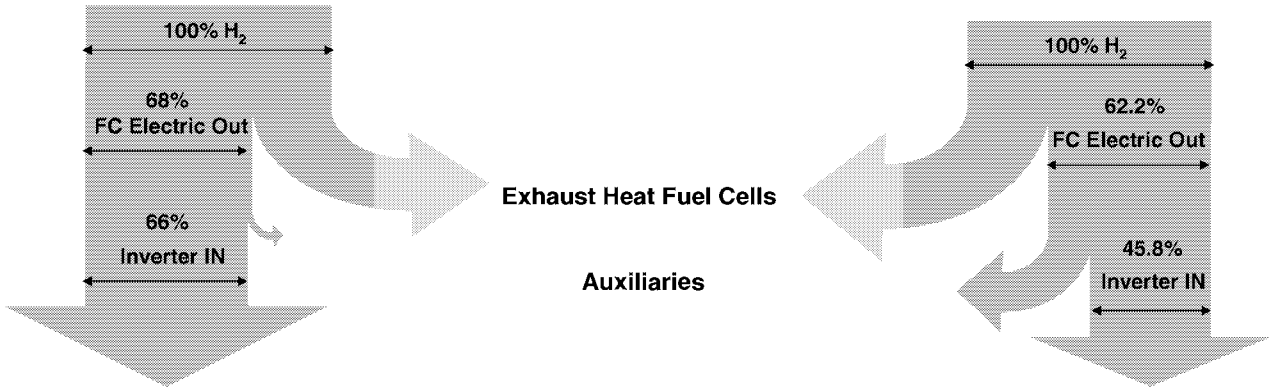

Fig. 3: Tank to electric power efficiencies of automotive fuel cell power trains. Left: HY-LIGHT H_2/O_2 32 kW peak power system for average power of 7 kW, data obtained on the road in arbitrary driving cycle. Right H_2/air, 55 kW peak power system, for average power of 12 kW, data obtained for NEFZ [1].

midification (gas dew points 45 °C at a cell temp. of 74 °C), therefore in addition to the reduction of the catalytic losses, also reduction of membrane resistance contributes to the efficiency gain.

4 SYSTEM EFFICIENCY

In conventional automotive systems, typically 15 – 20% of the stack power are lost for the operation of the BoP, the main power consumer being the air compressor. Typical tank to electric power efficiencies are in the order of 45% [1, 2].

The use of pure oxygen as the oxidant increases the cell efficiency at the same current density (Figure 1) and requires greatly reduced BoP parasitic power. The tank to electric power efficiency of the oxygen system exceeds 60 % over almost the entire power range (see Figure 2). In Figure 3 fuel cell power trains for the automotive application are compared. At an average of 22% of rated load, the oxygen fed power train has an efficiency advantage of 20 percentage points.

5 THE ENERGETIC COST OF OXYGEN

The use of pure oxygen is energetically not for free. Pure oxygen has to be produced and compressed. Table 1 gives an overview on the energetic cost. If hydrogen is produced by the natural gas route then oxygen has to be separated from air. The most common, industrial process is distillation of liquid air. Oxygen with high purity can also be obtained by pressure swing adsorption. If hydrogen is obtained from splitting of water, today electrolysis is the preferred process, in future thermochemical ways might be preferably used, normally the total energetic cost of the process is attributed to the hydrogen fuel. Therefore pure oxygen is obtained for free and only the energetic cost for compression has to be paid. Table 1 shows, that in case of water splitting only 0.15 kWh/Nm^3 are required. With high pressure electrolysis (200 bar) it could even be less.

The energetic cost of oxygen can be included in the fuel cell system efficiency calculation. In case of fossil hydrogen and oxygen obtained from liquid air the tank to electric power efficiency for the case in Figure 3 is reduced from 66% to 55%. In case of electrolytic hydrogen and oxygen the reduction is from 66% to 63%.

Method	Production [kWh/Nm^3]	Compression [kWh/Nm^3]	Total [kWh/Nm^3]
Distillation of liquid air	0.25 – 0.3	0.3	0.6
Pressure swing ads.	0.4 – 0.5	0.3	0.8
Electrolysis 30 bar	0	0.15	0.15

Table 1: Energy required for production and compression of pure oxygen to 350 bar.

The results show that in case of fossil hydrogen, the total efficiency of a H_2/O_2 system might be in the range of future, highly advanced H_2/air systems, in case of electrolytic hydrogen however the efficiency of the H_2/O_2 system is clearly superior.

6 ADVANTAGES OF PURE OXYGEN VS. AIR

The advantages of using pure oxygen vs. air can be summarized as follows:

- *At fuel cell level*: higher power density, lower platinum requirement, higher efficiency, no possible poisoning due to poor ambient air quality.
- *At system level*: higher system efficiency, easier humidity management, decreased noise, high dynamics of the fuel cell system.
- *At vehicle level*: Higher fuel efficiency, higher range, global weight reduction up to ca. 500 - 700 km range.

7 ACKNOWLEDGEMENT

The project was a collaboration between Michelin and PSI. Financial support by Michelin is gratefully acknowledged by PSI.

8 REFERENCES

[1] G. Friedelmeier, J. Friedrich, F. Panik, Fuel Cells **2**, 92 (2001).

[2] F. N. Büchi et al., PSI Scientific Report 2002, **V**, 102 (2003).

FUEL EFFICIENCY OF THE HY-LIGHT FUEL CELL CAR AT THE 2004 BIBENDUM CHALLENGE

G. Paganelli, A. Tsukada, F.N. Büchi, D. Walser (Michelin), P.A. Magne (Michelin), D. Laurent (Michelin)

The HY-LIGHT fuel cell vehicle has been developed in collaboration between Michelin and the PSI. This vehicle has been unveiled at the 2004 Bibendum challenge in Shanghai, China. During this event, fuel efficiency has been measured on a 2 hour drive on the Shanghai formula 1 circuit. An outstanding 0.679 kg H_2 / 100km (2.52 l_{ge}/ 100km gasoline equivalent) fuel efficiency has been demonstrated.

1 INTRODUCTION

The HY-LIGHT fuel cell vehicle has been developed by Michelin in collaboration with the Paul Scherrer Institute to demonstrate a satisfactory solution meeting the urgent need for clean mobility. A strong effort has been dedicated to achieve exceptional tank to wheel efficiency in this hydrogen powered car. Performance in this aspect is favourable to vehicle range. This also improves global well to wheel efficiency balance in case hydrogen is produced out of non-renewable fossil fuels. In the most probable scenario where renewable energy is used, the generating system size is reduced.

2 THE VEHICLE

The HY-LIGHT is equipped with the Michelin *active wheel* which embeds an electric actuator for programmable active suspension and chassis control functions and, for the two front wheels 30kW / 60kW nominal/peak power 7 kg electric motors for traction. The vehicle is powered by a 30 kW PEFC fuel cell supplied by compressed hydrogen, stored within the chassis, and compressed oxygen. Supercapacitors have been combined to the primary power source in order to recover braking energy and also to assist the fuel cell for peak power demands. Furthermore this hybridization offers opportunities to optimize power flows within the vehicle. The HY-LIGHT weighs only 850 kg, and special provisions have been made to reduce air drag such as flat bottom, electronic mirror and optimized cooling system integration.

3 FUEL EFFICIENCY RESULTS

The fuel efficiency test has been run on the Shanghai International Circuit during the 2004 Bibendum Challenge. Beginning from a cold start, competitors had to average 70 km / h over 24 laps (130 km) on a track with several sharp curves, forcing the drivers to decelerate and accelerate many times simulating real world traffic, see Figure 2.

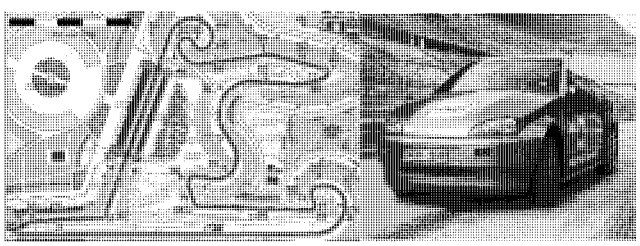

Fig. 1: Shanghai formula 1 circuit and the HY-LIGHT.

Based on tank pressure depletion, temperature and the Van der Waals equation of state, the hydrogen consumption over the entire test has been evaluated to 679 g / 100 km (2.52 l_{ge}/ 100km gasoline equivalent). Fuel cell current integration, using Faraday's constant, yields to a hydrogen consumption of 676 g / 100km. This agrees almost perfectly with the previous result due to extremely limited hydrogen purges leading to a hydrogen utilization of over 99%.

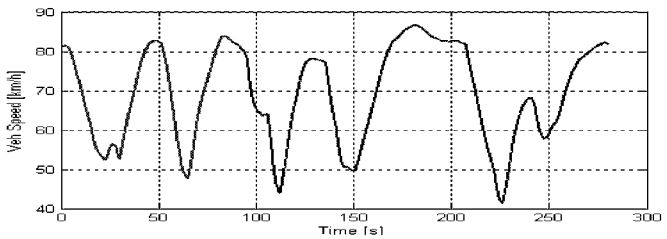

Fig. 2: Vehicle speed over one lap.

The supercapacitors are operated in a charge sustaining fashion. Therefore their contribution as energy source is negligible. The mere 650 kJ maximum usable energy stored in the supercapacitors represents anyhow less than 1% of the energy used over the test. On the other hand, the contribution of the supercapacitors as energy buffer is significant. A negative (braking) energy recovery capacity at wheel of 2.3 kWh over 100 km is available. Accounting for conversion and supercapacitor charge-discharge efficiency this recoverable energy translates to 1.75 kWh energy actually recovered as shown in Figure 3. Mean fuel cell efficiency being 63%, 2.8 kWh have consequently been saved in hydrogen over 100 km corresponding to a saving of 12% of the fuel used. This contributes greatly to the exceptional tank-to-wheel efficiency of 60%. This efficiency does not include the energetic cost of oxygen as discussed in the previous article.

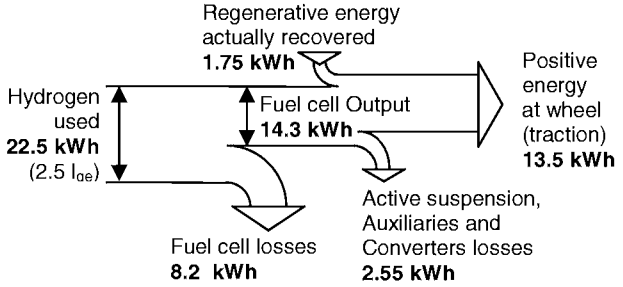

Fig. 3: Balance of energy flows over 100 km.

4 ACKNOWLEDGEMENT

The project was a collaboration between Michelin and PSI. Financial support by Michelin is gratefully acknowledged by PSI.

DYNAMIC PERFORMANCES OF THE HY-LIGHT HYDROGEN / OXYGEN PEFC

G. Paganelli, S.A. Freunberger, F.N. Büchi, A. Delfino (Michelin), D. Laurent (Michelin)

The HY-LIGHT fuel cell vehicle has been developed in collaboration between Michelin and the PSI. As opposed to the usual scheme, the fuel cell of this vehicle is supplied with pure oxygen. One of the numerous advantages obtained is the exceptional ability of the fuel cell system to follow fast power changes.

1 INTRODUCTION

In collaboration between Michelin and the Paul Scherrer Institut, a very advanced fuel cell vehicle, named HY-LIGHT, has been developed. The HY-LIGHT is equipped with the Michelin *active wheel* which embeds an electric actuator for programmable active suspension functions for the two front wheels and brushless 30kW/60kW nominal/peak power electric motors for traction. A highly dynamic power source is essential to supply such an electric drive train. This 850 kg vehicle is powered by a 30 kW PEFC fuel cell. Presence of supercapacitors insures part of the dynamic requirement. However, fast fuel cell power change is also possible in the HY-LIGHT, insuring extremely rapid excursion on the total power available in the vehicle. Usually, the oxygen needed to oxidize the hydrogen in a fuel cell is taken from the air by way of a compressor. In the HY-LIGHT, a completely different approach is used: pure oxygen is stored in a pressurized tank. This leads to significant advantages, one of them being outstanding fuel cell dynamics.

2 DYNAMIC RESULTS

In order to emphasize its dynamic capabilities, an extreme power rise from 0 to rated power (30kW) in 20ms was applied to the fuel cell system, as shown in Figure 1, top plot. This translates to a current density rise from 0 to 0.85 A/cm^2, middle plot. As can be seen on the bottom plot, the lowest cell voltage excursion during this transient stays within 100 mV of the mean cell voltage.

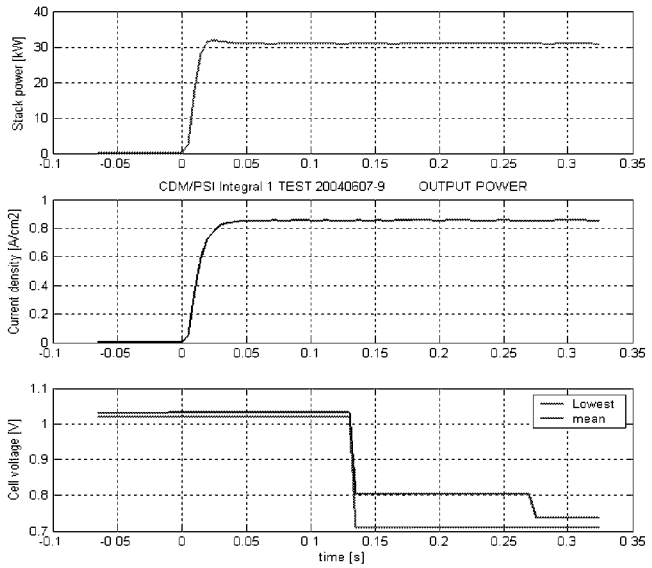

Fig. 1: Power, current density and cell voltages for 0 to 30 kW power step.

In the case of an air fed fuel cell system, the air compressor is the limiting factor in dynamic response. The reason is that time is needed to accelerate the moving parts within the compressor in order to satisfy the rising air mass flow demand. Consequently several 100 ms to some seconds are typically necessary to reach rated power [1]. The absence of an air compressor in pressurized oxygen fed systems is therefore a major advantage for dynamic operation. There is no lag in oxygen supply because pressurized oxygen is always available. The limiting factor becomes the pressure regulator valve. Nevertheless these components exhibit considerably less lag than compressors. Highly dynamic power change with minimal pressure excursions is therefore no problem as shown in Figure 2. The power step corresponds to a gas consumption change from 0 to 300 standard liters per minute (SLPM) and 150 SLPM respectively for hydrogen and oxygen in 20 ms. As can be observed, the deviation of the inlet pressure, which is the controlled pressure, does not exceed 100 mbar. Outlet pressure decrease is a normal consequence of increased pressure drop within the stack due to the higher mass flow.

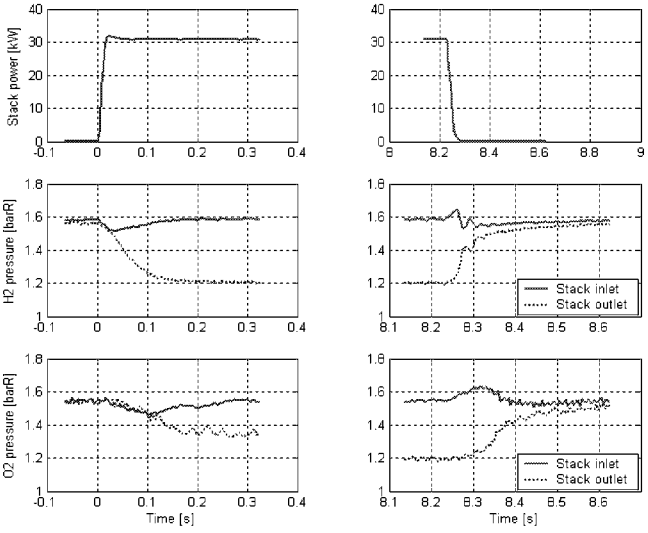

Fig. 2: Pressure response of gases to positive power step (left) and negative power step (right).

3 ACKNOWLEDGEMENT

The project was a collaboration between Michelin and PSI. Financial support by Michelin is gratefully acknowledged by PSI.

4 REFERENCE

[1] P. Treffinger, H.E. Friedrich, A. Brinner, F. Philipps, *Innovative Power Train Systems*, VDI-Berichte 1852, Düsseldorf, 551 (2004).

EFFECT OF RIPPLE-CURRENTS ON LARGE CELL SUPERCAPACITORS

J.-C. Sauter, R. Kötz

The effect of high frequency ripple currents on the performance and lifetime of Electrochemical Double Layer Capacitors (EDLC), also called supercapacitors, is not known. Such ripple, generated by high power electronic converters, are superimposed on the capacitor in electronic circuits such as the drive train for an electric hybrid vehicle. We have tested the degradation of EDLCs at nominal voltage with and without superimposed ripple currents. Our results indicate that the EDLCs are not affected.

1 INTRODUCTION

Electrochemical Double Layer Capacitors (EDLC) also called supercapacitors [1], are frequently used as power assist and short term storage devices in electrical drive trains for e.g. hybrid electric vehicles (HEV) such as the HY.POWER or HY-LIGHT vehicles developed at PSI with various partners. In such applications high power electronics is used for matching voltages of the different components. Such high power electronics, which chop the current, introduce so-called ripple currents into the circuits and its components. It was the aim of the performed tests to asses whether such high frequency currents affect the lifetime of the EDLCs.

2 EXPERIMENTAL

Two capacitor strings with five BCAP010 (2600 F, 2.5 V) in series were tested at constant voltage of 12.5 V. While one string was kept at DC voltage, an additional current was overlaid for the second string with a frequency of 1kHz and amplitude of ±10 Amp. The capacitance and the equivalent series resistance (ESR) of both strings and of the individual capacitors were measured in certain time intervals. The capacitance was determined from the charge time at constant current and the ESR at 1 kHz via a current interruption technique.

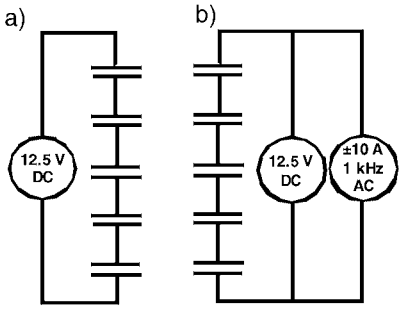

Fig. 1: Sketch of the test circuit for the two capacitor strings. a) reference, b) with rippel current.

3 RESULTS

Figure 2 shows the measured capacitance and ESR of the two strings. The capacitance of both strings decreases with an average rate of <0.5 F/day independent of whether a ripple current was applied or not. The measured decay is in good agreement with other measurements performed before on similar capacitors. In addition, the ESR of the capacitors in both strings increases by < 2 µΩ/day only. Obviously, within the time of the test (2 month) a continuous ripple current of 1 kHz does not effect the lifetime of the capacitors.

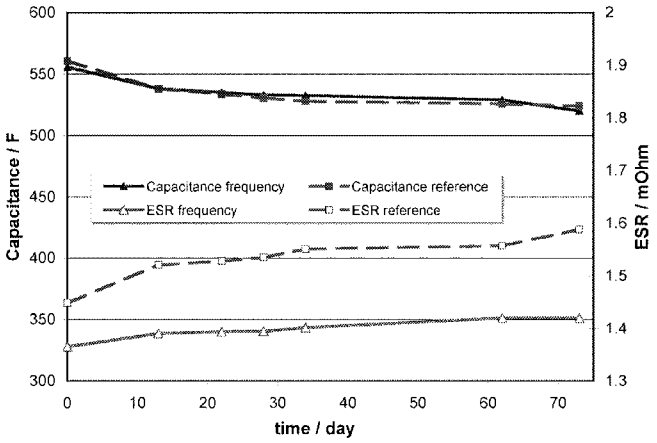

Fig. 2: Decay of capacitance and ESR for both capacitor strings with time. Full lines: Test string with ripple current (labelled 'frequency'), dashed lines: reference string. Full symbols: capacitance, open symbols: ESR @ 1 kHz.

The applied currents of 20 Amp peak-peak are of the same magnitude as the currents generated by the high power electronics in the HY.POWER fuel cell car, where ripple currents were limited to 5 % of the rated supercapacitor current (600 Amp).

However, the frequency of the ripple currents in modern power electronics is higher in the order of 10 to 15 kHz [2]. Due to experimental limitations we applied a frequency of only 1 kHz. On the bases of impedance measurements on EDLCs, however, it is known that the capacitor specifications do not vary significantly in this frequency range.

We therefore conclude that our measurements are also relevant for higher frequencies and that ripple currents at frequencies in the kHz range with moderate peak currents (5 % of rated current) do not affect the lifetime of large can EDLCs.

4 REFERENCES

[1] R. Kötz, M. Carlen, Electrochimica Acta **45**, 2483 (2000).

[2] O.Garcia, *DC/DC Wandler für die Leistungsverteilung in einem Elektrofahrzeug mit Brennstoffzellen und Superkondensatoren*, ETH Zürich, Dissertation Nr. 14859 (2002).

MODELING OF BATTERY / SUPERCAP HYBRID CARS

E. Deiss, M. Hahn, W. Scheifele, R. Kötz

Theoretical considerations have been made to investigate the benefit of supercaps as a short time power deliverer in battery/supercap hybrid cars.

1 INTRODUCTION

Supercapacitors (supercaps, SC) are electric power deliverers with a high specific power but a low specific energy compared to batteries. The question arises if it is meaningful to assemble battery cars with supercaps to overcome temporary power peaks. Calculations have been performed for a battery/supercap hybrid car concerning the optimized amount of batteries and supercaps with respect to spent energy per km. These calculations have been made on the example of Li-ion, NiMH (nickel metal hydride), NiCd, and Pb batteries in combination with supercaps. As test track five times the route Zurzach-PSI-Zurzach has been chosen with a total of 109 km and a maximum elevation of 144 m. This test track represents a route with typical hills in this region. A similar calculation has been performed over ten NEFZ cycles (Neuer Europäischer Fahrzeug Zyklus) with also a total of 109 km, but with a flat profile. The calculation was performed assuming a car of 800 kg (incl. persons) plus the mass of battery and supercaps. Braking energy recuperation has been considered in these calculations. The specific energy and power data for the storage devices are listed in Table 1.

Storage Device	Li	NiCd	NiMH	Pb	SC
Energy (Wh/kg)	130	56	65	30	4.2
$Power_{in}$ (W/kg)	350	100	85	50	10^3
$Power_{out}$ (W/kg)	700	200	170	100	10^3

Table 1: Energy and power specifications assumed for the different storage devices.

2 RESULTS AND DISCUSSION

The results are listed in Table 2 and show for the given test tracks the optimized combination of battery and supercap mass which leads to a lowest spent energy per km for the systems investigated. These data show clearly that the optimized combinations are those without supercaps, i.e. supercaps increase the spent energy per km in any case, and the batteries alone can deliver enough power.

The optimization calculations of the Zurzach-PSI-Zurzach test track only accepted those combinations of batteries and supercaps which enable a speed of 70 km at the top of the 144 m hill. This can be achieved by the batteries without supercaps, i.e. the amount of batteries needed for the distance of our test track of 109 km contain enough power for car applications except in case of Pb batteries. Due to their low specific energy and the fact that only 50 % discharge is possible the necessary Pb batteries are too heavy to complete the whole test track of 109 km. This test track also reveals that Li-ion battery cars yield the lowest spent energy per km (0.23 kWh/km) because of the high specific energy of Li-ion batteries and thus their low battery mass needed. The spent energy per km for the NiCd and NiMH battery systems with a value of 0.30 and 0.32 kWh/km is significantly higher.

The flat NEFZ test track shows similar results as the Zurzach-PSI-Zurzach test track. The Li-ion battery car needs again the lowest energy per km, much less than NiCd and NiMH. The Pb battery car needs by far most energy due to the huge battery mass required. Compared to the Zurzach-PSI-Zurzach test track the flat NEFZ test track requires less energy.

The benefit of supercaps in combination with batteries may lie in an increased cycle life of the battery which is not taken into account. Whether the frequent changes of power delivery and recuperation of a car in common traffic causes a significant cycle life reduction in a car with only batteries should be further investigated.

system	optimized battery mass (kg)	optimized supercap mass (kg)	spent energy per km (kWh/km)
a) test track: 5 times Zurzach-PSI-Zurzach (109 km)			
Li/SC	174	0	0.23
NiCd/SC	503	0	0.30
NiMH/SC	445	0	0.32
Pb/SC	test track not feasible		
b) test track: 10 times NEFZ (109 km)			
Li/SC	162	0	0.21
NiCd/SC	414	0	0.25
NiMH/SC	376	0	0.28
Pb/SC	2199	0	0.35

Table 2: Optimized combinations of battery and supercap mass which lead to the lowest spent energy per km for the two test tracks considered.

3 CONCLUSION

For two different driving cycles it has been shown that it is not advisory to assemble battery cars with supercaps as short time power deliverer. The batteries alone of a car with a range of about 100 km can deliver and recuperate enough power.

MODELING OF LATERAL EFFECTS IN LARGE SCALE PEFC

S.A. Freunberger, F.N. Büchi

Effects of cooling strategies on the performance of polymer electrolyte fuel cells (PEFC) are investigated using a numerical model. Due to the serious impact of temperature on all fuel cell processes, both the direction of the coolant stream relative to the gas streams, and its mass flow rate, turn out to significantly affect the cell performance. Besides influencing the electrochemical reaction and all kinds of mass transfer processes, temperature variations predominantly alter the local membrane hydration distribution and subsequently its conductivity.

1 INTRODUCTION

The limited coolant flow in PEFC systems leads to temperature inhomogeneities in the cell plane. This is important because the temperature profile has a serious impact on the local current generation and performance. A previously developed mathematical model for water management and current density distribution in a PEFC [1] is employed to investigate the effects of cooling strategies on cell performance. The model describes a two-dimensional slice through the cell along the channels and through the entire cell sandwich including the coolant channels and the bipolar plate. Arbitrary flow arrangements of fuel, oxidant and coolant stream directions can be described.

2 RESULTS

Dry air and moist hydrogen are fed either in parallel (co-flow) or anti parallel (counter-flow) manner into the cell. Coolant flowing in parallel with the air is denoted "positive coolant flow". In Figure 1 the effect of the coolant mass flow rate on the cell voltage for a coolant flow in positive and negative direction relative to the air stream is shown. The cases with positive coolant flow direction perform better than those with negative flow. This is because for the positive flow direction the highest temperatures occur at the saturated air outlet, whereas for negative coolant flow, the peak temperature is at the dry air inlet. Counter flow cases show better performance for both cooling directions.

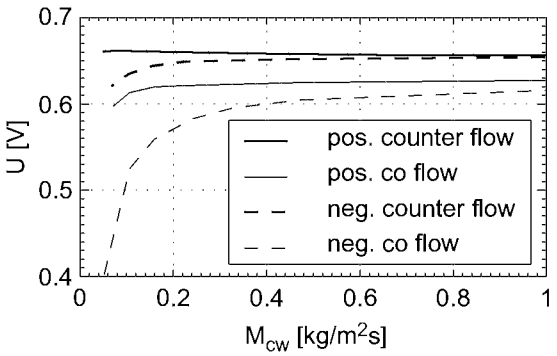

Fig. 1: The effect of coolant mass flow on the cell voltage at 5000 A/m² for different flow arrangements.

The same holds true throughout the whole current range as shown for the case of co flowing reactants at distinct fixed coolant flows in positive and negative direction in Figure 2 with a closer look on the underlying local current densities and coolant temperatures.

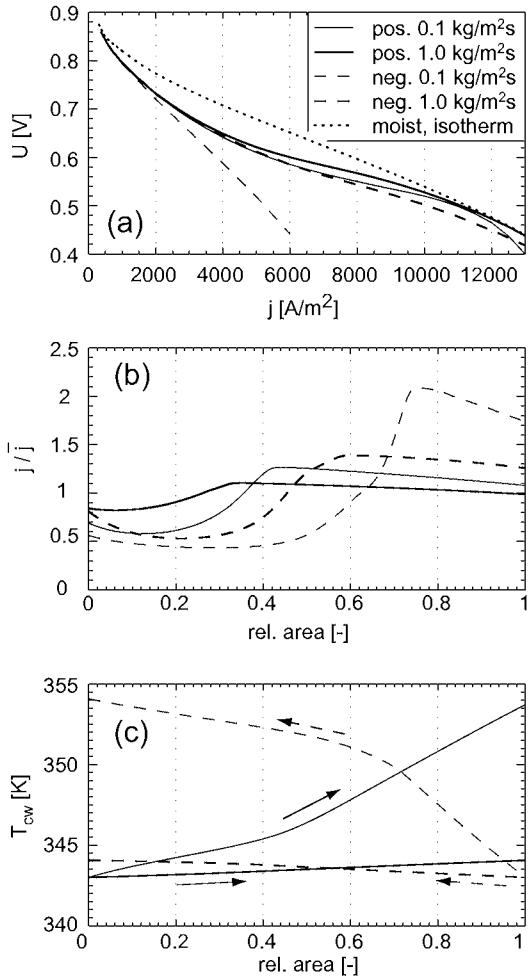

Fig. 2: Polarisation curves for co flowing reactants and different cooling flow arrangements (a), the normalized local current densities (b), and coolant temperatures (c) at 6000 A/m². The reactants flow from left to right.

The detrimental effect of increased temperature at the dry air inlet stems from an extended region of low current density there. In the opposite case the raised temperature at regions of fully saturated membrane downstream in the air path facilitates the reaction and transports giving a better performance even at lower coolant flow.

3 REFERENCE

[1] S.A. Freunberger, F.N. Büchi, submitted to the J. Electrochem. Soc. (2005).

HOMOGENISATION OF THE CURRENT DENSITY DISTRIBUTION IN POLYMER ELECTROLYTE FUEL CELLS WORKING WITH LOW AIR STOICHIOMETRIES

M. Santis, F.N. Büchi

Parasitic power consumption of the auxiliaries in a PEM fuel cell system can be reduced by operating the fuel cells at low air stoichiometries. However, this causes strong inhomogeneities in the current density distribution in the cell, lowering the performance. Experiments with a tailored electrode optimized for given operation conditions have shown promising results in the homogenisation of the current density distribution when operating the fuel cell at air stoichiometries as low as 1.2.

1 MOTIVATION

The optimization of a fuel cell system is a complex issue that calls for a compromise between power generation by the fuel cells and power consumption by the auxiliaries. A power consumption analysis of the auxiliaries shows that a substantial part of the power is consumed by the air compressor. One possibility to enhance the system efficiency is therefore to reduce the air stoichiometry (λ_{air}) to trim down the power consumption of the compressor. However this affects the performance of the fuel cell. Investigations of the current density distribution in PEM fuel cells have shown a strong inhomogeneity in the electrical current generation when λ_{air} is strongly reduced [1]. This phenomenon has been addressed by means of the electrochemical components.

2 TAILORED CATHODE APPROACH

During the generation of electrical current H_2 and O_2 are consumed along the gas paths. In PEM fuel cells operated with low λ_{air}, the overvoltages at the end of the gas path increase considerably. This leads to inhomogeneities in the current density distribution and as a result, local accelerated degradation phenomena could occur since some parts of the cell are electrochemically stressed more than others [2]. In order to homogenise the current density distribution along the air path at low λ_{air}, in a first approach a tailored cathode with an inhomogeneous distribution catalyst distribution loading has been developed.

3 EXPERIMENTAL

For the measurement of the local current density, the semi-segmented plate principle was used [1]. The segments location along the gas path and the profile of the Pt loading of the tailored cathode are shown in Fig. 1. The Pt loadings gradient along the air path are A: 0.3, B: 0.6, C: 1.2 mg/cm^2. The tailored cathode is realized by a puzzle principle using Elat-A7-Type E-Tek gasdiffusion electrodes. The average Pt loading of the tailored cathode was 0.6 mg/cm^2. The anode had a homogenous Pt loading of also 0.6 mg/cm^2. For the membrane, Nafion® 112 was used.

4 RESULTS

At high λ_{air} (2.0), cells with a conventional homogeneous cathode, show an almost homogeneous current density distribution along the air path (see Fig. 1). At λ_{air}= 1.2 and constant current operation conditions, the effects caused by O_2 depletion lead to an inhomogeneous distribution of electrical current production: less current is produced near the air outlet while a higher fraction is generated near the inlet. The tailored cathode approach is based on the following strategy: to compensate for the diminished O_2 concentration at the end of the air path a higher Pt loading was used promoting the current generation; at the beginning of the air path, being rich in O_2, the Pt loading was decreased lowering the current generation towards average along the air path (see Fig. 1).

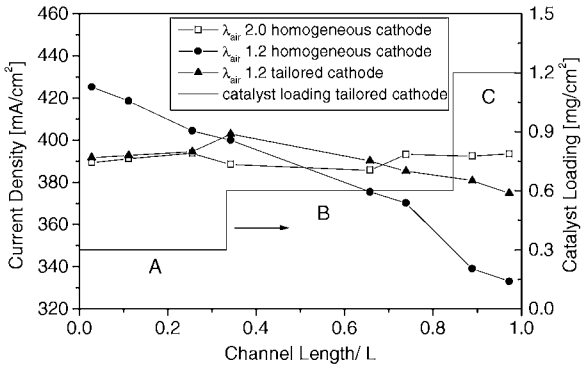

Fig. 1: Current density distribution as a function of the channel length. λ_{air}= 2.0 and 1.2 for the homogeneous cathode and 1.2 for the tailored cathode. λ_{H2}=2.0, T_{cell}= 70°C, air and H_2 dew point= 70°C, air and H_2 pressure= 2.0 bara. Constant Current mode with avg. current density 400 mA/cm^2. A, B and C see text.

These results show the possibility to homogenise the current density distribution in PEM fuel cells working with low λ_{air} by means of the electrochemical components, relieving the auxiliaries and therefore allowing for an enhanced overall system performance.

5 REFERENCES

[1] F.N. Büchi, A.B. Geiger, R.P.C. Neto, PSI Scientific Report 2001, **V**, 91 (2002).

[2] A.A. Kulikovsky, H. Scharmann, K. Wippermann, Electrochem. Comm. **6**, 75-82 (2004).

TOWARDS IN-PLANE INVESTIGATION OF LIQUID ACCUMULATION IN POLYMER ELECTROLYTE FUEL CELLS BY HIGH RESOLUTION NEUTRON IMAGING

D. Kramer, J. Zhang (Nissan), Y. Ono (Nissan), E. Lehmann, A. Wokaun, K. Shinohara (Nissan), G.G. Scherer

A high resolution neutron imaging detector was employed to the neutron radiography station NEUTRA in order to evaluate the possibility of liquid detection in the thickness-direction of hydrogen-fueled polymer electrolyte fuel cells. The separation of accumulations inside anode and cathode compartment could be achieved, and influences of method and sample that deteriorate the image quality, and therefore limit the effective spatial resolution, could be identified.

1 INTRODUCTION

Perpendicular penetration of operating polymer electrolyte fuel cells (PEFC) and direct methanol fuel cells (DMFC) by thermal neutrons allows the spatially resolved, non-invasive detection of liquid water inside the cell [1]. But the localization of liquid along the beam direction—whether it is inside the membrane, the anodic or the cathodic compartment—cannot be derived from those experiments. Therefore, the detection of liquid by passing the neutron beam through a cell which is rotated by 90°, is highly desirable to provide supplementary information [2]. This implies an improvement in spatial resolution by at least one order of magnitude, because typical dimensions in the thickness direction are in the order of micrometers rather than millimeters, which are common for in-plane structures, such as flow field channels.

2 EXPERIMENTAL

Single cells with an active area of 25 cm^2 were investigated to evaluate the possible detection of liquid in the thickness direction via a high resolution detector, which is capable of scanning neutron sensitive imaging plates with a spatial resolution of 10 µm. Images were obtained under three different operating conditions: (dry) the cell was purged with dry nitrogen on both sides, (OCV) the cell was supplied with pre-humidified gases (H_2 and air) under load-free operation, and (wet) the cell was operated at 800 mA/cm^2.

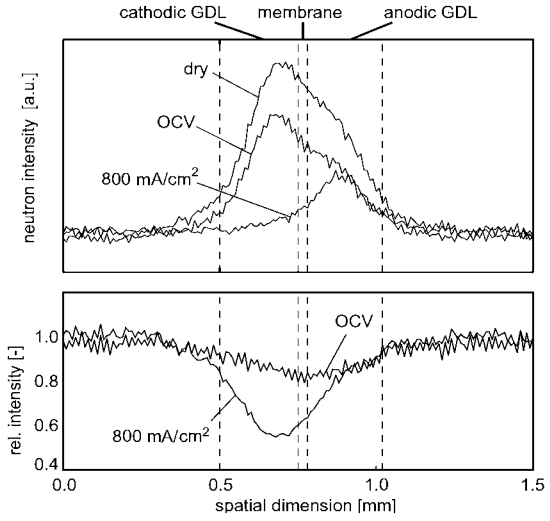

Fig. 1: Neutron intensities over the thickness of the MEA for different operating conditions.

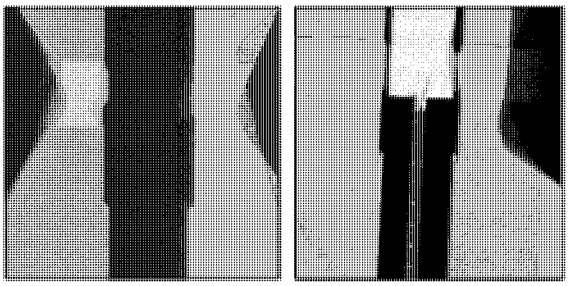

Fig. 2: Deteriorative influence of the gasket onto image quality.

3 RESULTS

The profiles of neutron intensity over the thickness of the MEA are shown in Figure 1. The highest intensity is obtained while feeding the cell with dry nitrogen. The asymmetric profile is caused by an additional insulator sheet ensuring electrical insulation between the flow field plates outside the MEA. The intensity is reduced by supplying humidified gases, whereas the reduction is strongest in the centre of the MEA—indicating that the intensity loss is due to membrane hydration. If current is generated, the intensity is asymmetrically reduced at the cathode compartment, indicating that product water is accumulating there, while no liquid is formed in the anodic compartment.

The broadened profiles indicate that the inherent spatial resolution is well above the detector limit. This is partially due to the deteriorative impact of the used sealing material as becomes evident from the images shown in Figure 2.

4 ACKNOWLEDGEMENT

Financial support by the Swiss Federal Office of Energy (BFE) is gratefully acknowledged.

5 REFERENCES

[1] D. Kramer, J. Zhang, R. Shimoi, E. Lehmann, A. Wokaun, K. Shinohara, G.G. Scherer, Electrochimica Acta, accepted.

[2] R.J. Bellows, M.Y. Lin, M. Arif, A.K. Thompson, D. Jacobson, J. Electrochem. Soc. **146**, 1099 (1999).

FAST LOCALLY RESOLVED ELECTROCHEMICAL IMPEDANCE SPECTROSCOPY IN POLYMER ELECTROLYTE FUEL CELLS

I.A. Schneider, H. Kuhn, A. Wokaun, G.G. Scherer

A system for performing locally resolved electrochemical impedance spectroscopy (EIS) in a segmented polymer electrolyte fuel cell (PEFC) has been developed. Due to our unique parallel approach, the measurement duration for obtaining a locally resolved impedance spectrum is virtually independent of the number of segments used. The current distribution and the corresponding locally resolved impedance spectrum for a PEFC segmented along a serpentine cathode flow field was investigated. The results show large differences in local cell impedance. The impedance spectrum of the entire cell provides only limited insight into factors limiting cell performance.

1 INTRODUCTION

When measuring over the entire active area of a PEFC, only average properties of the current density and the impedance of the cell can be determined. Thus, it is neither possible to identify inhomogeneities in fuel cell performance nor to get information about the respective local limiting processes.

We have addressed this problem by using EIS in a segmented H_2/O_2-PEFC. By doing this, locally resolved EIS measurements are possible and limiting processes affecting the lateral current distribution can be identified.

2 SEGMENTED PEFC

Our segmented cell (area 29.2 cm^2) is similar to an ordinary filter-press type H_2/O_2-PEFC consisting of a MEA sandwiched between two 3-fold serpentine flow field plates, which are clamped together by outer stainless steel plates. The only exception is the cathode flow field and its gold plated current collector (Figure 1). Both are divided into 9 electrically isolated segments of equal size.

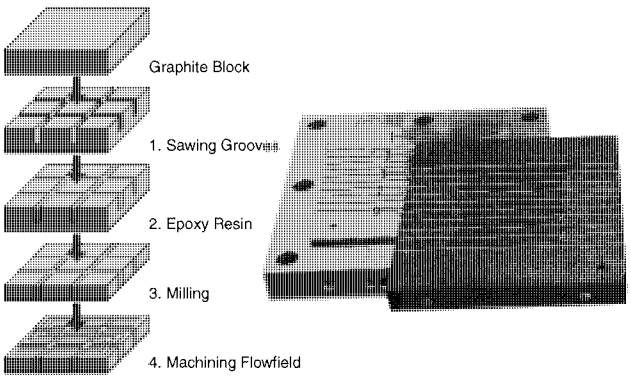

Fig. 1: Segmented cathode flow field/current collector and manufacturing steps.

3 SYSTEM FOR FAST PARALLEL EIS IN PEFCS

The system for performing locally resolved electrochemical impedance spectroscopy in a segmented PEFC has been developed in our laboratory (Figure 2) [1]. The setup is able to handle cell currents of up to 60 A and modulation frequencies up to 10 kHz.

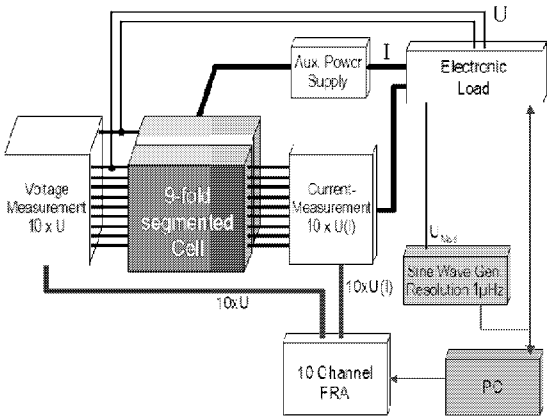

Fig. 2: System for performing fast locally resolved EIS in PEFCs.

The dc and ac current is controlled by an electronic load. The modulation amplitude and frequency is determined by a programmable sine wave generator. The segment currents are measured by using very low impedance and wide bandwidth closed loop hall sensors mounted directly at the cell. The segment currents are summed and fed back to the load. The segment voltages are measured individually by using wide bandwidth differential amplifiers, the large dc part of the signals is estimated and suppressed by using digital to analog converters. The remaining small residue signal is amplified.

The impedance measurement is carried out for all segments in parallel. For this, a multichannel frequency response analyzer was built up at our laboratory. The voltage and current signals are fed to high performance data acquisition channels and digitized in parallel. The frequency response analysis is performed with the digital signals, using a fast discrete fourier transform (DFT) algorithm. For a given frequency the computed values are displayed. The current distribution and the individual spectra are plotted in real time using the Nyquist- and Bode representation. Furthermore, the ac and dc voltages and currents are displayed.

Due to this unique parallel approach the measurement period for obtaining a locally resolved impedance spectrum is virtually independent of the number of segments used in a segmented PEFC.

4 EXPERIMENTAL

Membrane electrode assemblies were prepared from Nafion 115 membranes and carbon paper based electrodes with a platinum loading of 0.6 mg/cm^2. PTFE gaskets, 200 µm thick, were used to seal the cell. The cell was operated in galvanostatic mode on pure H_2 and O_2 at 70 °C and ambient pressure, using a dc current of 14.6 A. Both gases were fed in co-flow mode (r.h. 50%, stoich. = 1.5).

The amplitude of the sinusoidal modulation current was chosen such that the amplitude of the modulation voltages did not exceed a value of 10 mV. The modulation frequency was varied in a range from 10kHz to 0.0158 Hz.

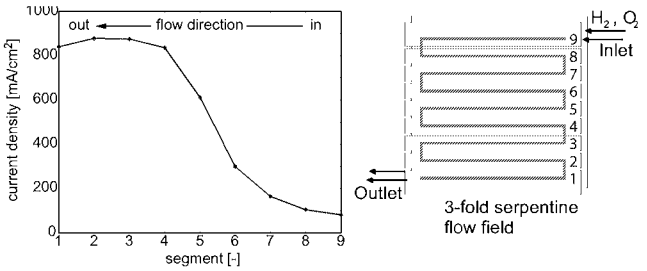

Fig. 3: Current density distribution in co-flow mode of the reactant gases (r.h. 50%).

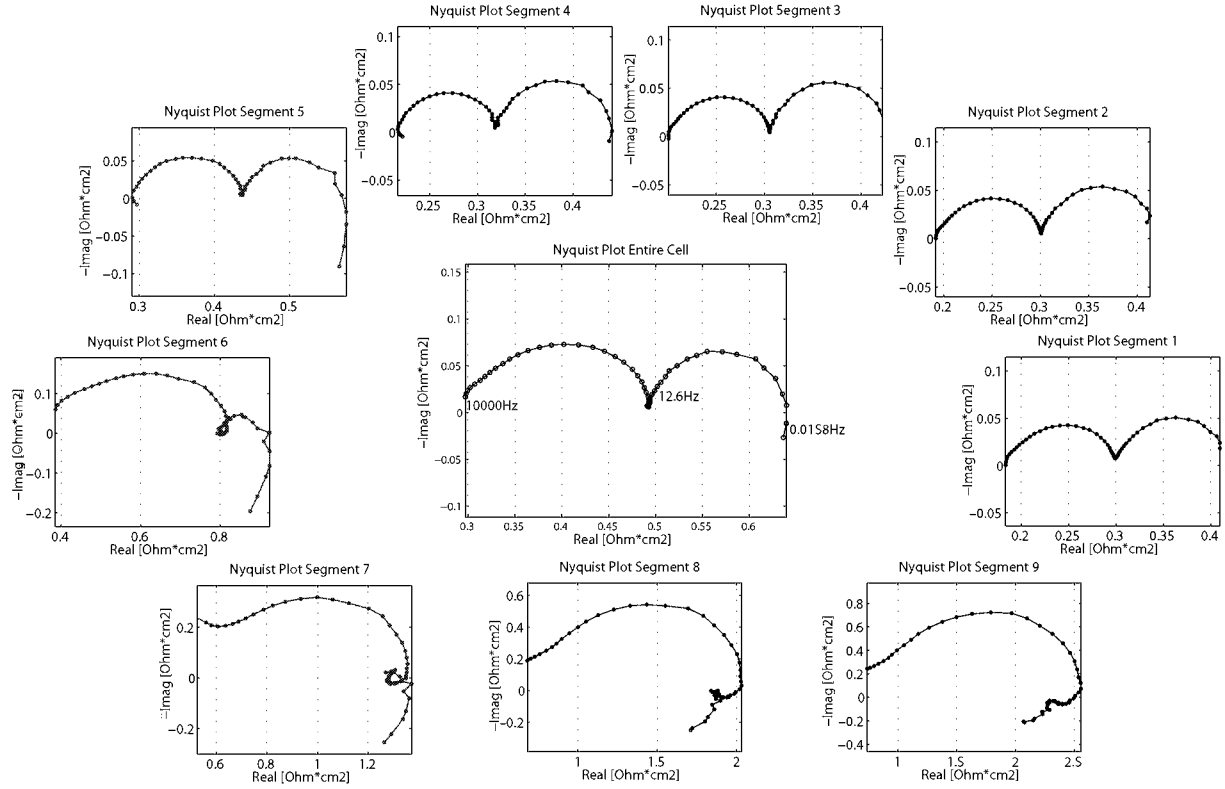

Fig. 4: Impedance spectra of segments 1-9 and calculated impedance spectrum of the entire cell.

5 RESULTS AND DISCUSSION

The benefit of an increasing relative humidity due to the formation of product water along the gas channels is clearly demonstrated. As the humidity increases along the channel from segment 9 to segment 1, in principle, the current density increases in the same direction (Figure 3).

The shape of the local impedance spectrum (Figure 4) changes from segment 9 to segment 1 along the channel, and as the shape of the spectrum changes, so do the processes limiting cell performance along the channel. Theses processes are discussed in [2]. The results show large differences in local cell impedance, whereas the spectrum of the entire cell shows only average values of the local cell impedances. The spectrum of the entire cell can be calculated from the individual spectra, since the segmented PEFC, in principle, is a parallel circuit of individual sub-cells.

The calculated integral spectrum of the cell (Figure 4) is similar in shape to the impedance spectra of segments 1-4, although different, but it has nothing in common with the spectra of segments 6-9.

The results show that the impedance spectrum of the entire cell provides only limited insight into factors limiting cell performance. One has to be careful when performing bulk EIS measurements in PEFCs. Bulk impedance measurements in PEFCs are only reasonable, if the cell is being operated in a state, in which local conditions are invariant within the cell [3].

6 REFERENCES

[1] I.A. Schneider et al., to be submitted (2005).

[2] I.A. Schneider et al., PSI Scientific Report 2004, **V**, 104 (2005).

[3] A.R. Kucernak et al., *Electrochem. and Solid-State Letters.*, **6**, A63-A66 (2003).

IMPACT OF GAS FLOW DIRECTION ON LOCAL PERFORMANCE AND LOCALLY LIMITING PROCESSES IN A PEFC STUDIED BY LOCALLY RESOLVED EIS

I.A. Schneider, A. Wokaun, G.G. Scherer

The current density distribution and the corresponding locally resolved impedance spectra for a H_2/O_2-PEFC segmented along a serpentine cathode flow field operated in co- and counter flow mode are presented and discussed. The benefit of an increasing humidity due to the formation of product water is demonstrated. The locally resolved impedance spectra show that the considerably lower performance in co-flow is due to drying and loss of active area.

1 INTRODUCTION

When operating a polymer electrolyte fuel cell (PEFC) under low humidity conditions the influence of the gas flow direction on cell performance becomes important. Differences in performance in co- and counter-flow mode are only due to variations in the local operating conditions. Therefore, locally resolved EIS measurements are a highly valuable *in situ* diagnostic tool to clarify the reasons for these differences.

2 EXPERIMENTAL

The experimental conditions are described in [1], with the exception that the gases are fed in co- and counter flow mode and oxygen is not humidified.

3 RESULTS AND DISCUSSION

When switching the reactant feed from counter- to co-flow the overall cell voltage strongly decreases from 651 mV to 482 mV (@ I_{Cell} = 14.6 A). The differences in performance are reflected in variations in the current density distribution and the respective locally resolved impedance spectrum. In co-flow mode the current density increases with increasing humidity (Figure 1a), whereas in counter-flow mode the current density shows a maximum with a strong decreasing value at the O_2 inlet (Figure 1d).

In co-flow mode the shape of the local impedance spectrum changes dramatically along the channel (Figure 1b), i.e. the processes limiting cell performance change along the channel. According to our model [2] there are two kinetic regimes in the cell. At high current densities and high humidity (seg. 1-3) the ORR kinetics and the diffusion at the anode are rate limiting (Figure 1c). At low current densities and low humidity (seg. 6-9) the diffusion is less or not important, since the capacitive arc in the lower frequency range disappears and the inductive behaviour of the cathode [2] becomes dominating (Figure 1b). Here the ORR and, due to the formation of a third higher frequency arc, evenmore the HOR are limiting. The ohmic and especially the charge transfer resistance increase dramatically along the channel length with decreasing humidity due to drying of the membrane and the catalyst layers (Figure 1b).

A higher frequency third arc is also seen in the spectrum of seg.1 (hydrogen inlet) in counter-flow mode (Figure 1f). Due to diffusion of water from the cathode to the anode this third arc disappears. Seg. 2, 3 and 4 (Figure 1f) show only one higher frequency cathodic arc. The charge transfer and ohmic resistance decrease with increasing current density. Segment 4 has the lowest charge transfer and ohmic resistance at all. The strong performance loss at the oxygen inlet (seg. 9) can be attributed to drying of the cathode catalyst layer and the membrane (Figure 1e). Starting at the oxygen inlet, due to the formation of water on the cathode side and transport of water from the humidified anode to the cathode the charge transfer and ohmic resistance rapidly decrease.

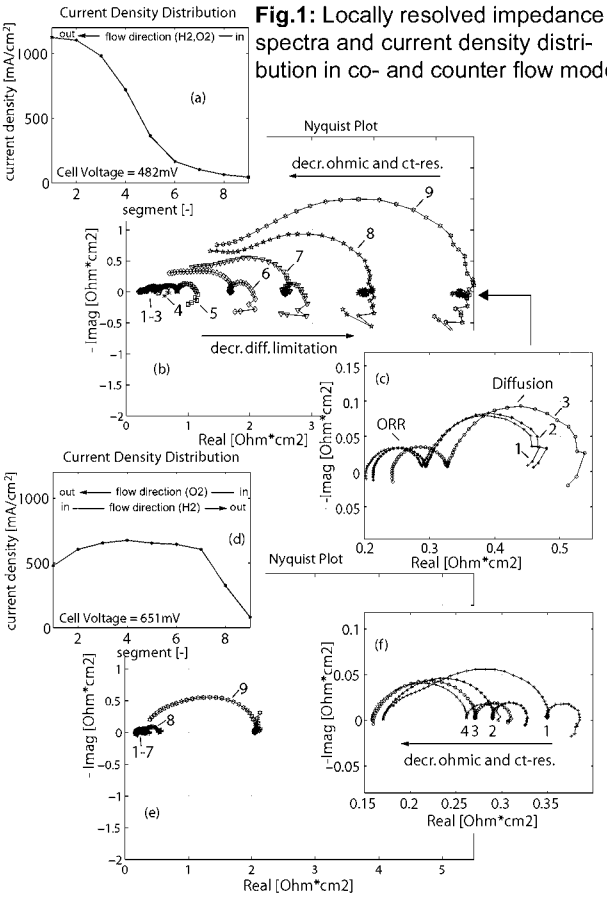

Fig.1: Locally resolved impedance spectra and current density distribution in co- and counter flow mode.

However, when comparing the locally resolved impedance spectra for co- and counter flow mode (Figure 1b,e) it becomes obvious that the performance loss in co-flow mode is due to drying and a substantial loss of active area, whereas in counter-flow mode most of the electrode area is well humidified.

4 REFERENCES

[1] I.A. Schneider et al., PSI Scientific Report 2004, **V,** 102-103 (2005).

[2] H. Kuhn et al., Electrochim. Acta, accepted (2004).

MASS TRANSPORT PHENOMENA IN POLYMER ELECTROLYTE FUEL CELLS

H. Kuhn, B. Andreaus, G.G. Scherer, A. Wokaun

A sufficient water content in the solid polymer electrolyte is crucial for the proton conductivity and, therefore, important for the performance of polymer electrolyte fuel cells. During operation at high current densities the solid polymer electrolyte shows a lower water content at the anode side and, hence, a detrimental effect on electrode and membrane behaviour. To avoid this effect, the fuel can be humidified or the back-diffusion of the product water from the cathode to the anode side can be enhanced. One possibility of enhanced water back diffusion can be achieved by applying an excess gas pressure at the cathode versus the anode side.

1 INTRODUCTION

It has been demonstrated that under high current density operation the water transport from anode to cathode by electro-osmosis can not be balanced by back transport of water from cathode to anode. The consequence is a lower water content in the ionomer of the anode and the anode-adjacent electrolyte layer [1] and, therefore, an increase in local resistivity. Hence, a reasonable water management is needed to ensure optimal hydration of the ionomer to avoid performance losses. [2,3].

2 EXPERIMENTAL

The experimental setup can be found elsewhere [4]. An excess pressure of 0 to 140 mbar was applied between cathode versus anode. Hydrogen was humidified at a dew point of 80°C, whereas oxygen was fed dry. The cell was operated at a constant current density of j = 500 mA/cm^2.

3 RESULTS & DISCUSSION

Water as the reaction product is created at the cathode. Depending on the humidification conditions at anode and cathode, part of this water is transported back to the anode side. At high current densities this back-diffusion is not sufficient anymore to compensate the electro-osmotic water drag. To enhance this back-diffusion, we applied a pressure difference between the cathode and the anode. The impact of this pressure difference on the fuel cell performance was studied by electrochemical impedance spectroscopy (EIS).

At the given current density, a pressure difference of up to 140 mbar between cathode and anode caused an increase in cell potential of 12% from 471 mV to 535 mV. EIS reveals two major effects, which cause this enhancement of cell performance. First, we observe a decrease of the ohmic resistance R_M by 21%, from 12.4 mΩ to 9.8 mΩ. As a consequence, the slope of the polarisation curve is only little affected, as can be seen in the inset of Figure 1. Second, we observe a clear decrease of the diffusion impedance, and this has the pronounced influence on the cell performance. The diffusion impedance Z_N is reduced by 87%, from 13.2 mΩ to 1.7 mΩ. The decrease is expressed in the polarisation curve at high current densities. The slope of the current–voltage curve at 50 mbar and 140 mbar pressure difference (dashed and solid line) are almost the same, but the behaviour

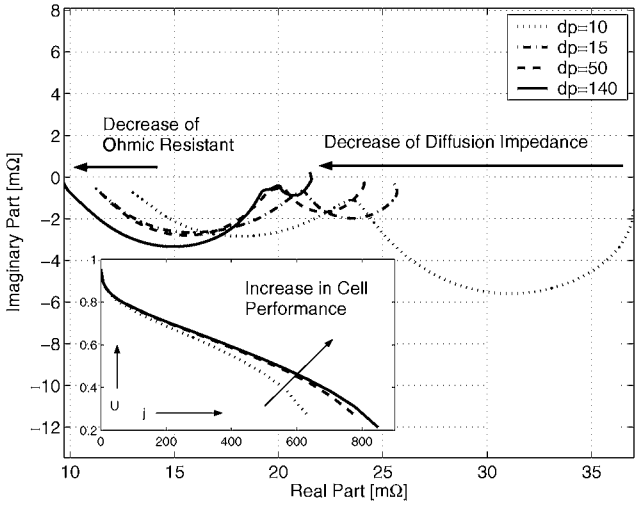

Fig. 1: Selected impedance measurements at various pressure differences between cathode and anode. The inset shows the polarisation curves at corresponding pressure differences.

at high current densities for the current-voltage curve and higher differential pressure (solid line) shows lower mass transport limitations.

Table 1: Mean values of different pressure intervals.

dp [mbar]	R_M [mΩ]	Z_N [mΩ]
0 - 10	~12.41	~13.2
15 - 50	~10.97	~3.9
100 - 140	~9.77	~1.7

These observations may be explained on the basis that due to the pressure difference the back-diffusion of the product water from the cathode to the anode side is enforced. Hence, the resulting higher water content at the anode side is better balanced. These findings will have consequences for cells of technical relevance, including the aspects of system design for these cells.

4 REFERENCES

[1] F.N. Büchi, G.G. Scherer; J. Electroanal. Chem. **404**, 37-43 (1996).

[2] B. Andreaus, A.J. McEvoy, G.G. Scherer, Electrochim. Acta **47**, 2223-2229 (2002).

[3] B. Andreaus, G.G. Scherer, Solid State Ionics **168**, 311-320 (2004).

[4] H. Kuhn, B. Andreaus, G.G. Scherer, A. Wokaun, PSI Scientific Report 2003, **V**, 107 (2004).

MODELING THE IMPEDANCE RESPONSE OF THE HYDROGEN OXIDATION REACTION IN POLYMER ELECTROLYTE FUEL CELLS

H. Kuhn, B. Andreaus, G.G. Scherer, A. Wokaun

Utilising a pseudo reference electrode in fuel cells allows for the separation of anodic and cathodic contributions to the entire cell impedance, ensuring no significant impact on the current distribution. Modelling the impedance responses by using equivalent circuits inhibits the investigation of kinetic parameters of the basic electrochemical reaction taking place at the electrode-electrolyte interface. We used a state-space model approach to calculate the impedance response based on a kinetic model of the basic reaction pathway for the hydrogen oxidation reaction (HOR). Hence, it is possible to obtain kinetic parameters for the specific reaction of interest.

1 INTRODUCTION

Compared to other *in situ* methods, EIS usually yields a better discrimination of the different fundamental processes occurring in PEFCs, such as the charge transfer kinetics or double layer charging. Usually, the EIS measurements are carried out across the whole cell, and the anode contributions of the hydrogen oxidation reaction (HOR) to the total cell impedance are neglected, the measured impedance being completely attributed to the oxygen reduction reaction (ORR) and to the electrolyte. The utilisation of a pseudo reference electrode enables the investigation of single electrode-electrolyte interfaces in a PEFC [1]. To extract kinetic parameters for these reactions it is necessary to derive a model which is based on the specific reaction pathway. We concentrate on the calculation of the theoretical impedance response of the HOR.

2 MODEL & SIMULATION

We used a state-space model approach to rationalise the theoretical impedance. An excellent description of this general method to analyse the transfer function of a linearised system was given by Gabrielli and Tribollet [2]. Based on the theoretically derived equations for the electrochemical reaction of hydrogen, the model yields the kinetic parameters for the HOR.

Considering the Tafel-Volmer path:

$$H_2 + 2M \rightarrow 2(M - H_{ad}) \quad (1)$$

$$(M - H_{ad}) \rightarrow H^+ + e^- + M \quad (2)$$

we may write down the respective state equation expressing the mass balance on the catalyst surface:

$$\rho\dot{\theta} = k_{ad} P_H (1-\theta)^2 - k_{des}\theta^2 - 2k_{ec}\theta \sinh\left(\frac{\eta_A}{b_H}\right) \quad (3)$$

as well as the observation equation:

$$j = 2k_{ec}\theta \sinh\left(\frac{\eta_A}{b_H}\right), \quad \text{with } b_H = \frac{RT}{F} \quad (4)$$

k_{ad} and k_{des} refers to the adsorption and desorption rate of hydrogen, θ denotes the hydrogen coverage and k_{ec} refers to the faradaic reaction rate when electrons are exchanged between adsorbed hydrogen and electrode. η_A describes the anode overpotential.

Following the state-space model we derive the faradaic impedance as:

$$\frac{1}{Z_F} = C(j\omega 1 - A)^{-1} B + D \quad (5)$$

with $A = \frac{\partial\dot{\theta}}{\partial\theta}$, $B = \frac{\partial\dot{\theta}}{\partial\eta_A}$, $C = \frac{\partial j}{\partial\theta}$, $D = \frac{\partial j}{\partial\eta_A}$.

The faradaic impedance, Z_F, considers charge transfer reactions at the interface. To explain the experimental results we have to extend this impedance with a Nernst's diffusion impedance, Z_N, a double layer capacity, Z_{CPE}, and the electrolyte resistance, R_{el}. Hence we obtain the following overall anode impedance:

$$Z_{Anode} = R_{el} + \left(\frac{1}{Z_{CPE}} + \frac{1}{Z_F + Z_N}\right)^{-1}.$$

A comparison between experimental and simulated data is shown in Figure 1. The model represents the measured data well. Reaction rates are now accessible and can be determined under different operating conditions [3].

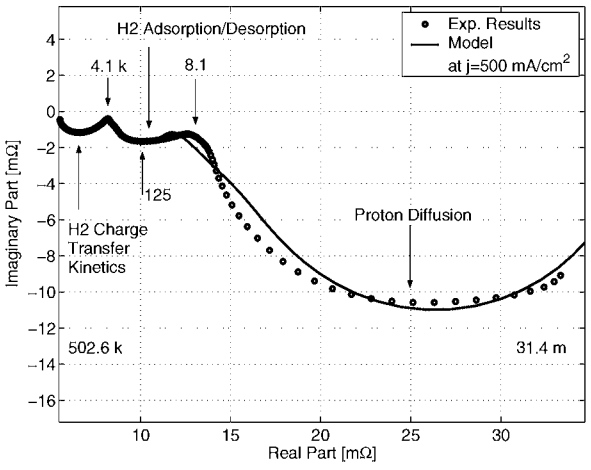

Fig. 1: Comparison between experimental and simulated results at current density of j = 500 mA/cm^2 for the HOR. Units of selected frequencies are *rads*$^{-1}$.

3 REFERENCES

[1] H. Kuhn, B. Andreaus, G.G. Scherer, A. Wokaun, PSI Scientific Report 2003, **V**, 107 (2004).

[2] C. Gabrielli, B. Tribollet, J. Electrochem. Soc. **141**, 1147-1157 (1994).

[3] H. Kuhn, B. Andreaus, A. Wokaun, G.G. Scherer, Electrochim. Acta, accepted (2004).

ROUGHNESS AND MORPHOLOGY CHANGES ON PLATINUM ELECTRODES

A. Reiner, B. Steiger, G.G. Scherer, A. Wokaun

A correlation between surface roughness and the electrochemically active surface fraction of Pt electrodes concerning the under potential deposition of hydrogen (H_{upd}) was found by cyclic voltammetry (CV) in 0.5 M H_2SO_4. Furthermore, a dramatic morphology change was observed due to intensive cycling.

1 INTRODUCTION

Platinum as a precious metal is still the most important catalyst material for polymer electrolyte fuel cells. In order to reduce the catalyst loading without performance penalty, the efficiency of the catalyst has to be increased. Information about the H_{upd} on Pt could help to identify limiting factors. However, useful measurements require stable electrode surface properties [1]. Knowledge about methods for increasing the catalyst surface could also help to reduce the loading.

2 EXPERIMENTAL

CV was carried out at 21° C with Pt wire counter and Hg/Hg_2SO_4 reference electrodes in 0.5 M H_2SO_4 saturated with purified Ar. The Pt disc electrodes were fabricated by heat sealing a polycrystalline Pt wire (250 µm) in a glass capillary followed by polishing successively with 600 grit SiC paper, 5, 0.3 and 0.05 µm Al_2O_3.

3 RESULTS

Pt electrodes in 0.5 M H_2SO_4 show deposition of a monolayer of atomic hydrogen before the onset of H_2 evolution. Due to the 1:1 relationship between a Pt-surface atom and an adsorbed H-atom, it was possible to calculate from the measured charge the electrochemically active Pt surface of the different electrodes. By cycling a polished electrode between the onset potentials for H_2 and O_2 evolution (about -0.64 to 0.80 V) at a scan rate of 200 V/s until steady state, the surface roughness changes drastically (Figure 1B).

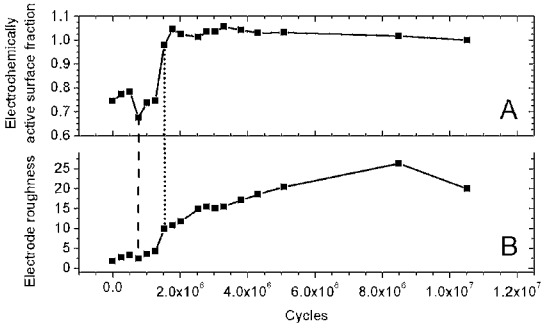

Fig. 1: Active surface fraction (A) and roughness (B).

After each roughening step, also the electrochemically active surface fraction concerning the H_{upd} process was recorded by scanning for 5 min in the limited voltage range between -0.64 and 0.0 V (Figure 1A). Until a surface roughness of about a factor of 12 is reached, it appears that there is a direct correlation to the electrochemically active surface fraction. Furthermore, it is apparent that after reaching a roughness value of about 12 only minor variations are observed by cycling further. In Figure 2 optical microscope pictures show how the intensive potential cycling affects the surface morphology of a freshly polished Pt disc electrode (Figure 2: A). The pictures of the electrode surfaces look like as if they were composed of several small crystalline islands. Presumably, these self-contained regions contact each other by grain boundaries. Proceeding from B to C (see Figure 2) the surface roughness increases and it appears that the surfaces of the islands are covered by increasing holes. This roughening process may be explained by a suggested mechanism for surface-oxide growth on Pt electrodes in H_2SO_4 [2]. The penetration of oxygen ions into the topmost layer is one of the steps of this mechanism. During the reduction process, the oxide ions are expelled from the metal lattice so that the roughening of the surface becomes understandable. Probably, the restructuring of the reduced Pt surface atoms is not ideal, i.e. in the outermost layer of the surface dislocations and holes remain. The extensive repetition of the activating cycle can then result in the surface roughening.

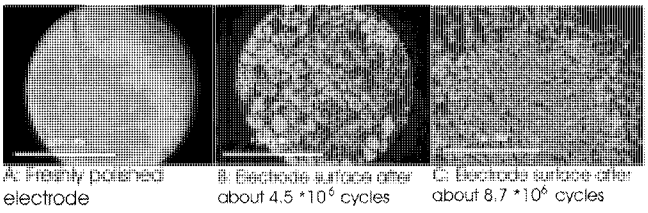

Fig. 2: Pt electrode surface variations.

Further increase of the number of activation cycles led to a significant change in the surface morphology accompanied by a dramatically increase of the electrode surface roughness. The surface became covered with needles (Figure 3). The uncovered surface after mechanical removal of the needles looked like the surfaces of B (see Figure 2). Although this new morphology has been reproduced several times, we are still trying to identify the factors, including the required number of activation cycles, that lead to this dramatic morphology change.

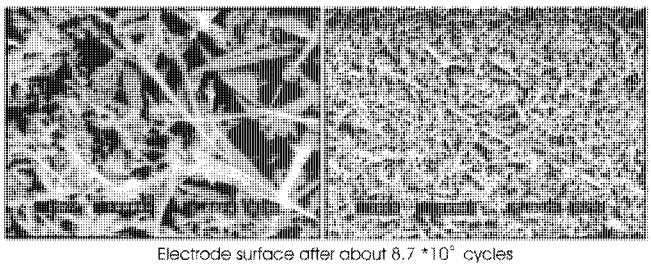

Fig. 3: SEM pictures of the novel Pt morphology.

4 REFERENCES

[1] A. Reiner, B. Steiger, G.G. Scherer, A. Wokaun, PSI Scientific Report 2003, **V**, 96 (2004).

[2] G. Jerkiewicz, et al., Electrochim. Acta **49**, 1451 (2004).

XPS AND XRD CHARACTERIZATION OF ELECTROCHEMICALLY REDUCED METAL OXIDE POWDERS

B. Steiger, A. Foelske, N.K. Beck, R. Kötz, G.G. Scherer, A. Wokaun

The effect of cathodic polarization and potential cycling on the composition of $Bi_2Pt_{2-y}Ir_yO_7$ ($0 \le y \le 2$) powders mechanically attached to the surface of graphite electrodes in 0.5 M H_2SO_4 has been studied by X-ray photoelectron spectroscopy (XPS). Furthermore, the products of controlled-potential electroreduction of PtO_2 and $Bi_2Pt_2O_7$ powders have been analyzed by X-ray diffraction (XRD). The reduction of Pt(IV) to Pt(0), Bi(III) to Bi(0) and Ir(IV) to Ir(0) was observed. The latter proceeded exceedingly slow.

1 INTRODUCTION

In recent reports it has been demonstrated that cycling of $Bi_2Pt_{2-y}Ir_yO_7$ electrodes between -0.6 and 0.6 V vs. Hg/Hg_2SO_4 is required for observing oxygen reduction activity [1,2]. It was recognized that this "activation" is initiated by a reduction process that produces a Pt containing material at potentials located near the negative limit of the cycling range. Herein, we report on the effect of this reduction process on the composition of $Bi_2Pt_{2-y}Ir_yO_7$ powders by means of cyclic voltammetry (CV), XPS, and XRD.

2 EXPERIMENTAL

The preparation of $Bi_2Pt_{2-y}Ir_yO_7$ and the equipment for conducting CV is described elsewhere [1]. Graphite pieces (∅ 6 mm) were punched out of a Sigraflex® graphite foil (SGL, 2 mm), pressed at 1 ton for 10 min and roughened on 400 grit SiC paper (Buehler). Then the oxide powder was spread on 1000 grit SiC paper and attached to the graphite piece by polishing. Preparative, controlled-potential reduction of 10 mg oxide powder, pressed between porous gold foils, was carried out in a cell with a gold sheet counter electrode using an EG&G PAR M173 potentiostat combined with a M179 coulometer. Potentials are given against Hg/Hg_2SO_4. The determination of the oxidation states of all the elements in the powders before and after electrolysis (glove box and sample transport under N_2) was carried out using a VG ESCALAB 220i XL (Thermo VG Scientific) spectrometer (Al Kα, λ = 1486.6 eV, 10 kV, 20 mA). XRD was carried out using a Siemens D500 X-ray diffractometer (Cu Kα).

3 RESULTS AND DISCUSSION

Cyclic voltammograms of a set of metal oxide powders on graphite (PtO_2, Bi_2O_3, IrO_2, and $Bi_2Pt_{2-y}Ir_yO_7$) are shown in Figure 1. The initial CV scan of PtO_2 shows an irreversible cathodic peak at *ca.* -0.5 V and the subsequent CVs show the typical shape known for Pt electrodes (Figure 1A). The area under the initial cathodic peak corresponds to 428 mC charge which is much larger than the 0.91 mC charge calculated from the underpotential adsorption/desorption of a monolayer of hydrogen. This indicates that the reduction process involves the bulk of the material (*vide infra*). The CV of Bi_2O_3 powder on graphite shown in Figure 1B exhibits similar features like the CV recorded with a cavity microelectrode where Bi_2O_3 powder was reduced to metallic Bi during the cathodic scan [3]. The

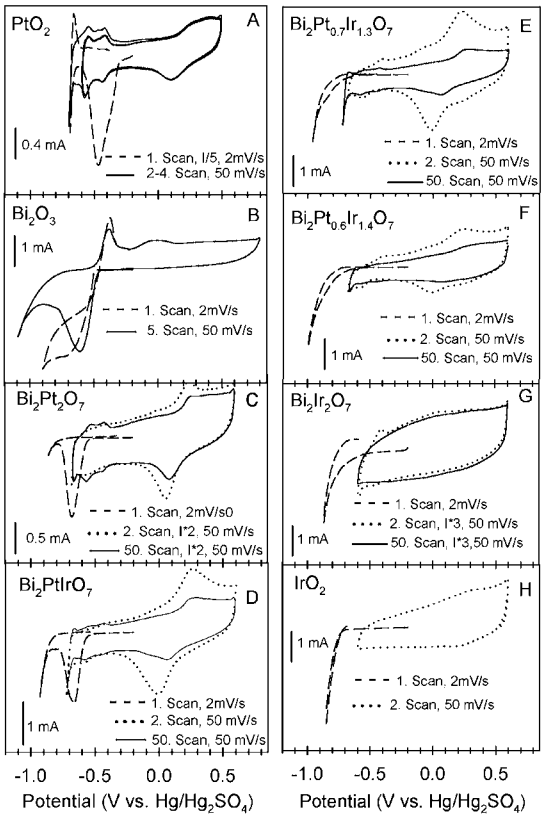

Fig. 1: CVs of metal oxide powders on graphite in Ar-saturated 0.5 M H_2SO_4 at the indicated scan rates and current scales.

first CV of $Bi_2Pt_2O_7$ shows an irreversible cathodic peak at *ca.* -0.68 V (Figure 1C). The dotted curve in Figure 1C was recorded immediately after completion of the first CV scan and its shape closely resembles CVs recorded with Pt electrodes immersed into 0.1 M $HClO_4$ containing dissolved Bi(III) species [4]. The characteristics of such Pt electrodes is the suppression of the underpotential adsorption/desorption of hydrogen and the underpotential adsorption/desorption of Bi at potentials coinciding with potentials for Pt oxide formation/reduction. We detected by ICP-OES significant concentrations of dissolved Bi in 0.5 M H_2SO_4 used to record the dotted CV curve shown in Figure 1C. Cycling and electrolyte exchange resulted in CVs with features known for pure Pt electrodes (Figure 1C, 50. scan). Increasing substitution of Pt for Ir leads to CVs exhibiting a less pronounced or absent initial cathodic peak (Figure 1D-1H).

Figure 2 (top) shows high resolution XP-spectra recorded for as prepared Bi_2PtIrO_7. The binding energies of 61.4 and 64.4 eV are found for Ir $4f_{7/2}$ and Ir $4f_{5/2}$ photoelectron lines, respectively, which are characteristic for Ir(IV) (e.g. IrO_2 [5]). The position of the Pt 4f core levels (73.6 and 77.0 eV) are in good agreement with those published for Pt(IV) (e.g. PtO_2 [5]). The binding energies of 158.0 and 163.5 eV are found for Bi $4f_{7/2}$ and Bi $4f_{5/2}$ photoelectron peaks, respectively, which can be assigned to Bi(III) (e.g. Bi_2O_3 [5]). After electrolysis at -0.8 V for 30 min, followed by removing the electrode from the electrolyte at this potential, and subsequent transfer under N_2 atmosphere into the UHV, the XP-spectra recorded, show marked changes (Figure 2, middle). Most of the surface Bi(III) and essentially all surface Pt(IV) was reduced to Bi(0) and Pt(0), respectively, as evidenced by the binding energies characteristic for the 4f electrons of the corresponding metals [5]. However, only a small amount of Ir(IV) was reduced to Ir(0) (peak at 60 eV). The bottom part of Figure 2 depicts high resolution XP-spectra recorded for Bi_2PtIrO_7 after potential cycling between -0.6 and 0.6 V at 50 mV s^{-1} for 16 cycles, followed by removing the electrode from the electrolyte at -0.5 V. This potential cycling method is the typical "activation" procedure for $Bi_2Pt_{2-y}Ir_yO_7$ pellet electrodes used in electrocatalytic experiments [1,2]. Under these conditions no Ir(0) could be detected. In contrast, the Pt and the Bi XP-signals show both the oxidized and reduced species.

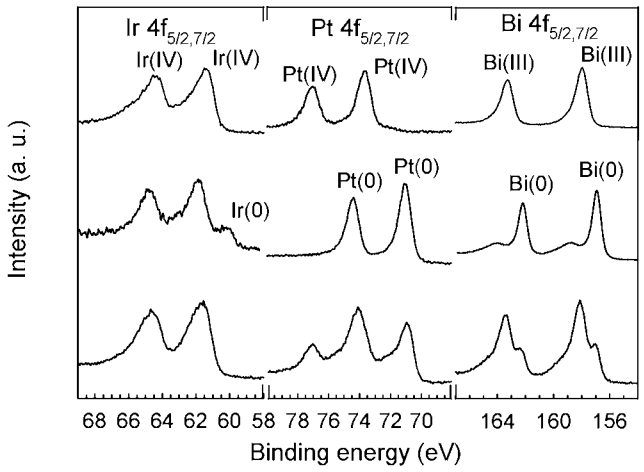

Fig. 2: High resolution XP-spectra of the Ir, Pt and Bi 4f electrons in Bi_2PtIrO_7 as prepared (top), after electrolysis at -0.8 V (middle) and after CV between -0.6 and 0.6 V (bottom).

Sputter depth profiling of the CV "activated" oxide powder with Ar^+ provides evidence that the presence of Pt(IV) is limited to the topmost layer. After 15 sec of ion etching all Pt(IV) has been removed from the surface and the Pt 4f signal shows metallic Pt(0) in the bulk material only. In contrast the presence of Bi(III) is not limited to the topmost layer. Bi(III) dominates the Bi 4f signal up to a sputter time of 800 sec, which corresponds to a depth of about 15 nm. These results can be explained by the fact that the negative limit of the potential cycling range (-0.6 V) is located at the foot of the cathodic CV peak shown in Figure 1D and therefore only a fraction of the total charge is passed during the cycling. That the reduction process involves the bulk of the metal oxide powders, is further confirmed by XRD analysis of the isolated product powder of a controlled-potential reduction of PtO_2 on a preparative scale (see Experimental). Figure 3 (top) shows the XRD pattern of commercial PtO_2. Diffraction peaks due to the presence of metallic Pt as impurity are also seen. The bottom part of Figure 3 shows that the XRD pattern for PtO_2 has been completely replaced by the XRD pattern typical for polycrystalline Pt metal after controlled-potential electroreduction. An analogous preparative electroreduction was carried out using $Bi_2Pt_2O_7$. No distinct XRD pattern was obtained, although coulometry showed exhaustive reduction and XPS was in agreement with the reduction of all surface Bi(III) and Pt(IV) to Bi(0) and Pt(0). Since air was not excluded for the XRD measurement, it is possible that a complex mixture of Pt and Bi materials is responsible for the observed XRD behavior.

Continuing investigations are directed towards the determination of the structure of the materials produced by the electroreduction of $Bi_2Pt_{2-y}Ir_yO_7$.

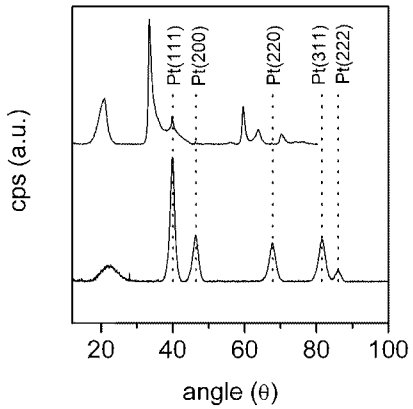

Fig. 3: XRD patterns of PtO_2 before (top) and after controlled-potential electroreduction (bottom).

4 ACKNOWLEDGEMENT

This work was supported by the Swiss Federal Office of Energy (BFE), Bern.

5 REFERENCES

[1] N. K. Beck, B. Steiger, G.G. Scherer, A. Wokaun, Proc. 2nd FDFC Conference, Belfort, France, Nov. 29–Dec. 2, ISBN 2914279-16-7, 177 (2004).

[2] N.K. Beck, B. Steiger, G.G. Scherer, A. Wokaun, PSI Scientific Report 2004, **V**, 110 (2005).

[3] V. Vivier et al., J. Electrochem. Soc. **147**, 4252 (2000).

[4] C.P. Wilde, M. Zhang, Langmuir **10**, 1600 (1994).

[5] C.D. Wagner et al, NIST Database 20, Web Version 3.4 (2003).

INFLUENCE OF ELECTROCHEMICAL PRE-TREATEMENT OF $Bi_2Pt_{2-y}Ir_yO_7$ PYROCHLORES ON OXYGEN REDUCTION ACTIVITY

N.K. Beck, B. Steiger, G.G. Scherer, A. Wokaun

$Bi_2Pt_{2-y}Ir_yO_7$ pyrochlores have shown both oxygen reduction activity and methanol tolerance. A pre-treatment by potential cycling, where reduction processes take place, is needed to obtain catalytic activity. A multiple potential step method has been applied to obtain current-potential curves for oxygen reduction.

1 INTRODUCTION

The oxygen reduction (ORR) activity of $Bi_2Pt_{2-y}Ir_yO_7$ pyrochlores increases as the platinum content increases in the structure. Methanol tolerance of these pyrochlores depends on the platinum content; the less platinum in the structure the better is the methanol tolerance [1]. We show that the catalyst has to be activated prior to ORR. New results have been obtained by using powder pellets and a method of multiple small potential steps.

2 EXPERIMENTAL

$Bi_2Pt_{2-y}Ir_yO_7$ (y= 1, 1.3, 1.4) were prepared by solid state synthesis [2] and pellets were prepared by cold pressing the powders followed by sintering in air. The pores of the pellets were filled with epoxy. The kinetics of the ORR of the oxides was studied using the rotating ring-disk electrode (RRDE) technique in O_2-saturated 0.5 M H_2SO_4. MeOH tolerance was measured in 0.5 M MeOH in Ar-saturated 0.5 M H_2SO_4 using equipment reported in [1].

3 RESULTS

Pyrochlores have to be activated prior to use at potentials near -0.6 V (Figure 1) [2,4]. The first cathodic scan of the fresh electrode does not show ORR activity but the anodic scan shows the development of the plateau. The *I-E* curve is stable after 4 cycles.

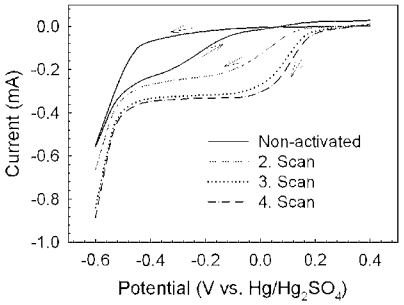

Fig. 1: The development of ORR activity of a fresh Bi_2PtIrO_7 powder pellet in O_2-saturated 0.5 M H_2SO_4 at 100 rpm. Scan rate = 5 mV/s. Cathodic scans are only shown for scans 2-4.

I-E curves for the ORR of $Bi_2Pt_{2-y}Ir_yO_7$ RDEs compared to a solid Pt RDE show that the electrocatalytic activity increases with Pt content in the oxide (Figure 2). H_2O_2 formation increases as the Pt content decreases. A method of multiple small potential steps [3] was applied to obtain *I-E* curves at the RDE, which allows reducing double layer charging current and eliminates adsorption current. For each potential step only one convection-diffusion-controlled ORR current value at the end of the step is recorded and the *I-E* curve is obtained from the collection of current points.

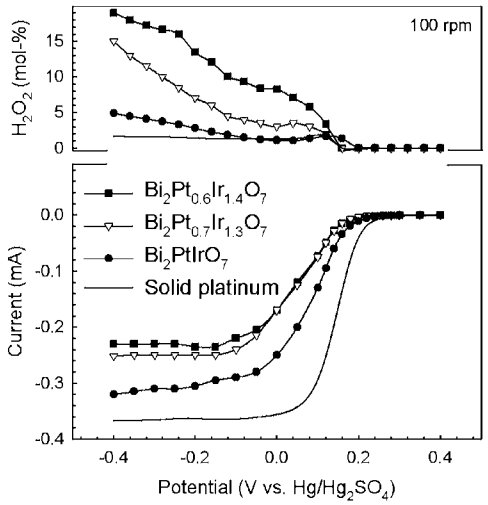

Fig. 2: O_2 reduction and H_2O_2 formation on $Bi_2Pt_{2-y}Ir_yO_7$ (y= 1, 1.3, 1.4) RDEs compared to a solid polycrystalline Pt RDE in O_2-saturated 0.5 M H_2SO_4. Scan rate = 5 mV/s.

Table 1 shows the MeOH oxidation current at 0.04 V of $Bi_2Pt_{2-y}Ir_yO_7$ RDEs at 100 rpm in comparison to Pt/Vulcan on a glassy carbon RDE. The lower the Pt content the better the MeOH tolerance.

Catalyst	$Bi_2Pt_{0.6}Ir_{1.4}O_7$	$Bi_2Pt_{0.7}Ir_{1.3}O_7$	Bi_2PtIrO_7	Pt/ Vulcan
I [mA]	0	5	40	170

Table 1: Methanol oxidation activity of $Bi_2Pt_{0.6}Ir_{1.4}O_7$, $Bi_2Pt_{0.7}Ir_{1.3}O_7$, and Bi_2PtIrO_7 compared to Pt/Vulcan XC-72 (ETEK,14 $\mu g_{Pt}/cm^2$, 20% Pt/C) at 0.04 V in 0.5 M MeOH in Ar-saturated 0.5 M H_2SO_4.

4 ACKNOWLEDGEMENTS

We are grateful to Dr. Claus Schüler for numerous helpful discussions. This work was supported by the Swiss Federal Office of Energy (BFE), Bern.

5 REFERENCES

[1] N. Lempola, B. Steiger, G.G. Scherer, A. Wokaun, PSI Scientific Report 2003, **V**, 84 (2004).

[2] N.K. Beck, B. Steiger, G.G. Scherer, A. Wokaun, Proc. 2nd FDFC Conference, Belfort, France, November 29 - December 2, ISBN 2914279-16-7, 177 (2004).

[3] R. Jiang, D. Chu, Electrochim. Acta **45**, 4025 (2000).

[4] B. Steiger, A. Foelske, N.K. Beck, R. Kötz, G.G. Scherer, A. Wokaun, PSI Scientific Report 2004, **V**, 108-109 (2005).

INVESTIGATIONS ON THE CONDUCTIVITY OF VARIOUS PROTON EXCHANGE MEMBRANES

L. Gubler, T. Finsterwald (ETH Zürich), G.G. Scherer

Polymer electrolyte fuel cells operating at reactant gas relative humidities below 100 % offer system efficiency advantages over fully humidified systems, because less energy is consumed in the preconditioning, i.e. humidification of the H_2 and O_2 / air. The proton conductivity of the polymer electrolyte membrane strongly depends on its water content and, consequently, the relative humidity of the reactant gases. In this study, the water uptake and conductivity of different types of membranes were characterized and compared to each other.

1 INTRODUCTION

Polymer electrolyte fuel cell systems comprise, in addition to the fuel cell stack, a number of auxiliary components, such as an air compressor or a heat exchanger, which reduce system efficiency. Humidification of the reactant gases is particularly energy sensitive and is to be minimized, which, however, requires fuel cell operation at reduced relative humidity of the fuel and oxidant gas streams.

2 EXPERIMENTAL

The water content and conductivity at room temperature and different relative humidities was measured for three types of proton exchange membranes:

1. Perflurosulfonic acid membranes (various Nafion® membranes: 112, 1135, 115, 1035, 105, 120)
2. Sulfonated polyether ether ketone (sPEEK) membrane with an *IEC*[1] of 1.5 mmol/g.
3. A standard PSI radiation grafted membrane on the basis of 25 µm thick FEP film with 18 % degree of grafting and an *IEC* of 1.4 mmol/g.

The membrane water content was determined by measuring the weight of samples equilibrated in a glove box with defined relative humidity, referenced against the completely dried membrane sample. The conductivity of the membrane samples was measured using AC impedance spectroscopy.

3 RESULTS AND DISCUSSION

The Nafion® and sPEEK membranes show a strong increase in water content between 90 and 100 % R.H., whereas the PSI membrane (FEP-25) shows a lower and more constant level of hydration (Figure 1). This may be explained by the crosslinked nature and thus dissimilar microstructure of the PSI radiation grafted membrane [1].

The measured proton conductivity of the membranes at the different R.H. shows a clear correlation with the respective water content of the membranes (Figure 2), despite the vastly dissimilar chemical composition and microstructure of the materials. It appears that the level of hydration determines to a large extent the proton mobility in the polymer. In order to maximize power output of the fuel cell, the membrane needs to be sufficiently hydrated to provide the necessary proton conductivity.

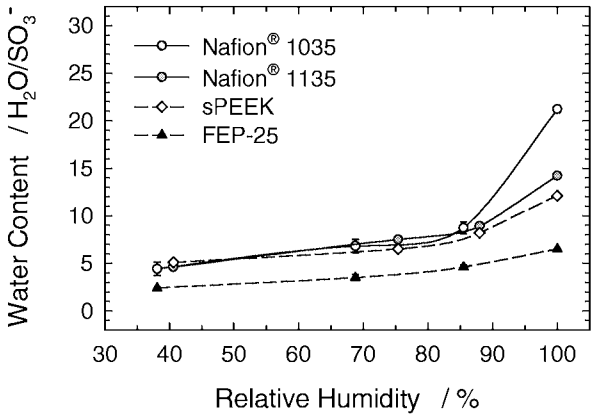

Fig. 1: Membrane hydration, expressed as molecules of water per sulfonic acid group, at room temperature.

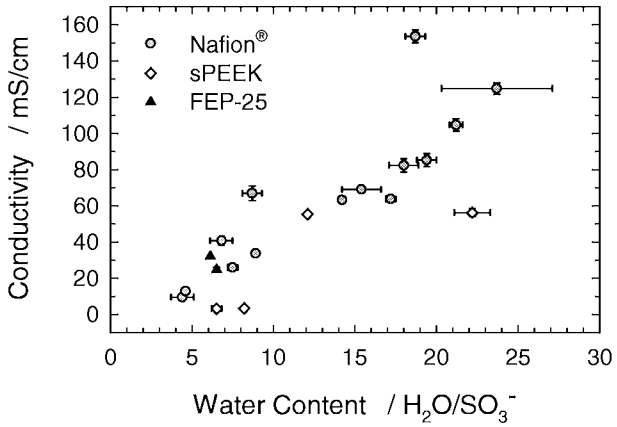

Fig. 2: Proton conductivity at room temperature as a function of water content. Nafion® data includes all Nafion® types investigated (cf. Experimental section).

Water transport properties in fuel cell membranes are reported in another contribution to this volume [2].

4 REFERENCES

[1] K. Mortensen, S. Alkan Gürsel, G.G. Scherer, to be published (2005).

[2] L. Gubler, R. Wälchli, R. Randegger, G.G. Scherer, PSI Scientific Report 2004, **V,** 112 (2005).

[1] *IEC* = ion exchange capacity

WATER MANAGEMENT ASPECTS OF RADIATION GRAFTED FUEL CELL MEMBRANES

L. Gubler, R. Wälchli (ETH Zürich), R. Randegger (ETHZ), G.G. Scherer

The majority of polymer electrolyte membranes for fuel cells rely on the presence of water within their microstructure for the transport of protons. Therefore, the amount and distribution of water within the membrane has a strong influence on performance. The transport properties of water through a commercial and a PSI made membrane were investigated in this study.

1 INTRODUCTION

The mobility of protons in fuel cell membranes and hence the ionic conductivity increases significantly as a function of the water content of the polymer. Ensuring uniform distribution of water within the membrane during fuel cell operation is therefore essential, and the investigation of water management aspects, i.e. the water transport properties in the membrane and membrane electrode assembly (MEA), of crucial importance.

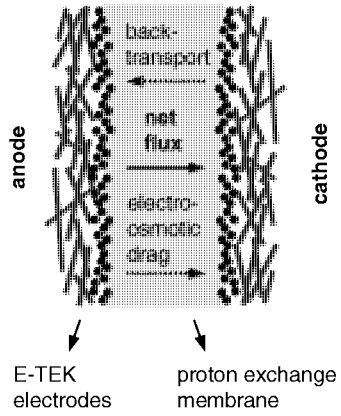

Fig. 1: Mechanisms for water transport in a fuel cell membrane:

i) convective / diffusive transport due to a pressure / concentration gradient, and

ii) water transport coupled with proton flux from anode to cathode (electro-osmotic drag).

Water transport in fuel cell membranes occurs via several mechanisms (Figure 1) [1]. The resulting net water flux through the membrane is determined by MEA components, flow field design and the operating conditions of the cell.

2 EXPERIMENTAL

The water transport properties of two MEAs, using commercially available Nafion® 112 and an in-house fabricated radiation grafted membrane on the basis of 25 µm thick ETFE film (23 % degree of grafting), respectively, and standard carbon cloth based electrodes from E-TEK were assessed by measuring the water rejected from the anode and cathode, and balancing the collected water with water source terms (reactant gas humidification, product water). Three different current densities and two humidification conditions were investigated.

3 RESULTS AND DISCUSSION

The water flux through the membrane is expressed as number of water molecules transported per proton, referred to as *effective drag coefficient* H_2O / H^+ (Figure 2). In case of positive drag, water flows from anode to cathode, and vice versa.

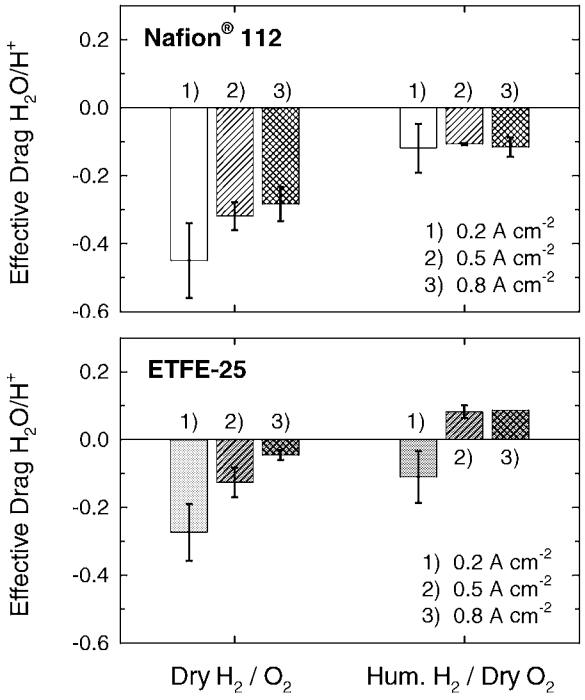

Fig. 2: Net water transport through 2 different fuel cell membranes. 30 cm^2 single cells with serpentine flow field, counter flow operation, 80 °C cell temperature, H_2 / O_2 gas flows 1.5 times stoichiometric, atmospheric pressure.

For both membrane types, net water flux from cathode to anode is observed when the cell is operated with dry H_2 / O_2, which is explained by the existing water concentration gradient because product water is generated on the cathode side. The ETFE-25 membrane shows lower water flux and a stronger dependence on current density, which could be due to a stronger influence of the electroosmotic drag in the ETFE-25 membrane. Using humidified H_2 results in a smaller water concentration gradient, and therefore smaller net water flux in both MEAs. Again, the ETFE-25 membrane shows stronger dependence on current density. One reason for the dissimilar water management properties of the two membranes could be the lower water content of the radiation grafted membrane compared to Nafion® [2].

4 REFERENCES

[1] B. Andreaus, G.G. Scherer, Solid State Ionics **168**, 311 (2004).

[2] L. Gubler, T. Finsterwald, G.G. Scherer, PSI Scientific Report 2004, **V**, 111 (2005).

POLY (ETHYLENE-*ALT*-TETRAFLUOROETHYLENE) BASED MEMBRANES FOR FUEL CELLS: SYNTHESIS AND FUEL CELL PERFORMANCE

S. Alkan Gürsel, L. Gubler, G.G. Scherer

Proton exchange membranes have been synthesized by pre-irradiation grafting of styrene onto poly (ethylene-alt-tetrafluoroethylene) (ETFE) in the presence of divinyl benzene (DVB) as the crosslinker and characterized ex-situ for their fuel cell relevant properties. The optimum graft level was determined as between 20 and 30 %. ETFE based membranes exhibited encouraging fuel cell performance yet, there is room for improvement through optimization of the membrane-electrode interface.

1 INTRODUCTION

Proton conducting membranes prepared by radiation grafting method are promising candidates for fuel cells applications. The favourable polarization properties and successful long-term testing of radiation grafted poly (tetrafluoroethylene-*co*-hexafluoropropylene) (FEP) based membranes have been reported previously [1,2]. Here we focus on the synthesis of radiation grafted membranes using ETFE as the base material due to its superior mechanical properties. The influence of grafting parameters was studied in detail. After subsequent sulfonation the resultant membranes were investigated for their fuel cell performance.

2 EXPERIMENTAL

Radiation grafted membranes were prepared using Tefzel® ETFE film with a thickness of 25 µm from *DuPont* (Circleville OH, USA) as the base polymer, styrene as the monomer and DVB as the crosslinking agent at a ratio of 9:1 (v/v) in water:isopropanol mixture [3].

3 RESULTS

A series of ETFE based grafted films with degree of grafting within the range 2.3 - 69 % mass was prepared by varying the grafting parameters as follows: irradiation dose from 0.75 to 3.5 kGy, grafting temperature (T) from 40 to 90 °C, and grafting time (t) from 40 minutes to 7.5 hours. These three parameters of grafting were identified to have significant effects on the degree of grafting and were subsequently optimized using the design of experiment methodology [3]. The details for preparation conditions for some of the sulfonated ETFE based grafted membranes, which were evaluated in H_2/O_2 fuel cells, are given in Table 1.

Membrane	Dose (kGy)	T (°C)	t (h)	Graft level (%mass)	Graft level (%mol)
ETFE-25	1.5	80	2	19.1	11.7
ETFE-25	1.5	50	6	24.2	14.9
ETFE-25	1.5	80	6	30.4	18.7
FEP-25	3	60	4	18.2	18.0

Table 1: Grafting conditions for the membranes tested in fuel cells.

It was determined that ETFE based membranes exhibited inferior performance compared to Nafion® 112 and FEP based membranes (Figure 1). This may be attributed to both the higher membrane resistance and higher membrane-electrode interface resistance. As far as the ETFE based membranes with different graft level (GL) are concerned, the ohmic resistances exhibit a decreasing trend with increasing GL. This is a consequence of the increasing number of ion exchange sites and hence increasing conductivity. The optimum GL was found to be between 20 and 30 % since at GL below 20 %, the membrane resistance becomes excessively high, whereas GL above 30 %, the mechanical properties of the membranes are insufficient leading to rapid failure in the single cell [4].

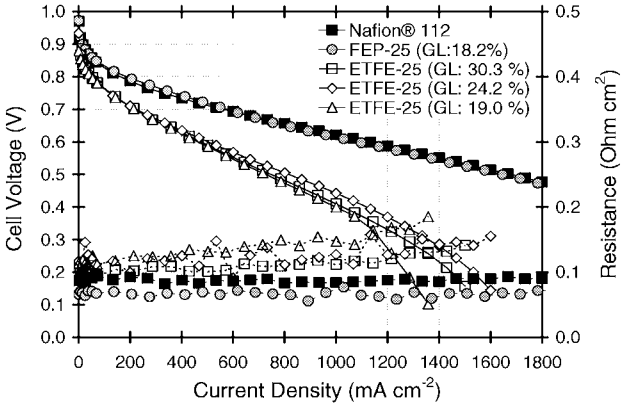

Fig. 1: Single cell performances of ETFE based membranes (carbon cloth electrodes) compared with Nafion® and FEP based membranes (carbon paper electrodes) (Pt loading of 0.6 mg cm^{-2}) at 80°C.

ETFE-25 (GL: 24.2 %), tested over 770 hours, showed no signs of membrane degradation based on the values for fuel cell performance and ohmic resistance. The optimization of the membrane - electrode interface, which was achieved for FEP based membranes [2], will be studied as a next step.

4 REFERENCES

[1] H.P. Brack, F.N. Büchi, J. Huslage, G.G. Scherer, Electrochem. Soc. Proc. 98-**27,** 52 (1998).

[2] L. Gubler, H. Kuhn, T.J. Schmidt, G.G. Scherer, H.P. Brack, K. Simbeck, Fuel Cells **4**, 196 (2004).

[3] S. Alkan Gürsel, H. P. Brack, G. G. Scherer, PSI Scientific Report 2003, **V**, 99 (2004).

[4] L. Gubler, N. Prost, S. Alkan Gürsel, G. G. Scherer, Solid State Ionics, submitted for publication (2005).

FTIR MICROSCOPY FOR POST MORTEM ANALYSIS OF FUEL CELL MEMBRANES

M. Slaski, L. Gubler, G.G. Scherer, A. Wokaun

A fuel cell membrane has been investigated with FTIR microscopy after 8000 hrs of single cell operation at 80°C. Analysis of bands for S=O stretching vibration gave a percentage content of sulfonic acid groups remaining after test, which is related to the membrane degradation. The membrane did not degrade uniformly, overall higher degradation was observed in channel areas compared to the land areas, the strongest degradation was seen close to oxygen inlet area.

1 INTRODUCTION

Radiation grafted proton exchange membranes have performance similar to state-of-the-art materials such as Nafion. Low cost of materials and synthesis based on established industrial processes make them an attractive material for low temperature fuel cells (operating temp. around 80 °C), applicable to hydrogen as well as direct methanol fuel cell. Until now, membranes are usually characterized before fuel cell testing. Membranes were not sufficiently characterized *post mortem* in terms of local degradation.

2 EXPERIMENTAL

The investigated membrane was prepared by grafting of styrene and divinylbenzene (DVB) onto preirradiated poly(tetrafluoroethylene-co-hexafluoro- propylene) (FEP) 25µm, and subsequent sulfonation. For 4000 hrs of operation at 80°C, the fuel cell performance was stable, without significant degradation [1]. The increased occurrence of start-stop cycles subsequently lead to accelerated cell performance degradation. After a total of 8000 hrs operation, the cell was shut down and disassembled, the MEA (membrane electrode assembly) was treated in water at 80°C for 12 hrs, and then the electrodes were gently peeled off. Sulfonic acid groups of the membrane were exchanged in aqueous solution of potassium chloride to convert them into potassium salt form, and the membrane was dried. FTIR measurement was carried out with FTIR spectrometer BIO-RAD FTS 175 coupled with IR microscope UMA 500, spatial resolution 100µm x 100µm. FTIR spectra were recorded in land and channel areas and as a reference (not degraded area) points at the edge outside the active area were measured. The area of the peak at 1039 cm^{-1} (S=O stretching vibration) was integrated for each point, the edge area representing 100% of sulfonic acid groups, the rest of the values and bars represent remaining percentage of sulfonic acid groups.

3 RESULTS

In the picture of membrane the flow field structure is visibly imprinted, also the area looks not uniformly degraded (Figure 1). The measurement made in channels and lands have shown generally higher loss of acid groups in channel areas than in land areas, possibly due to limited access of gas in active sites under the lands. Area close to oxygen inlet (sector 2) is more degraded than the center part of the membrane (sector 1). Strong degradation of the sector 2, which is located close to oxygen inlet, could be explained by lower membrane hydration caused by feeding of dry oxygen.

4 CONCLUSIONS

Degradation of fuel cell membranes does not occur uniformly over the active area, it strongly depends on a configuration of a fuel cell. FTIR microscopy gives unique information about local degradation of a fuel cell membrane, which could be used in optimization of fuel cell operating conditions, components used and flow field design.

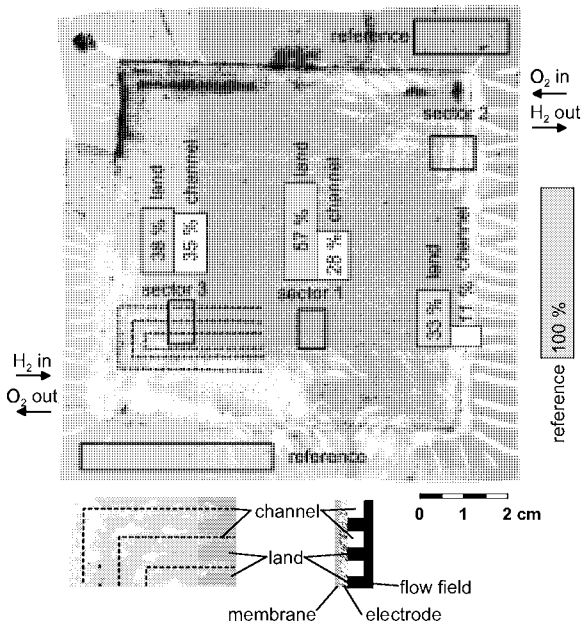

Fig. 1: Picture of the membrane after 8000 hrs of performance in fuel cell, at a cell temperature of 80°C, with marked sectors of FTIR measurement. The contrast was electronically enhanced.

5 ACKNOWLEDGEMENTS

We would like to thank Manfred Schmid of EMPA for the assistance during the FTIR microscopy measurement and the Swiss Federal Office of Energy for continued financial support.

6 REFERENCE

[1] L. Gubler, H. Kuhn, T.J. Schmidt, G.G. Scherer, H.-P. Brack, K. Simbeck, Fuel Cells **4**, 196 (2004).

INFLUENCE OF ELECTROLYTE THICKNESS ON WATER AND METHANOL CROSS-OVER IN DIRECT METHANOL FUEL CELLS

D. Kramer, L. Gubler, G.G. Scherer, A. Wokaun

Direct Methanol Fuel Cells (DMFC) are energy converters with characteristics particularly interesting for portable applications due to the high energy density implied by the direct feed of a liquid fuel. However, the high permeability of commercial standard electrolytes for methanol and water is detrimental to performance and efficiency, because permeating methanol forms a mixed potential at the cathodic electrode and the additional flux of water from anode to cathode might impede the accessibility of the cathodic electrode for oxygen by flooding the porous structures of electrode and gas diffusion layer. In order to derive strategies for new electrolyte materials, the impact of membrane thickness has been investigated utilizing the commercial standard electrolyte "Nafion" in three thicknesses.

1 INTRODUCTION

The power output of DMFC is considerably lower than that of its hydrogen-fuelled analogue. This is partially due to the cross-over of water and methanol from the anode to the cathode. The influence of membrane thickness onto those cross-membrane fluxes and the relation to electrochemical performance has been investigated. Thereby, the use of a suitable reference electrode [1] allowed the separate investigation of the cathodic contributions to the overall voltage loss.

2 EXPERIMENTAL

All experiments were performed with 30 cm^2 single-cells, which were equipped with a perimeter-placed dynamic hydrogen electrode as reference electrode. The permeation of methanol under load-free operation was derived from the carbon dioxid concentration of the cathodic effluent, assuming a 100% conversion of crossing methanol at the cathode. The permeation of water was likewise determined by collecting and measuring the water carried out of the cell with the cathodic effluent. Varied was the membrane thickness, whereas electrodes, flow fields and cell housing were alike.

3 RESULTS

The diagram of Figure 1 shows the permeation rate of water and methanol under load-free operation as a function of membrane thickness at an operating temperature of 60 °C at near ambient pressure. The used membranes were Nafion 112, 115 and 117. It is remarkable that the water flux over the membrane does not depend on of electrolyte thickness (in the range of investigated thicknesses). Obviously, the membrane itself does not represent the rate-limiting mass transport resistance for the water permeation. On the other side, the permeation of methanol is non-linearly increasing with decreasing electrolyte thickness. The non-linearity is a consequence of a superposition of water and methanol fluxes, as can be derived from a simplified model for the methanol permeation (model predictions are shown as dashed lines in Figure 1). The model describes the membrane as fixed porous system with diffusive methanol permeation within a constant flux of water. From the performance point of view, a thicker electrolyte is beneficial (Figure 2) only in the low current density region due to a lower polarisation (higher voltage) of the cathode (inset Figure 2). At higher current densities increased ohmic losses and lower cathode polarisation are counter-balanced.

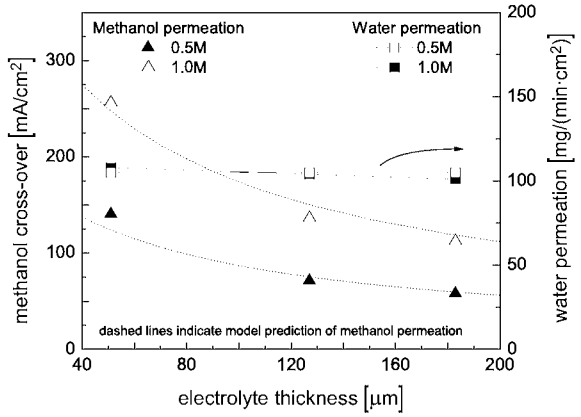

Fig. 1: Methanol and water permeation as a function of membrane thickness for Nafion membranes.

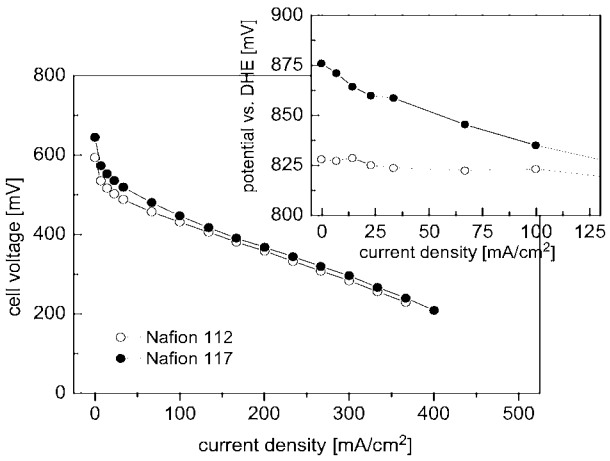

Fig. 2: Polarisation curves for DMFC with Nafion 112 and 117 at 60°C 1bar(a); oxidant is air; inset shows cathodic polarisation at low current densities.

4 REFERENCE

[1] D. Kramer et al., PSI Scientific Report 2003, **V**, 106 (2004).

PREPARATION OF MICROGRAFTED POLYMER FILMS

S. Alkan Gürsel, G.G. Scherer, C. Padeste, H.H. Solak

Micro- and nanostuctured polymer materials have been fabricated by the combination of selective irradiation of polymer substrates with X-rays and subsequent grafting of a second polymer. Spatially defined grafting of styrene throughout the thickness of fluoropolymer films was achieved.

1 INTRODUCTION

The fabrication of polymer structures by selective exposure of fluoropolymer films with soft X-rays or electrons and subsequent grafting of other polymers on the exposed areas was achieved previously [1,2,3]. The grafting reaction indicated good selectivity between the exposed and non-exposed areas. The aim of this study was to perform the spatially defined grafting of styrene throughout the thickness of poly(tetrafluoroethylene-*co*-hexafluoropropylene)(FEP) and poly(ethylene-*alt*-tetrafluoroethylene)(ETFE) films.

2 EXPERIMENTAL

A Cr K X-ray tube source was used for the lithographic exposures. 10x10 cm^2 pieces of 100 µm ETFE (Nowofol) and 25 µm FEP (DuPont) were mounted on an x-y stage to allow multiple exposures on each sample. The FEP and ETFE films irradiated by the exposure to X-rays through a metal mesh were grafted using a solution of the monomers styrene and divinyl benzene (DVB) in an isopropanol/water mixture at 60°C for varying grafting times, and then sulfonated. Atomic Force Microscopy (AFM) was used to determine the surface profiles of the micrografted samples. Staining of the grafted and sulfonated regions of the polymers was achieved by using a solution of methylene violet dye in water.

3 RESULTS

The micrographs of grafted FEP films show the formation of more pronounced structures with increasing exposure time (Figure 1).

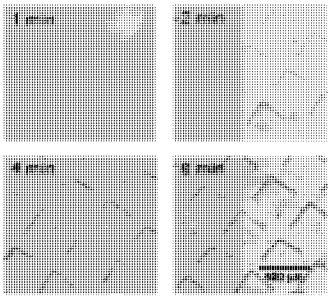

Fig. 1: Optical micrographs of styrene/DVB grafted FEP films after X-ray exposure though a metal mesh for 1 to 8 minutes.

The relationship between dose and graft level was assessed by AFM and profilometer measurements of the microstructured regions. The thickness increase in the grafted areas was calculated from the step heights assuming similar grafting on both sides of the polymer film. An approximately linear dependence of thickness increase on X-ray dose and on reaction time was determined (Figure. 2).

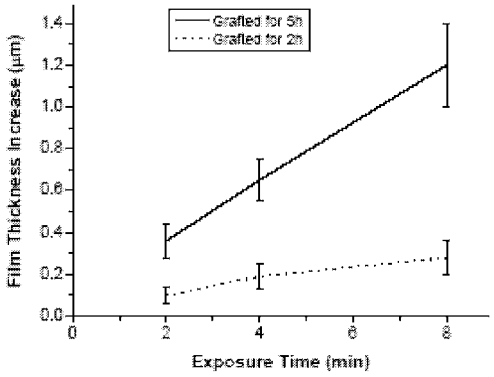

Fig. 2: Dependence of film thickness increase on exposure dose and grafting time measured by profilometer for styrene/DVB grafted FEP films.

Indicator dyes can be selectively diffused into the grafted parts of the films due to the ion-exchange capabilities of the sulfonated polystyrene. Although an even distribution of the dye throughout the thickness of the 25 µm FEP was obtained, a considerable difference in the front and back-sides of the 100 µm ETFE film was observed (Figure 3).

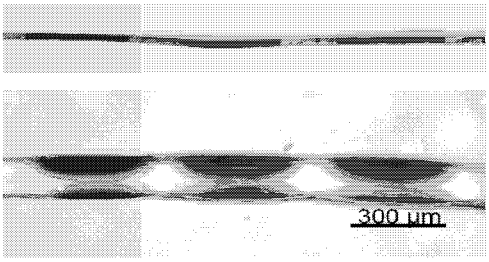

Fig. 3: Optical micrographs of a cross-section view through grafted, sulfonated and stained polymer films; top: 25 µm FEP, bottom: 100 µm ETFE.

The described process allows controlled grafting through fluoropolymer films with micrometer resolution. Local modification of the properties of polymer films, such as ion conductivity, diffusion of molecules, and optical properties will be studied.

4 REFERENCES

[1] H.P. Brack, C. Padeste, M. Slaski, S. Alkan, H.H. Solak, J. Am. Chem. Soc. **126**, 1004 (2004).

[2] European Patent Application EP 03 016 889.2.

[3] C. Padeste, H.H. Solak, H.P. Brack, M. Slaski, S. Alkan Gürsel, G.G. Scherer, J. Vac. Sci. Technol. B **22**, 3191 (2004).

FABRICATION AND CHARACTERIZATION OF MICROSTRUCTURED GLASSY CARBON ELECTRODES FOR MICRO FUEL CELLS

M. Kuhnke, T. Lippert, G.G. Scherer, A. Wokaun

Micro-structured electrodes with an integrated flow field of 1 cm^2 ("flow field electrodes") were fabricated in glassy carbon (GC) by a combined laser and reactive ion etching process. At a depth of 52 µm, the laterally traversing channels provide an electrochemically active surface area of 3.75 cm^2.

1 INTRODUCTION

Micro structured glassy carbon is an interesting material for the fabrication of electrodes for micro fuel cells because it is chemically inert and electrically conductive. Typically, these structures have a depth of > 100 µm and a width of ≈ 50 µm. A large surface area is also desirable and can be obtained with high aspect ratio channels and high surface roughness.
We have developed a process that combines the structuring of a metal mask by laser ablation with a subsequent reactive ion etching (RIE) step. Channels fabricated with this method exhibit a rough surface and provide sufficient surface area for fuel cell operation without the use of separate gas diffusion electrodes. An alternative structuring process is laser direct writing, which produces less surface roughness, but higher aspect ratio. In both cases the Pt catalyst is sputter-deposited into the channels.

2 MICROFABRICATION

Glassy carbon (G-type, HTW Germany) was polished with a diamond suspension and coated with a 600 nm thick Al layer. The mask writing was done on a computer controlled xyz stage by a XeCl laser (308 nm), enabling us to write lines with a width of < 30 µm. The processing time for a 1 cm^2 flow field mask is about 1 h. After mask preparation, the pattern was transferred into the GC substrate by a RIE step in oxygen plasma.

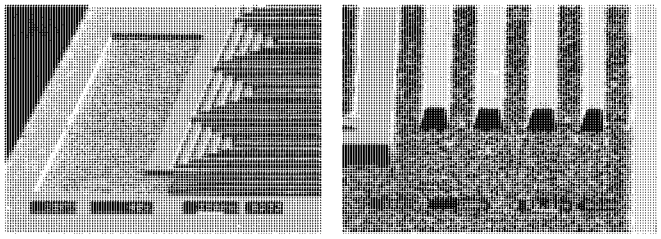

Fig. 1: Micro flow field of 5 parallel channels (pitch 100 µm, depth 52 µm) traversing a 1 cm^2 area.

3 CHARACTERIZATION RESULTS

Micro structured electrodes are expected to become valuable models for studying interface processes in the H_{upd} region. Used in micro fuel cells, they can e.g. help to understand the transport of H^+ on Pt-coated surfaces. A comparison of the geometric surface area of electrodes with various channel depths with their electrochemically active area will provide information on the maximum depth in which a catalyst can be utilized. Thus, the active area of the micro fuel cells is one of the most interesting parameters and this can be determined by cyclic voltammetry (CV).

The CV of a RIE-structured electrode fully immersed in electrolyte exhibits the typical H-adsorption and desorption peaks of Pt (Figure 2). The active surface area calculated from the CV of the RIE-structured electrode is 3.75 cm^2, compared to a geometric area of 1.8 cm^2. Assuming a Pt roughness factor of 1.3 (resulting from sputtering), this corresponds to a Pt usage of 160%, caused by the GC surface roughness.

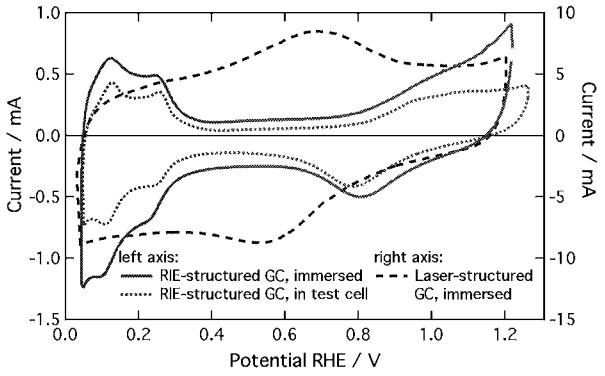

Fig. 2: CVs of micro structured and Pt-coated GC electrodes recorded at a scan rate of 100 mV/s.

In the case of laser-structured electrodes it was impossible to determine this area, as the CV does not show any hydrogen adsorption or desorption. Possible reasons for this were that either the CV of the electrode immersed in a 0.5 M H_2SO_4 electrolyte is dominated by the carbon surface or that the Pt does not have a good electrical contact to the GC. This question was answered by measuring the CV of the RIE-structured electrode in a test cell that allows only the patterned area to be in contact with the electrolyte and compare it to the CV of the immersed electrode. Both CVs are very similar, with the immersed cell providing a slightly higher surface area, as parts of the unpatterned area are also Pt-coated. As the immersed carbon surface does not significantly influence the CV, we assume that there is an increased contact resistance towards the GC surface, possibly caused by surface oxidation during the laser writing (355 nm, 8 kHz, 0.24 mJ/42 ns pulse, pulse power 5.7 MW).

A micro fuel cell was assembled from two RIE-structured electrodes and a Nafion 115 membrane between two stainless steel end plates. The maximum open circuit potential was about 880 mV, the highest current was 1.46 mA at 200 mV. As a comparison: an E-TEK electrode with a 672 $cm^2_{Pt}/1cm^2_{geom.}$ operated at 1 $A/cm^2_{geom.}$ delivers 1.5 mA/cm^2_{Pt}. Assuming comparable catalytic activity, this means that less than 1 cm^2 of Pt was really used in the fuel cell. Possible explanations are channels blocked by a pressed-in membrane or flooding of several channels.

IN SITU ATOMIC FORCE MICROSCOPY STUDIES OF CATION INSERTION INTO GRAPHITE IN SUPERCAP-TYPE ELECTROLYTE

F.P. Campana, M. Hahn, A. Foelske, R. Kötz, H. Siegenthaler (University of Bern)

Film formation and intercalation processes at supercapacitor electrodes have been widely neglected in the past. The formation of a surface film on and the intercalation of ions and/or solvent into highly oriented pyrolytic graphite (HOPG) in $(C_2H_5)_4NBF_4$ / propylene carbonate – a typical electrolyte used in supercapacitors – were investigated using in situ atomic force microscopy (AFM). A significant expansion of the steps was observed at 1.0 V vs. Li/Li$^+$, indicating the intercalation of tetraethylammonium cations. In addition film formation occurs at an electrode potential of 0.7 V vs. Li/Li$^+$.

1 INTRODUCTION

Supercapacitors (SC) are well known not only for their extraordinary power density but also for their extreme robustness and cycle stability. The latter is usually ascribed to the fact that charge storage is solely based on rearrangement of ionic charges in the double layer. For a typical double layer capacitor chemical reactions like oxidation/reduction or intercalation are excluded.

In order to increase energy density of SC it would be desirable to increase the nominal SC device voltage from currently 2.5 V to significantly higher values of up to 4 V. At such high voltages, however, the occurrences of processes other than double layer charging have to be considered.

2 EXPERIMENTAL

In situ contact-AFM measurements were performed in propylene carbonate (PC) with 1M $(C_2H_5)_4NBF_4$. The working electrode was highly oriented pyrolytic graphite (HOPG, ZYA-type). Counter and reference electrode were made from an activated carbon powder. At a given potential (between 3 V and 0.5 V vs. Li/Li$^+$) the step height was determined by an average of 5 areas on different locations on two arbitrarily selected steps for 2 different images. The step heights were 3 and 10 graphene layers, respectively.

3 RESULTS

Figure 1 shows two AFM topography images (3D) at the same location on a HOPG electrode in $(C_2H_5)_4NBF_4$ / PC at two different potentials; close the rest potential at 3.0 V vs. Li/Li$^+$ (Figure 1a) and negatively charged at 1.0 V vs. Li/Li$^+$ (Figure 1b).

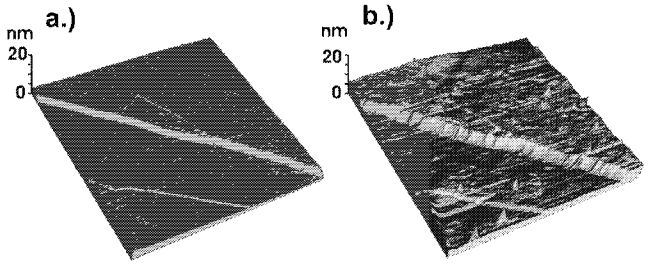

Fig. 1: *In situ* contact-AFM images (1.5 µm x 1.5 µm) of HOPG in PC with 1M $(C_2H_5)_4NBF_4$ at the same location. a) At 3 V vs. Li/Li$^+$. b) At 1 V vs. Li/Li$^+$.

The observed step height changes of 70 % (large step) and 100 % (small step) are somewhat larger than the macroscopic electrode height change of about 40 % found by dilatometry for a graphite powder electrode [1]. The discrepancy might be due to the lower anisotropy of the powder sample, according to which only part of the interlayer expansion results in a macroscopic height change. The intercalation of tetraethylammonium ions from aprotic solutions was already hypothesized by Besenhard et al. [2]. However, up to now such processes were hardly considered for activated carbon based super-capacitors. The spikes observable on the HOPG surface at 1.0 V vs. Li/Li$^+$ (Figure 1b) may be attributed to an initial film formation as the formation of a closed film could be observed at slightly more negative potential (Figure 2).

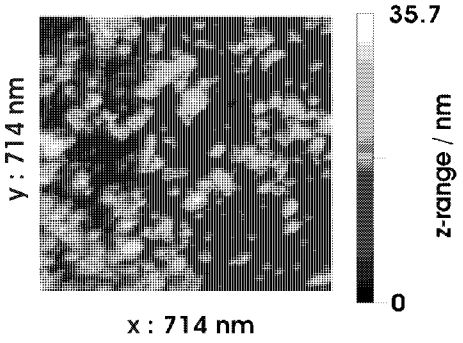

Fig. 2: *In situ* tapping-AFM image (0.7 µm x 0.7 µm) of HOPG in 1M $(C_2H_5)_4N$ BF_4 / PC at 0.7 V vs. Li/Li$^+$.

Figure 2 shows an AFM topographic image recorded at a potential of 0.7 V vs. Li/Li$^+$ after 10 minutes. The generated film is clearly visible and exhibits a globular structure. The film has an rms roughness of 4.3 nm and an average thickness of 11 nm.

In conclusion, cathodic film formation and cation insertion have to be taken into account as voltage limiting processes for supercapacitors.

4 ACKNOWLEDGEMENT

Financial support by the Swiss National Foundation, grant no. 21-59224.99, is gratefully acknowledged.

5 REFERENCES

[1] M. Hahn et al., Appl. Phys. A (2005), submitted.

[2] J.O. Besenhard, H.P. Fritz, J. Electroanal. Chem. **53**, 329 (1974).

CHARGE INDUCED EXPANSION OF SUPERCAPACITOR ELECTRODES

M. Hahn, O. Barbieri, F.P. Campana, R. Gallay (Maxwell SA, Rossens), R. Kötz

The height change of an activated carbon supercapacitor (SC) electrode upon charging has been measured. The onset of a small but distinct expansion was observed at about ± 1 V remote from the immersion potential, well within the typical SC operating range. This finding suggests that – in contrast to common opinion – intercalation processes play an important role for charge storage and life time limitation of SCs.

1 INTRODUCTION

The much better cycle life performance of today's SCs when compared to batteries is generally ascribed to the circumstance that charge storage is based on pure double layer charging, and not on Faradaic reactions. Such reactions are often accompanied by microscopic structural changes, which may be not fully reversible and thus limit the cycle life of batteries.

Commonly microscopic structural changes result in macroscopic dimensional changes. Consequently, dilatometry is an appropriate means to distinguish between Faradaic and capacitive processes.

2 EXPERIMENTAL

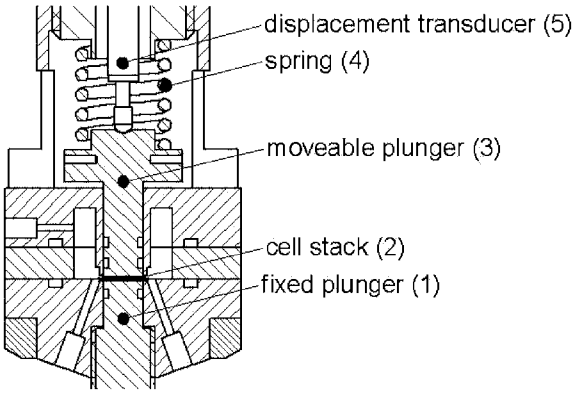

Fig. 1: Cross sectional view of the dilatometer. The cell stack (not shown in detail) is held between two plungers (1 and 3).

The home made dilatometer (Figure 1) consists of a cell stack, i.e. two activated carbon SC electrodes separated by a paper separator. This assembly is soaked with the electrolyte solution, 1 mol/l $(C_2H_5)_4NBF_4$ in acetonitrile. The upper electrode (WE) is free to move against a constant load (20 N) applied by means of a spring. The lower (and much bigger) electrode is fixed and serves as the counter electrode (CE). The overall height change of the cell is monitored by an inductive displacement transducer mounted on top of the plunger which contacts the WE. Due to its much higher capacitance the potential and the height of the CE remain unchanged during charging. Accordingly the measured expansion can be solely attributed to the WE.

3 RESULTS AND DISCUSSION

The results obtained with one and the same electrode, first for cycling in the negative, then for cycling in the positive potential range, are shown in Figure 2. For the negative range (0 to -2 V) the voltammogram (CV) shows almost ideal capacitive behaviour with 99.5 % Coulomb efficiency (3rd cycle). A maximum height change of 5 µm (3.3 %) with the onset at about -1 V vs. the immersion potential (ip) is observed. For the positive range (0 to 2 V) the height change is smaller but no longer fully reversible, and a continuous swelling of the electrode is evident during cycling. At the same time, the CV shows some irreversible features with a Coulomb efficiency of only 75.5 %. Again, the onset of expansion is found at about 1 V vs. ip.

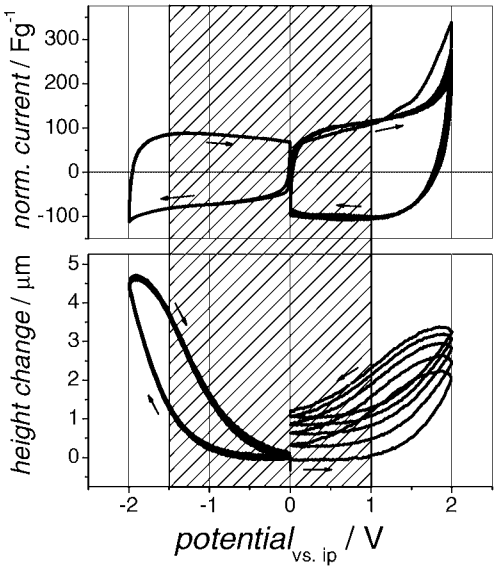

Fig. 2: CV (top) and simultaneous height change (bottom) of a 150 µm thick supercap electrode. The SC operation window is indicated.

Recently we have shown that the observed height change can be attributed to ion intercalation into the nanometer sized graphite crystallites of which the electrode material consists [1]. The onset of expansion is observed for a capacitor voltage well within the SC operating window of 2.5 V. We thus conclude that these intercalation processes are important not only for the mechanism of charge storage but also for understanding degradation processes.

4 ACKNOWLEDGEMENTS

We thank the Swiss CTI (project no. 5807.2 KTS-NM, and 5945.2 TNS) and Maxwell Technologies SA, Rossens, for financial support.

5 REFERENCE

[1] M. Hahn, O. Barbieri, F. Campana, R. Kötz, R. Gallay, Appl. Phys. A, submitted.

PREPARATION OF A 100 F SUPERCAPACITOR DEMONSTRATOR

O. Barbieri, M. Hahn, R. Gallay (Maxwell SA, Rossens), R. Kötz

Within the TopNano 21 project "Synthesis of supported, nanostructured, high porosity carbon as electrode material", a cooperation with the University Fribourg, EMPA in Dübendorf, Maxwell Technologies SA in Rossens and Timcal SA in Bodio, we investigated and optimized different carbons as electrode materials for supercapacitors. As a deliverable in this project a demonstrator was successfully built and tested.

1 INTRODUCTION

The production of commercial supercapacitors with the highest performance at the lowest cost is a major goal for all the companies working in this field. Within the TopNano project "Synthesis of supported, nanostructured, high porosity carbon as electrode material" we defined which are the morphological properties of carbon samples controlling the electrochemical performance of supercapacitor electrodes. According to these findings we then produced some electrodes using an optimized carbon provided by Timcal SA and built a demonstrator in collaboration with Maxwell Technologies SA.

2 EXPERIMENTAL

From the raw carbon powder we produced the electrodes of the demonstrator. First, the carbon powder was mixed with a solution (1:1) of isopropanol and deionised water with a 1:5 weight ratio. A colloidal PTFE solution was added as a binder so that we obtained a binder content of 20 wt-% in the dry electrode. Acetone (in a weight ratio of 2:1 with the carbon) was added to the continuously stirred mixture to precipitate the PTFE homogeneously. After evaporation of most of the liquid the obtained paste was rolled to a 0.20 mm thick film and dried at room temperature.

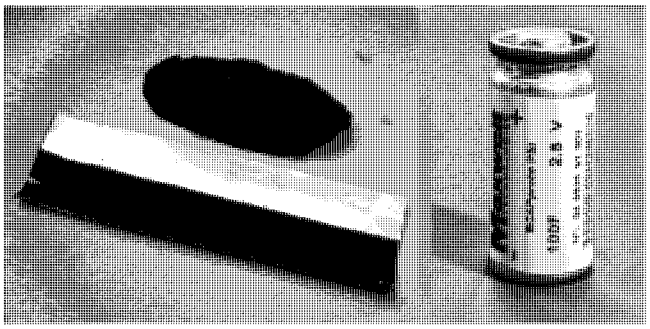

Fig. 1: Freestanding electrode film, film attached to the aluminium stripe, and final supercap device.

From the film we cut 100 × 45 mm^2 ribbons which we glued on 300 × 65 mm^2 aluminium stripes serving as the current collectors (see figure 1). The conductive primer used to glue the ribbons on the stripes were made of graphite and a polymeric binder. We prepared 2 meters of such multilayer electrodes which were then assembled in a commercial D-cell housing (see figure 1) following the standard winding procedure established by Maxwell Technologies SA. The demonstrator was then soaked with the electrolyte, an aprotic solution of 1 mol/L $(C_2H_5)_4NBF_4$ in acetonitrile.

3 RESULTS

Some performance data of the demonstrator are shown in table 1 and compared with the performance of a state-of-the-art commercial supercapacitor, BCAP0350, with the same housing.

	C (F)	R_s (mΩ)	τ_s (s)	C_{el} (F/g)
Demo	100	8.6	0.86	66
0350	350	3.2	1.12	60

Table 1: Some performance data of the demonstrator compared to a state-of-the-art supercap. The parameters C, R_s, τ_s are given for the device, C_{el} is given for the electrode level.

For technical reasons the demonstrator device contains a much smaller electrode area than its counterpart BCAP0350. Therefore the total capacitance C is significantly lower, nevertheless the electrode mass-specific capacitances C_{el} (neglecting the effect of package density) are comparable. For the same reason the DC series resistance R_s is much higher than the corresponding value of the commercial device.

However, a comparison of the time constant $\tau_s = R_s C$ reveals, that the time response of the demonstrator is even slightly better than that of BCAP0350. This last parameter is important as it described the time needed to charge and discharge the device. The small R_s and τ_s are due to the particular porous morphology of the carbon combining both micropores and mesopores.

In conclusion, the demonstrator electrode shows excellent values of capacitance and power capability. On the device level, a substantial enhancement of the package density is needed. One measure to achieve this goal could be to increase the density of the carbon itself.

4 ACKNOWLEDGEMENTS

Financial support of this project by the Swiss CTI (project # 5807.2 KTS-NM, and #5945.2 TNS), by Maxwell Technologies SA in Rossens, Switzerland and TIMCAL SA in Bodio, Switzerland is gratefully acknowledged.

MEASUREMENT AND ESTIMATION OF SUPERCAPACITOR LIFE TIME

M. Hahn, O. Barbieri, J.-C. Sauter, R. Kötz

The lifetime of a 350 F electrochemical double layer capacitor (EDLC) was estimated on the basis of leakage current measurements at various temperatures and voltages. Acceleration factors for the degradation processes at increased temperature and voltage were determined from Arrhenius type plots of the measured leakage currents. For standard conditions, a lifetime of more than 100 years was estimated.

1 INTRODUCTION

Electrochemical double layer capacitors (EDLC) are known as high power storage devices, which exhibit very good cycle life performance [1]. Today's capacitor manufacturers guarantee 500'000 full charge / discharge cycles. Life tests are very time consuming and it is therefore important to develop accelerated life tests which allow lifetime estimations under varying conditions. Therefore, life tests are performed at elevated temperatures and at voltages exceeding the nominal voltage, in order to accelerate the degradation processes.

2 EXPERIMENTAL

The leakage current of a commercially available EDLC (BCAP0350, Maxwell SA) with a nominal capacitance of 350 F was measured at various potentials between 2.5 V and 3.0 V and temperatures between -40 °C and +60 °C. In regular time intervals the capacitance and the equivalent series resistance (ESR) of the capacitor was measured by electrochemical impedance spectrometry (EIS).

3 RESULTS

We assume that the leakage current measured during the constant voltage test can be correlated to degradation processes [2]. For an ideal capacitor the leakage current should be zero. Plotting the leakage current as a function of temperature in an Arrhenius plot should allow estimating the respective activation energy.

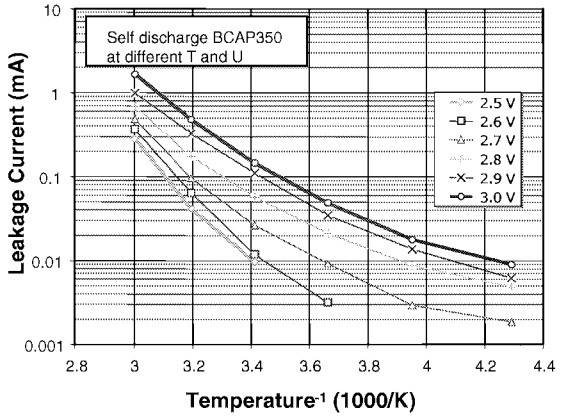

Fig. 1: Arrhenius plot for the leakage current of a 350 F EDLC at temperatures between -40 °C and +60 °C at various voltages.

Figure 1 shows the Arrhenius plot of the leakage current at various capacitor voltages. Unfortunately the data do not result in straight lines. Nevertheless, it is possible to estimate acceleration factors from fig. 1. An increase of 10 °C in temperature will accelerate degradation by a factor of 1.7 ... 2.4, and an increase of the voltage by 0.1 V will result in an increase of the degradation processes by a factor of 1.5 ... 2.

Figure 2 shows a log/log plot of capacitance and ESR during the constant load test of a BCAP0350 at 25 °C and 2.5 V. The end of life criteria for the capacitor is defined as a 20% capacitance loss and/or a 100 % ESR increase.

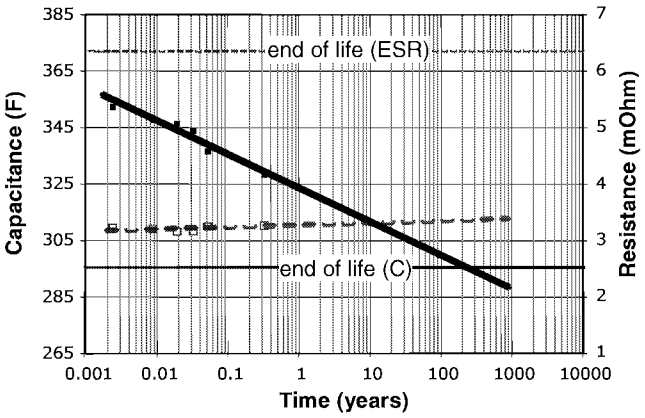

Fig. 2: Capacitance fading (full line) and ESR increase (dashed line) of an EDLC at 25 °C and 2.5 V.

Clearly, by this definition, the end of life is given by the observed capacitance fading. At 25 °C and 2.5 V the lifetime of the capacitor is estimated to more than 100 years. Using the above determined acceleration factors the lifetime of the capacitor at 25 °C and 3.0 V would reduce to ~10 years. A capacitor at 65 °C and 2.5 V would perform well for ~10 years. This is still acceptable for many applications.

4 ACKNOWLEDGEMENTS

Financial support of this work by the Swiss CTI (project # 5807.2 KTS-NM, and # 5945.2 TNS) and by Maxwell Technologies SA, Rossens (CH), is gratefully acknowledged.

5 REFERENCES

[1] R. Kötz, M. Carlen, Electrochimica Acta **45**, 2483-2498 (2000).

[2] C.R. Feger, T.F. Strange, Passive Component Industry, November/December, 22 (2002).

SURFACE DISORDER DETECTION ON GRAPHITE ELECTRODES

L.J. Hardwick, P. Novák, H. Buqa, A. Wokaun

Graphite is the principle material in negative electrodes in the lithium ion battery. Subtleties in the structural arrangement of graphite affect the electrochemical performance of this material. The relationship between its nano-, micro- and defect structure with the mechanism of lithium ion insertion is currently being studied. Raman spectroscopy has been shown to be pertinent in the investigation of the surface region of carbonaceous materials, therefore ex situ Raman microscopy was used to study surface disorder on graphite electrodes at a confocal resolution of around 1 μm^3. Results show it may be possible to "image" electrodes using their L_a values and therefore show the correlation of L_a with the morphology of the surface of the electrode. A Raman in situ cell was used to investigate the correlation between surface disorder and lithium content in graphite. Early results show that encouragingly a distribution of lithium content is observed on the graphite exterior.

1 INTRODUCTION

Graphite is the preferred material for lithium-ion battery negative electrodes, on account of low cost and non toxicity. Raman microscopy is well suited for the study of carbonaceous materials. The surface of graphite electrodes is extremely disorganised on the micrometer scale. High number point mapping of graphite electrodes with confocal Raman microscopy allows the analysis of its surface heterogeneity. The first order spectrum of graphite (Figure 2 top) consists of two main bands observed at 1330 cm^{-1} and 1580 cm^{-1} these are known respectively as the D and G bands. From the area ratio of the D and G band and by using the Tuinstra and Koenig equation the L_a value can be calculated [1]. The L_a value is an important parameter of graphite which provides a measure of local surface disorder and represents the length of the graphene crystallite sheets.

2 EXPERIMENTAL

The *ex situ* mapping technique and the *in situ* cell experimental set up are described elsewhere [2] and references therein.

3 RESULTS AND DISCUSSION

Figure 1 shows the (a) image of the graphite surface and (b) the L_a map created from the ratios of the D and G bands of graphite. From comparing both images the correlation between the surface morphology and the L_a value can be observed.

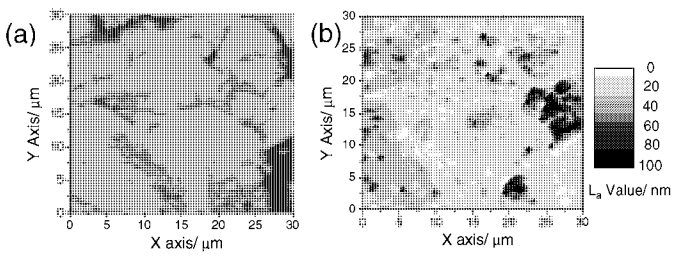

Fig. 1: *Ex situ* Raman mapping of graphite surface showing the comparison of (a) the optical picture of the surface of graphite and (b) the high number point L_a map; 50 x 50 points; 2500 spectra.

Lithium intercalation is examined by the comparison of Raman maps at open circuit potential (OCP) ca. 3 V and at 150 mV vs. Li/Li^+. At 150 mV a phase change is observed from a stage 4 graphite intercalation compound (GIC) to a stage 3 GIC. The spectra measured at this potential consist of a G band doublet. It is possible to relate the doublet structure of a GIC to its stage index [3] by the intensity ratio of the interior, $E_{2g2}(i)$ and bounding, $E_{2g2}(b)$ layer bands (Figure. 2).

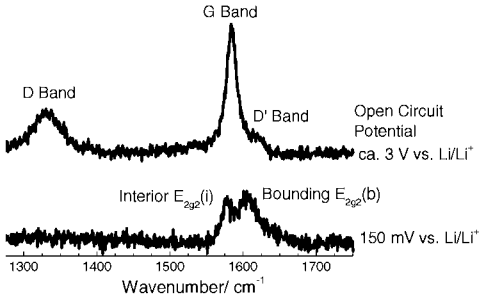

Fig. 2: The Raman spectra of graphite at OCP (ca. 3.0 V vs. Li/Li^+) and at 150 mV vs. Li/Li^+.

The comparison of the L_a (disorder) map and the lithium content map is shown in Figure 3. No correlation between disorder and content can yet be observed with these preliminary maps, though the content map does encouragingly show a variation in lithium content. Obviously more points per map should be measured and this will be the context of our future work.

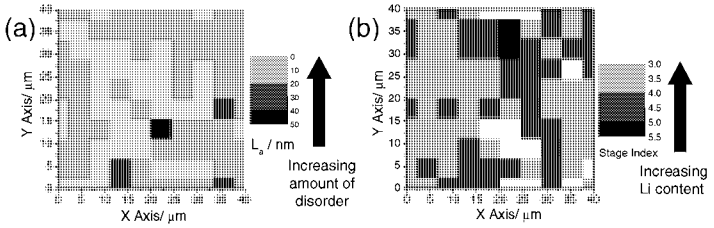

Fig. 3: (a) L_a map of graphite (OCP ca. 3.0 V vs. Li/Li^+) and (b) lithium content map (150 mV vs. Li/Li^+) 10 x 10 points; 100 spectra (bad points in white).

4 REFERENCES

[1] F. Tuinstra, J.L. Koenig, J., Chem. Phys. **53,** 1126 (1970).

[2] P. Novák et al., J. Power Sources, in print (2005).

[3] M. Inaba et al., J. Electrochem. Soc. **142,** 20 (1995).

IN SITU INVESTIGATION OF CATHODES OF LITHIUM-ION BATTERIES

A. Würsig, J. Ufheil, M. Holzapfel, W. Scheifele, F. Krumeich (ETH Zürich), P. Novák

The gas evolution and film formation on cathode materials in lithium-ion batteries was studied using post mortem scanning electron microscopy (SEM) and differential electrochemical mass spectrometry (DEMS). The influence of additives on these processes was shown with vinylene carbonate (VC), which is able to significantly reduce the CO_2 gas evolution in the commonly used potential window between 3 V and 4.3 V. By long time cycling experiments it was demonstrated that, additives can improve the durability of lithium-ion batteries.

1 INTRODUCTION

During the last years, the efforts to identify and investigate new, improved electrode materials for secondary lithium-ion batteries have been increased significantly. However, the electrochemical potential of most of these materials is far beyond the thermo-dynamic stability window of the most commonly used organic electrolytes. Hence, reductive and oxidative electrolyte decomposition leads to gas evolution within the electrochemical cell. This increases the internal pressure, which may result in larger safety risks and reduced cycle stability. Fortunately, the SEI film formed at the surface of negative electrode materials prevents further reductive electrolyte decomposition. A similar protective film has also been reported for positive intercalation materials, and it has been shown, that primarily CO_2 is formed by oxidative decom-position processes on the oxide surface. Unfortu-nately, the parameters influencing the formation of a cathodic SEI are yet not well understood.

2 EXPERIMENTAL

Since the amount of CO_2 formed by oxidative electrolyte degradation is rather low, a totally new DEMS measurement cell had to be developed, which allows increasing the mass and the surface of the electrode. A schematic view of this cell is shown in Figure 1. Scanning electron mi-croscopy (SEM) was carried out on a LEO 1530 Gemini field-emission microscope, which was operated at low voltage (usually 1 kV) to achieve a suitable contrast of the surface details in the secondary electron images and to minimize the charging of the uncoated samples. Cycling experiments were performed galvanostatically in a standard laboratory cell.

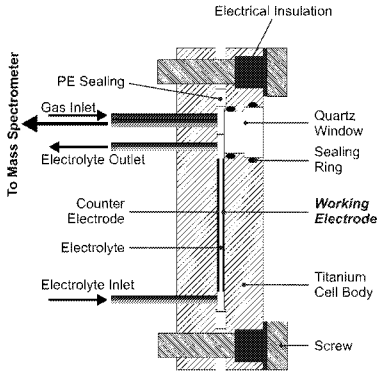

Fig. 1: Schematic view of the new DEMS cell.

3 RESULTS

By SEM, it was possible to observe the SEI formation on the surface of positive electrodes. Figure 2 shows a *post mortem* image of the electrode surface. After stabilization at 4.3 V vs. Li/Li^+, a pronounced film is visible, presumably formed by the polymerisation of the additive used, vinylene carbonate (VC). DEMS allows to follow the CO_2 gas evolution during the cycling of metal oxide electrodes. Comparing the rate and the onset potential of the CO_2 gassing, it was proved that with the addition of VC the gas formation between 3 V and 4.3 V can be significantly reduced. Figure 3 shows a typical DEMS measurement of $LiCoO_2$ with VC where the CO_2 evolution is starting at ca. 4.7 V. This is likely because the protective film created by VC is already formed at lower potentials. The relatively high CO_2 formation rate above that potential could have its origin in the oxidative decomposition of the polymeric SEI. With galvanostatic long time cycling experiments the cycle stability of the positive electrode was investigated. The diagram in Figure 4 demonstrates that by adding 2 % VC the cycle stability can be considerably improved. The increase of the irreversible charge was negligible.

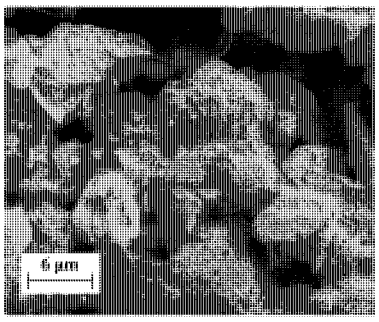

Fig. 2: SEM image of a $LiCoO_2$ electrode, electrolyte EC/PC 1:1 + 2 % VC, 1M $LiPF_6$.

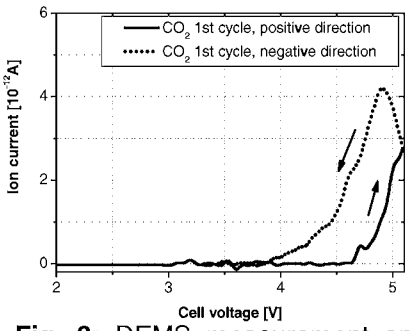

Fig. 3: DEMS measurement on $LiCoO_2$, electrolyte EC/DMC 1:1 + 2 % VC, 1M $LiPF_6$.

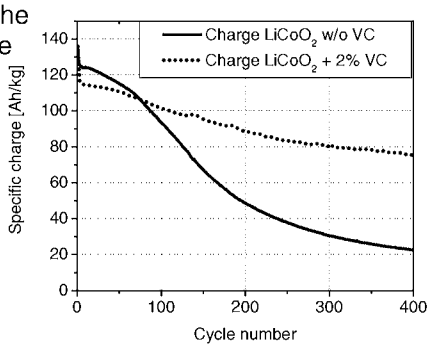

Fig. 4: Cycle stability of $LiCoO_2$, electrolyte EC/PC 1:1, 1M $LiPF_6$ with and without additive.

4 ACKNOWLEDGEMENTS

The financial support of the Swiss National Science Foundation as well as the Swiss Federal Office of Education and Science (CAMELIA Project) is gratefully acknowledged.

SEI FILM FORMATION ON HIGHLY CRYSTALLINE GRAPHITIC MATERIALS IN LITHIUM-ION BATTERIES

H. Buqa, A. Würsig, M.E. Spahr (TIMCAL SA), F. Krumeich (ETH Zürich), P. Novák

The solid electrolyte interphase (SEI) layer, i.e. the passivation layer formed on the surface of the carbonaceous negative electrode material, is the key component in the negative electrode, determining electrochemical performance and safety of the whole lithium-ion battery. In situ differential electrochemical mass spectrometry (DEMS) and post mortem scanning electron microscopy (SEM) studies were used to study the SEI film formation at a highly crystalline TIMREX® SLX50 graphite negative electrode during the first electrochemical lithium insertion using 1 M $LiPF_6$ in ethylene carbonate (EC) with either dimethyl carbonate (DMC) or propylene carbonate (PC) as co-solvent.

1 INTRODUCTION

In lithium-ion batteries with either liquid or gelled polymer electrolytes, a passivating layer called the Solid Electrolyte Interphase (SEI) [1,2] is formed during the first charge. The SEI layer suppresses, if the film forming process is optimised, any further electrolyte decomposition and prevents the exfoliation of the graphite structure. At the same time, it allows the passage of lithium ions. However, the mechanism of its formation is rather complex and not yet completely understood.

In used standard electrolytes such as 1 M $LiPF_6$ in EC/DMC, the irreversible charge loss occurring during the first reduction is low and depends linearly on the specific BET surface area of the graphite material used [2]. Unfortunately many graphite-based negative materials are not able to intercalate lithium ions reversibly in propylene carbonate (PC) based electrolytes. It is known that most graphitic materials with high crystallinity show exfoliation during the first electrochemical insertion of lithium in propylene carbonate. This graphite exfoliation results in an enhanced irreversible charge loss and reduced cycling stability [3] and, thus, in battery failure. The graphite exfoliation can be avoided if propylene carbonate is replaced by its non-substituted cyclic carbonate homologue, ethylene carbonate. So, in the EC/PC, $LiPF_6$ mixture, striking differences can be observed in the SEI film formation depending on the type of graphite used.

The complex interaction between the graphite electrode and the electrolyte makes the analysis of the SEI layer highly challenging. We are confident that, by combining various *in situ* and *ex situ* techniques, a sufficient basic knowledge to understand these processes can be acquired. We employed different techniques as *in situ* DEMS and *post mortem* SEM along with classical electrochemical charge/discharge tests.

2 EXPERIMENTAL

As active anode material, TIMREX® SLX50 (TIMCAL SA, Bodio, Switzerland) graphite (specific BET surface area: 4.0 m^2/g) powder was used as received. Electrochemical behaviour of SLX50 graphite was investigated in half cells against lithium in 1 M $LiPF_6$ in EC/DMC (1:1) and EC/PC (1:1) mixtures, as described elsewhere [4].

Scanning electron microscopy (SEM) was performed on a LEO 1530 Gemini microscope, which was operated at low voltage (usually 1 kV) to achieve a suitable contrast of the surface details in the secondary electron images and to minimize charging of the uncoated samples.

In situ DEMS measurements were used to study the process of electrolyte decomposition and SEI formation, and to follow the formation of different gaseous reaction products on the graphite electrodes during the first electrochemical reduction. The DEMS setup has been described elsewhere [5].

3 RESULTS

Figure 1 shows the different electrochemical response of the first galvanostatic lithium insertion/de-insertion in TIMREX® SLX50 graphite in 1 M $LiPF_6$, EC/DMC 1/1 (w/w) and 1 M $LiPF_6$, EC/PC 1/1 (w/w) as electrolyte system.

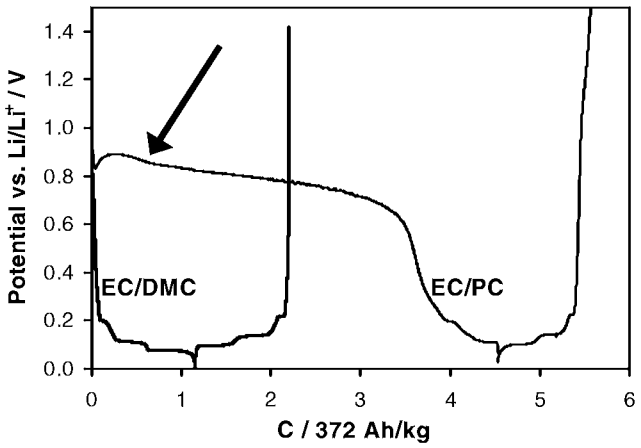

Fig. 1: First electrochemical intercalation/deintercalation of lithium into/from TIMREX® SLX50 in 1 M $LiPF_6$, EC/DMC 1/1 (w/w) and in 1 M $LiPF_6$, EC/PC 1/1 (w/w) as electrolyte at a specific current of 10 mA/g.

In EC/DMC, SLX50 graphite shows the typical insertion properties expected for a highly crystalline graphite material. A reversible capacity of about 360 mAh/g with a coulombic efficiency of 94 % could be observed at a specific current of 10 mA/g. In contrast, the higher reduction potential of ca. 0.9 V vs. Li/Li^+ and the very

large additional plateau observed in the case of the EC/PC electrolyte (see arrow in Figure 1) indicates that a different reduction mechanism occurs in this electrolyte and leads to graphite exfoliation [3]. Various factors directly and indirectly affect the potential of this additional plateau. Up to now, it was challenging to determine the parameters which influence this phenomenon.

From the electrochemical results we can clearly see that the SEI film formation depends on the electrolyte used. To further investigate the film formation behaviour on the graphite negative electrode in different electrolytes, we performed post mortem SEM studies of SLX50 graphite. The electrodes were galvanostatically charged to 0.3 V vs. Li/Li^+ and subsequently stabilised potentiostatically at this potential.

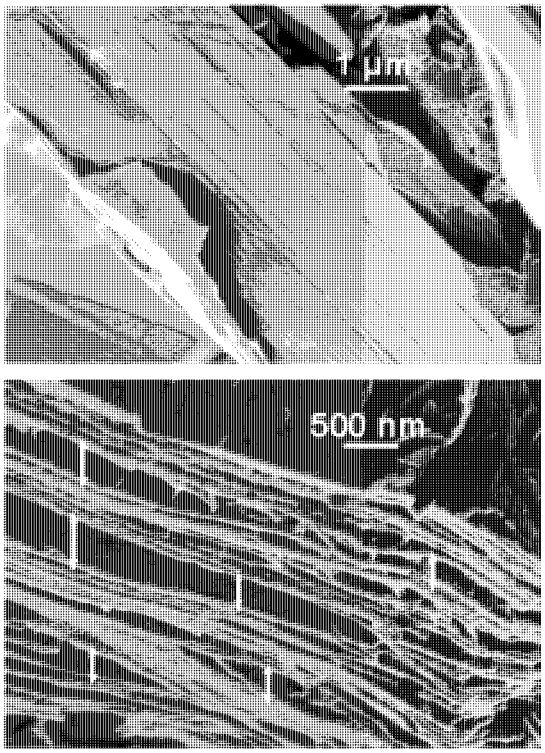

Fig. 2: (top) SEM image of TIMREX® SLX50 powder graphite material and (bottom) *post mortem* SEM image of a SLX50 graphite negative electrode in 1 M $LiPF_6$ in EC/PC 1/1 (w/w) as electrolyte.

Figure 2 (top) shows the SEM image of uncycled SLX50 graphite. The graphene layers are well ordered and compact densely packed, without expanded distances. Figure 2 (bottom) displays the effect of exfoliation of the same graphite electrochemically reduced in EC/PC. Some graphite particles reveal a partial exfoliation of the graphene layers manifested by gaps and holes at the graphite layer edges of the particles. In addition, some particles show a significant expansion of their dimensions (up to ~500 nm, see arrows). This observation supports the hypothesis that electrochemical graphite exfoliation is caused by the co-intercalation of solvents, along with the Li^+ ions, between the graphite layers during the film formation, followed by the decomposition of the solvent molecules (as suggested by Besenhard et al. [6]). No exfoliation of the graphene layers can be observed in the case of SLX50 electrodes stabilised in 1 M $LiPF_6$, EC/DMC electrolyte. A uniform SEI film is covering the entire graphite surface (not shown here).

In situ DEMS measurements were performed to investigate the consequences of the graphite exfoliation on the SEI formation. These gases were used to monitor the graphite passivation and film formation process. If 1 M $LiPF_6$, EC/PC was used as electrolyte; propylene gas could be detected by the mass spectrometry besides the formation of ethylene and hydrogen.

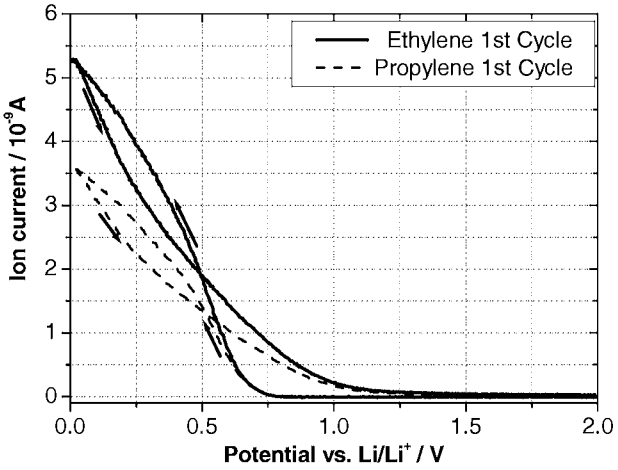

Fig. 3: DEMS measurements in TIMREX® SLX50 in 1 M $LiPF_6$, EC/PC 1/1 (w/w) electrolyte. Mass signals corresponding to ethylene (m/z=27) and propylene (m/z=41) are shown.

Both, the ethylene and propylene formation start at a similar potential of about 0.8 V vs. Li/Li^+ and increase until the potential of 0.01 V vs. Li/Li^+ is reached (Figure 3). This indicates that the formation of a stable passivation film was hindered. The gas formation can be observed even during the next cycles (not shown) between 0.9 V and 0.01 V vs. Li/Li^+ indicating, thus, that the passivation film is still not complete. The gas formation at the graphite electrode during the first reduction in the EC/PC electrolyte significantly differs to the EC/DMC electrolyte system. Obviously, the decomposition products of solvated graphite intercalation compounds formed upon the reduction in EC/PC electrolytes are not able to form an effective SEI. This provides space for further solvent co-intercalation and the electrochemical exfoliation of the graphite.

4 REFERENCES

[1] E. Peled, J. Electrochem. Soc. **12**, 2047 (1979).

[2] M. Winter, J.O. Besenhard, M.E. Spahr, P. Novák, Adv. Mater. **10**, 725 (1998).

[3] D. Aurbach, B. Markovsky, A. Shechter, Y. Ein-Eli, H. Cohen, J. Electrochem. Soc. **143**, 3809 (1996).

[4] H. Buqa, D. Goers, L. Hardwick, M. E Spahr, P. Novák, PSI Scientific Report **V**, 2002, 63 (2003).

[5] R. Imhof, P. Novák, J. Electrochem. Soc. **145** 1081 (1998).

[6] J.O. Besenhard, M. Winter, J. Yang, W. Biberacher, J. Power Sources **54**, 228 (1995).

THE EVOLUTION OF GAS IN PC CONTAINING BATTERY ELECTROLYTE

J. Ufheil, A. Würsig, P. Novák

In situ differential electrochemical mass spectrometry (DEMS) and in situ subtractively normalised interfacial Fourier transform infrared spectroscopy (SNIFTIRS) were used to study the reductive decomposition products of propylene carbonate (PC) containing battery electrolyte at metal oxide electrodes. Depending on a large number of parameters like e.g. (i) electrolyte composition, (ii) type and surface of the metal oxide and (iii) the electrochemical conditions, hydrogen, carbon dioxide, ethane, ethene, propane and propene were evolved during electrolyte decomposition. In some cases additional signals were detected which could indicate the evolution of acetone.

1 INTRODUCTION

Rapid progress in the portable electronics industry has led to a large increase in the demand for portable power sources. Lithium secondary batteries continue to be the superior choice with respect to weight and power requirements. The system comprises of a lithium transition metal oxide as the cathode and a carbonaceous material as the anode, divided by an organic electrolyte and separator. The cathode material is one of the important factors in determining the final cost, weight and efficiency of the battery. Many studies on cathode materials have been reported during the last years. Amongst these studies, *in situ* methods like DEMS and SNIFTIRS have provided valuable information about electrolyte decomposition and formation of the SEI. Our present work describes our investigations of gas evolution at different metal oxides in respect to possible evolution of acetone.

2 EXPERIMENTAL

Metal oxide electrodes were prepared from a slurry containing the metal oxide, Oppanol (B200, BASF AG, Germany), graphite (MB15, TIMCAL Ltd, Switzerland) and carbon black (Ensaco® 250, TIMCAL Ltd, Switzerland) with a mass ratio of 91:5:9:1. Petrol ether was used as the liquid. After stirring with a turbo stirrer the slurry was doctor bladed to a thickness of 350 µm directly onto the current collector body of the DEMS cell and dried for 12 h at 120°C under vacuum.

DEMS tests were performed in a half cell with lithium metal as negative electrode (reference and counter electrode) and metal oxide as positive electrode (working electrode). The measurement system is based on headspace analyses. A schematic drawing of our DEMS setup has been published elsewhere [1]. The gaseous reaction products are pumped off continuously from the top of the electrochemical cell via a capillary into a quadrupole mass spectrometer where they are analysed *on line*.

In situ ATR-SNIFTIRS experiments were performed with a 12 mm diameter polished nickel disc as a working electrode and a Li strip as counter and reference electrode. The SNIFTIRS cell was dried, assembled, filled with electrolyte, and hermetically sealed in the glove box before adjusting it in the FTIR instrument. Spectra were measured with a resolution of 4 cm^{-1} by accumulating 40 scans with a Perkin-Elmer 2000 Fourier transform infrared (FTIR) spectrometer equipped with a DTGS detector. A reference spectrum R_0 was measured at open circuit potential (OCP). The potential was successively decreased in steps of 0.2 or 0.3 V, respectively, with an equilibration time of four minutes at each potential. During each equilibration, one spectrum R_E was measured at the potential E. The potential-dependent changes at the electrode/electrolyte interface in the thin electrolyte layer between the electrode and the optical window were visualised by plotting R_E/R_0.

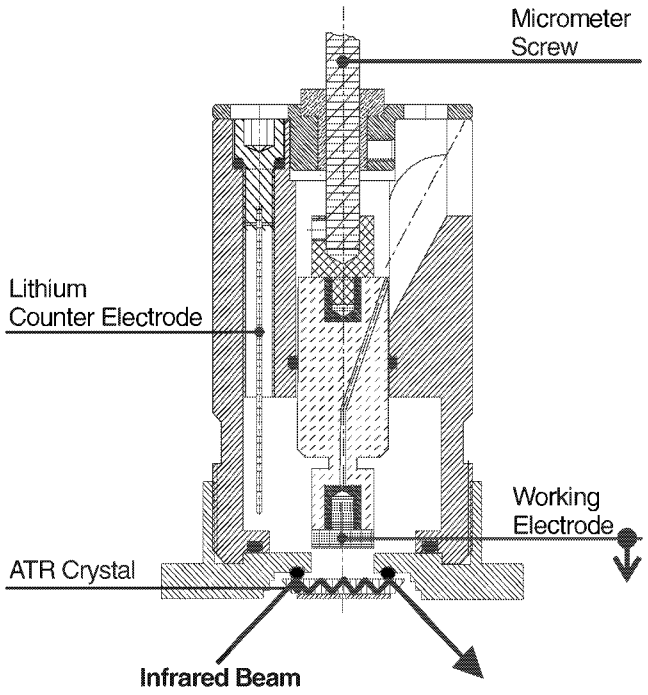

Fig. 1: Schematic of the ATR-SNIFTIRS cell used. The internal reflection element (ZnSe) allows up to six reflections.

3 RESULTS

Figure 2 (I) shows the ATR-SNIFTIRS spectrum at 5 V of PC with 1 M $LiClO_4$. Positive-going and negative-going bands represent a decrease or increase, respectively, in the concentration of species at the electrode or in the thin electrolyte layer between the electrode and the optical window. The spectra reveal several decomposition products during oxidation, e.g. carbon dioxide at 2341 cm^{-1}. However, we were not able to attribute the observed bands, in particular at 1770 cm^{-1} to known compounds like ethane, ethene, propane and propene which were detected by DEMS. For this we assigned most of the negative going-

bands to SEI formation products. Interestingly, the IR spectrum of acetone (III) in combination with the spectrum of PC (II) nearby matches the spectrum. Indeed, acetone can be considered as a decomposition product of PC (Figure 3).

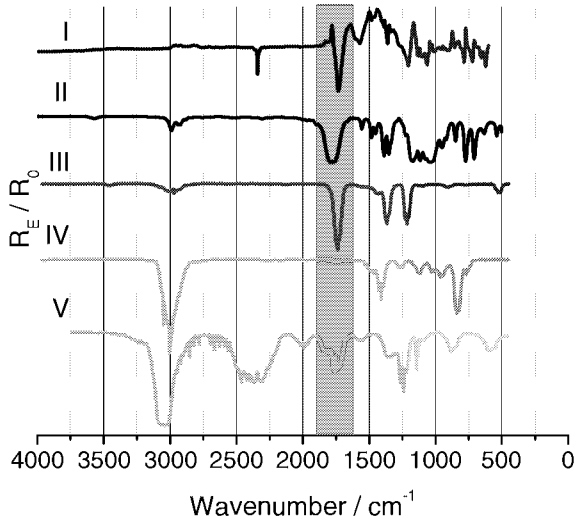

Fig. 2: SNIFTIR spectra measured on a polished nickel electrode in the electrolyte (I) 1 M $LiClO_4$ in PC at 5 V vs. Li/Li$^+$, IR-spectra of PC (II), acetone (III), propylene oxide (IV) and propanal (V).

To confirm the hypothesis we attempted to identify the evolved gases in DEMS experiments. The identification is complicated because of the overlapping of the mass spectra of the gas mixture, in which a number of products share the same mass numbers.

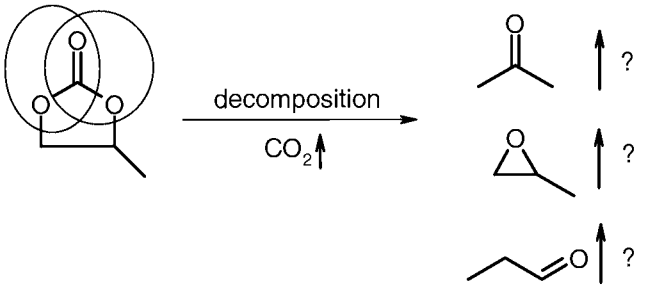

Fig. 3: Possible products of propylene carbonate decomposition.

Figure 4 shows the mass spectra of acetone which is similar to propylene oxide or propanal. For the DEMS measurements mass numbers were chosen allowing to exclude or include possible gas decomposition components. The obtained results are shown in Figure 5. Obviously, ion currents are potential dependent for certain mass numbers.

The first components to be excluded are ethylene and propylene carbonate. Both are electrolyte components present in the cell. We therefore expect a potential independent signal. The obtained signals show a clear dependence on the potential. Consequently we can be sure that the mass signal is coming from products of electrochemical decomposition. In addition, for mass number 58 we detected an unambiguous potential dependent signal. There the intensity for ethylene and propylene carbonate fragment is low but for acetone high. The signal at mass number 58 also excludes ethane, ethene, propane and propene. Signals of these components are expected at mass units 43, 42, 41 and 15. They obviously overlap with the acetone signal, because the acetone mass spectrum shares most of its mass numbers with propane and propene.

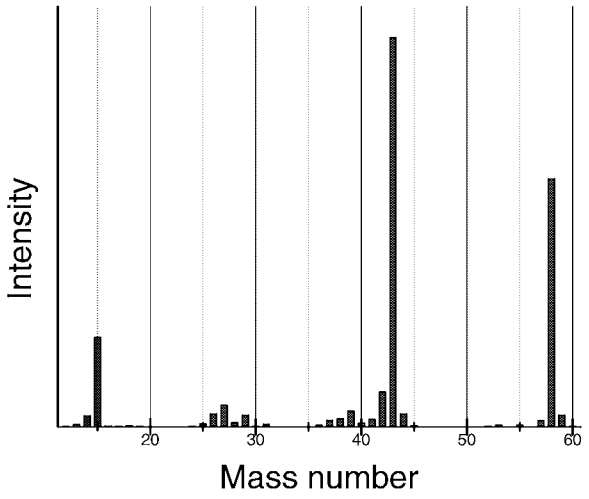

Fig. 4: Mass spectrum of acetone. Prominent mass numbers are 15, 43 and 58.

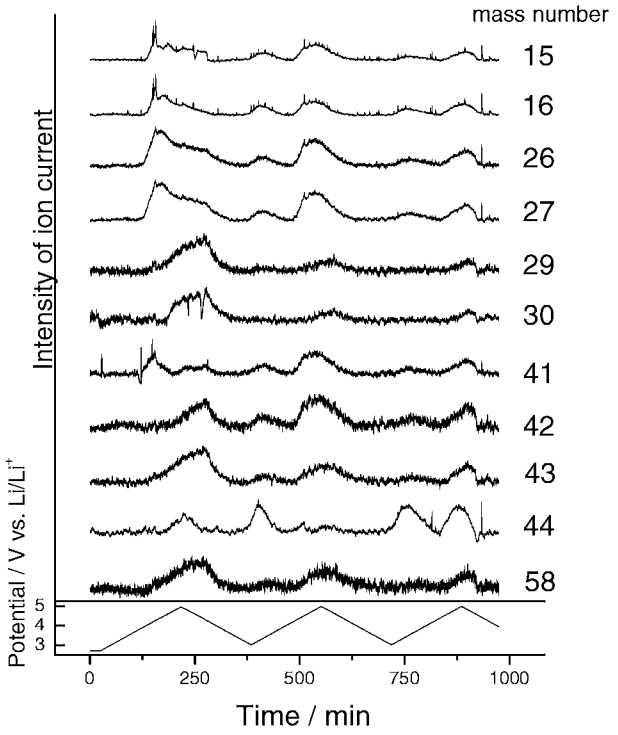

Fig. 5: Intensity of the ion currents at the investigated mass numbers in dependence on the applied potential. For a better illustration strong signals (e.g. 44) were scaled.

In conclusion, the combination of mass spectra and SNIFTIR spectra could point to the possible generation of acetone in PC containing battery electrolyte.

4 REFERENCE

[1] P. Novák, D. Goers, L. Hardwick, M. Holzapfel, W. Scheifele, J. Ufheil, A. Würsig, *Advanced In Situ Characterization Methods Applied to Carbonaceous Materials,* J. Power Sources, in press (2005).

STABLE CYCLING OF GRAPHITE IN AN IONIC LIQUID BASED ELECTROLYTE

M. Holzapfel, C. Jost (Degussa), P. Novák

1-Ethyl-3-methylimidazolium-bis(trifluormethylsulfonyl)-imide (EMI-TFSI) has been shown to reversibly permit lithium intercalation into standard graphite when vinylene carbonate is used in small amounts as additive.

1 INTRODUCTION

Ionic liquids [1] have been attracting interest for lithium and lithium-ion batteries, as they show a relatively large electrochemical along with a high thermal stability and they possess a high conductivity. They show a much reduced flammability and a nearly non-existing vapour pressure even at elevated temperatures. In general they are not environmentally hazardous.

Early attempts to cycle lithium-ion batteries using electrolytes on the basis of ionic liquids have failed. The reason is that electrolyte reduction occurs at the low potential at which the intercalation of lithium into the graphite proceeds. One exception are systems based on aluminium chloride. However, these are difficult to prepare and are toxic due to $AlCl_3$ [2]. Only recently a partial lithium intercalation into graphite was obtained in $AlCl_3$-free systems but with only poor yield and only between 5-10 cycles [3,4]. We present here the results we have obtained on the highly reversible and stable cycling of graphite electrodes in a vinylene carbonate containing electrolyte, based on 1-ethyl-3-methylimidazolium-bis(trifluormethylsulfonyl)-imide.

2 EXPERIMENTAL

The EMI-TFSI used has been dried under vacuum at 120°C for 8h prior to use and contained less than 20 ppm water. The graphite used was TIMREX SFG44 (TIMCAL SA, Bodio), $Li_4Ti_5O_{12}$ was used as counter electrode. Cycling of the graphite material was done with 10 mA/g during the first cycle and 50 mA/g during the subsequent cycles. At the end of the galvanostatic step a potentiostatic step followed until the current dropped below 5 mA/g. Scanning electron microscopy was performed on a LEO 1530 Gemini microscope.

3 RESULTS

Figure 1 shows the results of the cycling experiments of an SFG44 electrode in the electrolyte EMI-TFSI – 1M $LiPF_6$ with 5% VC. The feasibility of the cycling of graphite is clearly shown. No fading is evident for up to 150 cycles, only a small capacity loss between the charge and discharge is observed (1.5-2%). To our best knowledge, this is the first time that graphite electrodes have been cycled in a stable manner in an ionic liquid based electrolyte. The irreversible capacity is slightly increased when compared to the classical electrolyte EC:DMC (1:1) – 1M $LiPF_6$, where it is of the order of 0.2%. For lower concentrations of VC (2%) the capacity loss per cycle is higher (4%) and the reversible capacity lower (around 300 mAh/g). This shows that the film formed under these conditions is not yet fully stable. For only 1% of VC, cycling of graphite is no longer possible. Indeed, scanning electron microscopy (Figure 2) shows that a homogeneous thin protective film is formed in the case of the 5% VC-containing electrolyte. However, loose aggregates of reduction products together with uncovered graphite particles (arrow) are found in the case of the VC-free electrolyte. This is, to our best knowledge, the first time that a passivation film on graphite has been identified in an ionic liquid electrolyte.

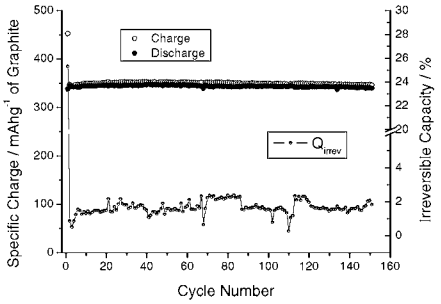

Fig. 1: Stable cycling of a SFG44 in EMI-TFSI – 1M $LiPF_6$– 5%VC.

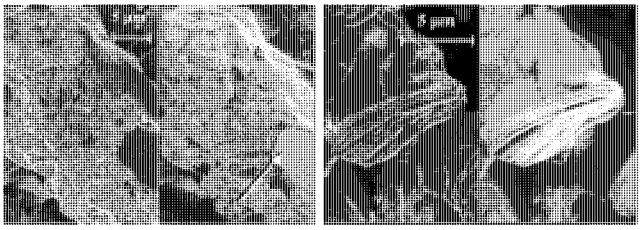

Fig. 2 SEM micrographs of SFG44 electrodes after stabilisation at 300 mV vs. Li/Li^+ in EMI-TFSI - 1M $LiPF_6$ without (left) and with 5% VC (right). In both cases the right hand images have been made in the surface sensitive secondary electron mode.

4 ACKNOWLEDGEMENT

The authors would like to express their gratitude to Dr. Frank Krumeich (ETH Zürich) for the acquisition of the scanning electron micrographs.

5 REFERENCES

[1] P. Wasserscheid, T. Welton, *Ionic Liquids in Synthesis*, Wiley-VCH, Weinheim (2003).

[2] J. Fuller, R. A. Osteryoung, R. T. Carlin, J. Electrochem. Soc. **142**, 3632 (1995).

[3] H. Sakaebe, H. Matsumoto, Electrochem. Commun. **5**, 594 (2003).

[4] Y. Katayama, M. Yukumoto, T. Miura, Electrochem. Solid State Lett. **6**, A96 (2003).

INVESTIGATIONS ON THE INFLUENCE OF ELECTROLYTE CO-SOLVENT CHAIN BRANCHING ON LITHIUM-ION BATTERY PERFORMANCE

J. Vetter, H. Buqa, P. Novák

Lithium ion battery electrolytes containing three different isomers of butyl methyl carbonate were investigated in order to determine the influence of co-solvent chain branching on the electrochemical performance. The reversible capacity obtained in SFG44 graphite (TIMCAL Ltd.) half-cells is higher for electrolytes with branched co-solvents and increases as the chain branching gets closer to the carbonate group. The long-term cycling stability, investigated in SLP30 graphite (TIMCAL Ltd.) half-cells, shows the same trend.

1 INTRODUCTION

Organic carbonates are widely used as solvents in state-of-the-art lithium-ion batteries. Since battery performance is determined to a major part by the film-forming solvent component and the electrolyte salt, so far little attention has been paid to the co-solvent. In a recent publication [1] we proved the suitability of n-alkyl methyl carbonates as co-solvents. To investigate the influence of chain branching on cell performance, we chose isomers of n-butyl methyl carbonate (n-BMC), i.e. *iso*-butyl methyl carbonate (*i*BMC) and *sec*-butyl methyl carbonate (*s*BMC).

2 EXPERIMENTAL

Electrochemical cycling experiments were performed using 1*M* $LiPF_6$ solutions in different solvent mixtures. Two types of graphite were used as the working electrode with metallic Li as the counter and reference electrode. The cycling experiments were performed at 25°C under strict temperature control at a charge/discharge rate of C/5 (1st cycle: C/30). Complete Li intercalation was ensured by applying a CCCV procedure.

3 RESULTS AND DISCUSSION

In half cells with TIMREX® SFG44 graphite and ethylene carbonate / dimethyl carbonate (EC/DMC), 1*M* $LiPF_6$ electrolytes, usually a reversible capacity of ca. 340 Ah/kg (of carbon) is observed instead of the theoretical maximum value of 372 Ah/kg. If DMC is substituted by the BMC isomers, a reversible capacity of 350 – 360 Ah/kg can be achieved, showing that the electrolyte has a significant impact. The most probable interaction pathway of the electrolyte is by influencing the properties of the solid electrolyte interphase (SEI), a protective layer formed on graphite during the initial cycles. As can be seen from Figure 1, the reversible (specific) capacity increases in the series DMC < *i*BMC < BMC ≈ *s*BMC. This holds true for both 1:1 and 1:2 mixtures with EC.

Differences in the SEI should also impact on cyclability. To estimate the long-term behaviour of cells with the BMC isomers, TIMREX® SLP30 graphite was used instead of SFG44. With this more challenging electrode material, the effects of chain branching on cyclability become more obvious. Using electrolytes with BMC isomers, the cycling stability of SLP30 could be significantly improved. As can be seen from Figure 2, for 1:2 mixtures with EC the cycling stability increases in the row *i*BMC < BMC < *s*BMC and, in the case of *s*BMC even outperforms the reference EC/DMC 1:1. The comparison is given in both absolute values and values relative to the 2nd cycle to rule out weighing errors.

Chain branching of the electrolyte co-solvent influences both reversible capacity and long-term cycling behaviour. The mechanism is not clear yet, but the most probable pathway is via the SEI. Chain branching close to the carbonate group (as in *s*BMC) has a positive effect on reversible capacity and fading. The influence of chain branching at a site remote from the carbonate group (as in *i*BMC) is weaker and seems to vary with different types of graphite.

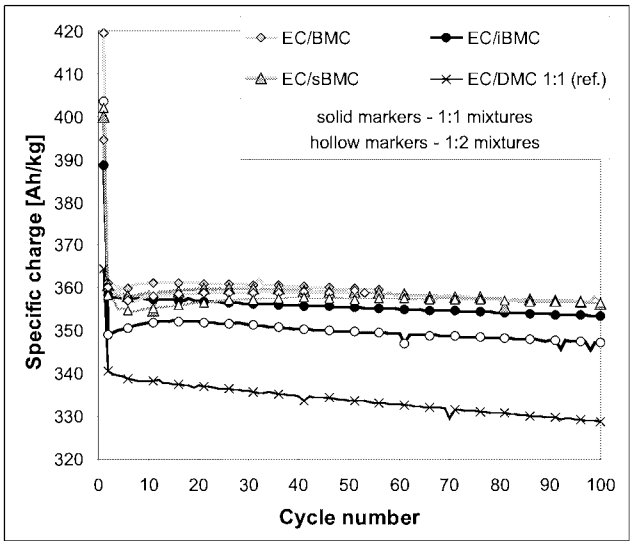

Fig. 1: Specific charge capacity (Li intercalation) in SFG44 half cells vs. metallic Li with isomeric BMC electrolytes containing 1*M* $LiPF_6$.

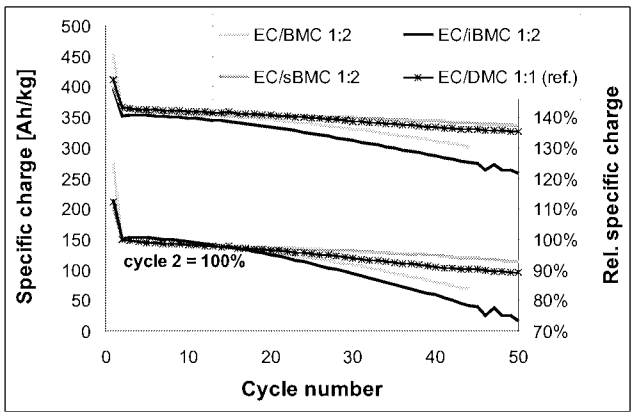

Fig. 2: Relative (bottom) and absolute (top) cycling behaviour (Li intercalation) in SLP30 half cells vs. met. Li with isomeric BMC electrolytes containing 1*M* $LiPF_6$.

4 REFERENCE

[1] J. Vetter, P. Novak, J. Power Sources **119-121**, 338-342 (2003).

STATUS OF THE INFRARED BEAMLINE "X01DC" AT THE SLS

J. Wambach

The SLS Infrared Beamline will represent a state-of-the-art infrared source with a photon energy range covering the entire Infrared (IR) range. In the first stage two FTIR spectrometers will be available, which will be upgraded as soon as possible with IR microscopy and IR ellipsometry.

1 GENERAL

Infrared (IR) spectroscopy is widely applied and belongs to the main analytical techniques in chemistry, physics and biology. It bases on the excitation of discrete vibrational or rotational states by the absorption of radiation and is a non-destructive, easy-to-use method. Commonly used are Fourier Transform Infrared (FTIR) spectrometers.

The use of a synchrotron as IR radiation source offers several advantages. It represents a broadband source with high brightness (two to three orders of magnitude), and as non-thermal source the Boltzmann noise is well reduced. Synchrotron-based IR spectroscopy has allowed important breakthroughs in two areas, namely in the extension to the lowest energy range (the Far Infrared regime) and the study of extremely small samples. IR beamlines are realised or planned at several synchrotron facilities worldwide.

The SLS Infrared Beamline will represent a state-of-the-art IR source with a photon energy range covering the entire IR regime from the Far Infrared to the Near Infrared and partly up to the visible and UV regime (0.001 – ca. 5 eV, 1000– 0.20 μm, 10 - 45000 cm^{-1}).

2 THE IR RADIATION SOURCE

The IR beamline source will be the centre dipole magnet in the first triple bend achromat of the storage ring. The design makes use of radiation produced in the homogeneous field of the bending magnet. The top trace of Figure 1 shows the extracted flux.

3 THE BEAMLINE

The extraction mirror M1 is located directly downstream of the dipole magnet. Because of the high heat load, the mirror will be slotted allowing the hard radiation to pass on to an absorber. The mirror has a maximum acceptance of 61(H) x 39(V) $mrad^2$. The optical system will consist of three toroidal mirrors and one parabolic mirror as optical elements. In addition, several flat mirrors will be used. The total length of the beamline will be ca. 11 m.

Figure 1 shows a comparison of the extracted flux with the propagated flux at the last focal point F4 and inside the spectrometers. Only small losses in the propagated flux up to the spectrometer aperture at focal point F4 are observed. The relative large beam sizes at low energies give raise for losses after having passed the spectrometer aperture due to diffraction. The brightness of the beamline was calculated using an analytical function, which describes the source best (at low wavelength diffraction limited source; linearly decreasing effect with wavelength; at higher wavelengths increasing effect of the extended source). The result is displayed in Figure 2.

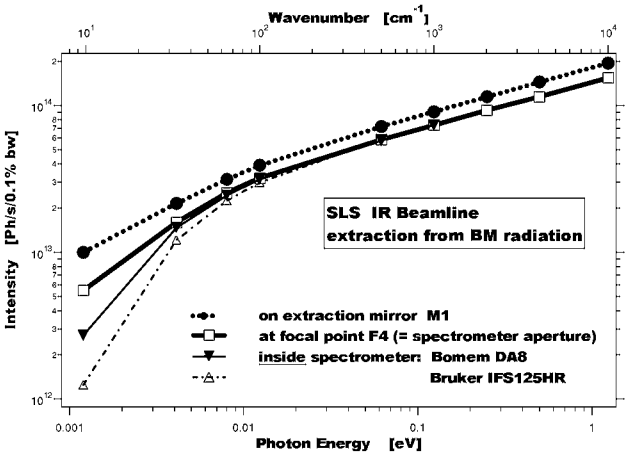

Fig. 1: Comparison of the extracted flux at the first mirror M1 (61(H) x 39(V) $mrad^2$) with that at focal point F4 and with the flux inside different spectrometers.

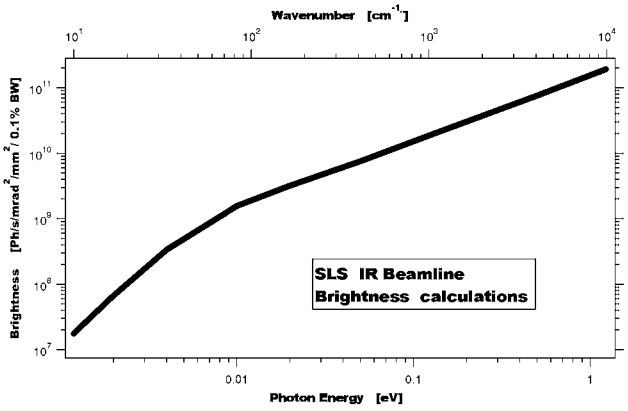

Fig. 2: The calculated brightness for the IR beamline.

4 END STATIONS

Three different FTIR spectrometers, two high resolving and one research-type spectrometer, will be available. The spectrometer will be upgraded with IR microscopes. User endstations or additional users equipment can be mounted easily at request.

5 TIME SCHEDULE

The beamline will be set-up in the next year, and user operation is envisioned to start in winter 2005.

HALL EFFECT CHARACTERIZATION OF THIN FILMS DEPOSITED BY LASER ABLATION

S. Canulescu, M. Montenegro, Th. Lippert, A. Wokaun

A series of $La_{0.6}Co_{0.4}CoO_3$, $La_{0.6}Co_{0.4}Mn_{0.9}Ni_{0.1}O_3$, $La_{0.6}Co_{0.4}MnO_3$, $La_{0.6}Co_{0.4}MnO_3$ thin films were investigated by Hall effect measurements and Raman Spectroscopy. It was found that the manganese thin films have excelent magnetoresistive properties. The influence of the substrate on the electrical properties of the films was investigated.

1 INTRODUCTION

Transition metal oxides with perovskite structures (ABO_3) such as $La_{1-x}Ca_xMnO_3$ and doped compounds have attracted a much attention due their colosal magnetoresistance {CMR= [ρ(H)- ρ(0)]/ ρ(0)}, for which the electrical resistance changes more than one order of magnitude under the effect of an external magnetic field. Recently, a Pulsed Reactive Crossed Beam Laser Ablation (PRCLA) method was successfully applied for the growth of thin films, such as $La_{0.6}Ca_{0.4}CoO_3$ [1].

2 EXPERIMENTAL

Perovskite thin films $La_{0.6}Ca_{0.4}CoO_3$, $La_{0.6}Ca_{0.4}Mn_{0.9}Ni_{0.1}O_3$, $La_{0.6}Co_{0.4}CoO_3$ $La_{0.6}Ca_{0.4}MnO_3$, with a thickness of 200 nm were prepared by a PRCLA method on different substrates, e.g MgO (111), MgO (110), $SrTiO_3$ (100), MgO (111), $LaAlO_3$ (100). The laser beam from a KrF excimer laser was used to induce ablation and this was synchronized with an N_2O gas pulse during the ablation process. The temperature- resistivity dependence curves were measured by the four-point method by cooling the samples from room temperature to liquid nitrogen temperature. The magnetoresistance was measured by applying a magnetic field of 0.5 T perpendicular to the film surface.

3 RESULTS AND DISCUSSION

The ρ(T) curves of LCMO films deposited at substrate temperatures of 650°C on $SrTiO_3$ and $LaAlO_3$ are shown in Figure 1.

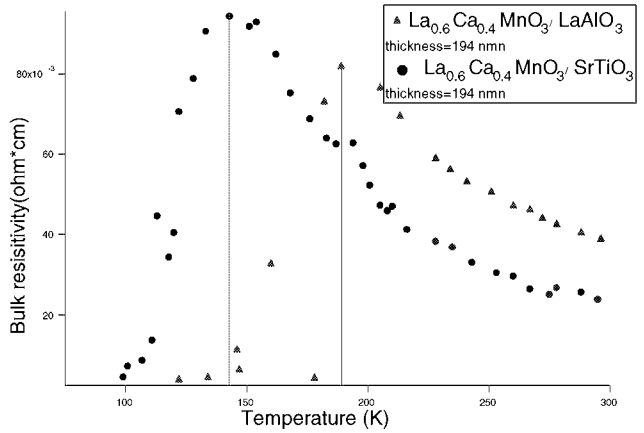

Fig. 1: Temperature dependences of the resistivity for LCMO thin films deposited on $SrTiO_3$ (left) and $LaAlO_3$ (right).

Both films exhibited a semiconductor to metal transition. The transition temperature point is higher for $LaAlO_3$ than $SrTiO_3$ substrates due to its different substrate-film lattice mismatch, which causes changes in the film microstructure and influences its electrical properties. Similar results for the transition temperature shift have been reported in the literature [2]. The maximum magnetoresistance value was 250 for LCMO/ $LaAlO_3$ and 1400 for LCMO/$SrTiO_3$. The point of the maximum CMR value coincides with the temperature transition point.

The LCCO and LCMO doped with Fe exhibited a semiconductor behavior in the entired measured temperature range (77K- 300K).

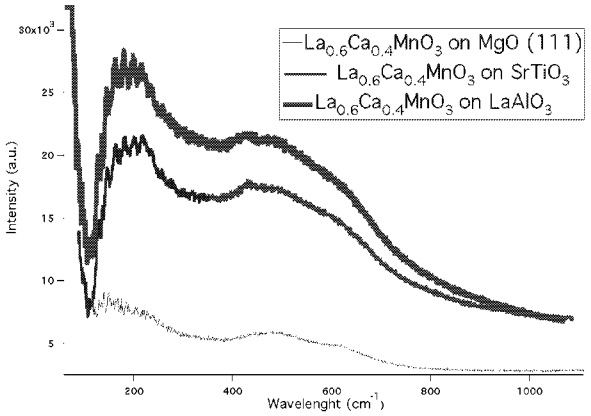

Fig. 2: Raman spectra of $La_{0.6}Co_{0.4}MnO_3$ thin films on $LaAlO_3$, $SrTiO_3$ and MgO substrates. Active vibrations at 425 cm^{-1} were recorded for the $LaAlO_3$ substrate and 437 cm^{-1} for the $SrTiO_3$ substrate.

Raman spectra recorded on the MgO substrate did not exhibit an obvious peak although a small shift was recorded between films deposited on $SrTiO_3$ and $LaAlO_3$ (Figure 2).

4 CONCLUSIONS

Electrical properties of LCCO and LCMO perovskite samples have been studied by Hall effect measurements and the lattice distorsions induced by different substrates were deduced from Raman spectroscopy. Further investigation will be performed to study surface morphology and crystallographic structures, in order to explain the effect of the strain and lattice mismatch on the growth and properties of CMR oxides.

5 REFERENCES

[1] M.J. Montenegro, M. Dobeli, T. Lippert, S. Muller, B. Schnyder, A. Weidenkaff, P.R. Willmott, A. Wokaun, Phys. Chem. Chem. Phys. **4**, 2799 (2002).

[2] C.J. Lu, Z.L. Wang, C. Kwon, Q.X. Jia, J. Appl. Phys. **88**, 4032 (2000).

GRAVIMETRIC AND PROFILOMETRIC MEASUREMENTS OF THE ABLATION RATES OF A PHOTOSENSITIVE POLYMER AT DIFFERENT IRRADIATION WAVELENGTHS

Th. Dumont, R. Bischofberger (applied microSWISS GmbH), T. Lippert, A. Wokaun

The ablation rates of a triazene polymer were studied by gravimetric (quartz micro balance) and profilometric (profilometer) methods after irradiation at irradiation wavelengths of 248 and 308 nm. The consistence of the two experimental methods is discussed for the ablation rates of the triazene polymer. The comparison of the gravimetric and the profilometric measurements suggests a significant mass removal, e.g. by formation of gaseous products, prior to the detection of changes in the surface morphology.

1 INTRODUCTION

Studies of the laser-induced decomposition or transformation of polymers with single pulses and laser fluences close to the threshold of ablation require very sensitive techniques, such as a quartz crystal microbalance (QMB), atomic force microscopy or profilometry. A mass loss (e.g. by QMB) due to photochemical reactions is expected for photosensitive polymers before a change in the surface morphology (e.g. by profilometry) can be measured. A triazene polymer (TP, see figure 1 for chemical structure) was studied gravimetrically and profilometrically after irradiation with fluences below and above the threshold of ablation at irradiation wavelengths of 248 and 308 nm.

2 RESULTS AND DISCUSSION

Figure 1 shows a comparison of the gravimetric and profilometric measurements of the ablation rates of TP at irradiation wavelengths of 308 and 248 nm for single pulse experiments. The ablation rates obtained with the QMB correlate quite well with the profileometer data. The removal rates for an irradiation wavelength of 248 nm (inset in Figure 1) measured with the profilometer are slightly higher relative to the data obtained by QMB at fluences above 80 mJ/cm^2. A possible explanation could be the carbonization of the polymer surface for higher fluences i.e. decomposition of the aromatic rings [1]. The carbonization is more pronounced at higher fluences. However, carbon reveals a higher density than the original polymer leading to a loss in volume without significant mass loss. Therefore, the craters are probably deeper when measured with the profilometer than calculated from the QMB data. The TP carbonization is more pronounced for shorter wavelengths (larger absorption of the aromatic system at shorter wavelengths). This could explain why this difference is not found at an irradiation wavelength of 308 nm. For fluences below 50 mJ/cm^2, profilometric measurements reveal a slightly lower ablation rate than calculated from the QMB data. This suggests that a mass loss, e.g. by formation of nitrogen from the photodecomposition of the triazene group or by evaporation of remaining solvent, occurs before change in the surface morphology of the polymer can be detected.

The ablation rates calculated for an irradiation wavelength of 308 nm, at high fluences, reveal a quite good agreement. For fluences below 45 mJ/cm^2 no significant ablation of the material could be measured by profilometry, which is also close to the reliable detection limit of this method. However, the data calculated from QMB exhibit clearly mass removal for fluences well below 45 mJ/cm^2. Again, this suggests, as expected for a photolabile material, the formation of gaseous products in the bulk and/or at the surface of the polymer prior to ablation.

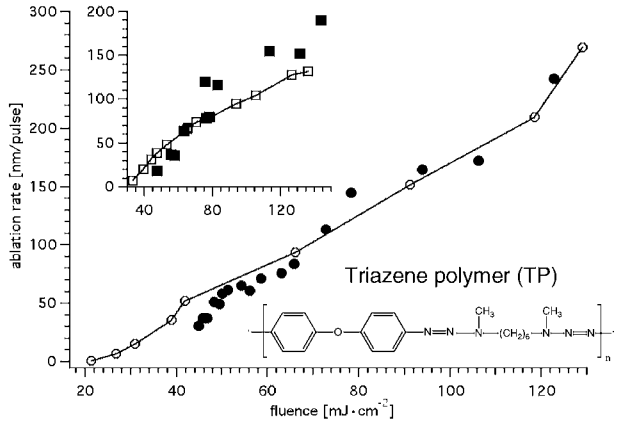

Fig. 1: Profilometric (●, ■) and gravimetric (○, □) measurement of the ablation rates of TP at irradiation wavelengths of 248 (■, □) and 308 nm (○,●).

3 CONCLUSION

A triazene polymer was irradiated at two different irradiation wavelengths (248 and 308 nm) and the ablation was studied using a Quartz microbalance and a profilometer. The comparison of the ablation rates obtained by both methods revealed a significant mass removal prior to ablation at irradiation wavelengths of 248 and 308 nm and a clear difference between the ablation rates obtained by the different methods. Partial carbonization of the material at the polymer surface, evaporation of the solvent and the formation of gaseous products may be the main reasons for this difference.

4 REFERENCE

[1] T. Lippert, T. Nakamura, H. Niino, A. Yabe, Macromolecules **29**, 6301-6309 (1996).

INVESTIGATION OF LASER-POLYMER INTERACTION BY TIME RESOLVED EMISSION SPECTROSCOPY

L. Urech, T. Lippert, A. Wokaun

The plasma emission properties of poly(vinyl chloride) (PVC), glycidyl azide polymer (GAP) and poly(vinyl nitrate) (PVN) have been investigated. The plasma temperature and electron density were calculated from the recorded spectra. For the energetic polymers (GAP and PVN) the plasma temperature decreased faster and had a higher maxiumum value. The fastest rate of decrease in the electron density was observed for GAP, whereas PVN and PVC had similar, but slower density reduction. For all polymers an increase in the plasma temperature within the first µs was observed.

1 INTRODUCTION

The influence of the decomposition properties on the emission spectra from three different polymers (Figure 1) after laser irradiation at 1064 nm was investigated under ambient conditions.

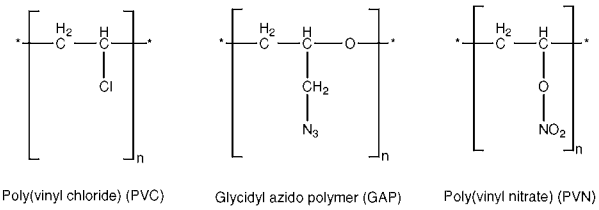

Fig. 1: Structure of PVC, GAP and PVN.

The polymers were doped with carbon nanopearls to achieve absorption at 1064 nm. All three polymers have similar decomposition temperatures, but GAP (-2053 J/g) and PVN (-3829 J/g) have significantly higher decomposition enthalpies than PVC (-418 J/g).

2 RESULTS AND DISCUSSION

All spectra shown in Figure 2 reveal the presence of diatomic (CN Violet, C_2 and CH) and atomic (H, Ca and Na) species. The atomic hydrogen is most probably formed during the fragmentation of the polymer, while Ca seems to be a common impurity in the carbon.

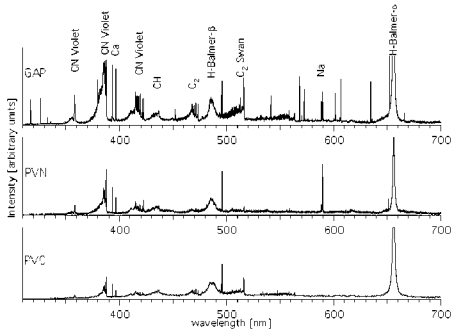

Fig. 2: Emission spectra of GAP, PVN and PVC, doped with carbon, 1 µs after irradiation at 1064 nm.

The CN Violet system in the PVC spectra must be created by the reaction of excited C species, derived from the polymer, with N_2 from the surrounding air [1]. The intensity of the peaks assigned to atomic species decayed much faster than that of the peaks assigned to molecular species, as shown in Figure 3. The H-Balmer-α line had almost dissapeared by 2 µs, whereas the CN Violet system could still be observed until 10 to 20 µs after the creation of the plasma even though the maximum intensities of these two lines were similar.

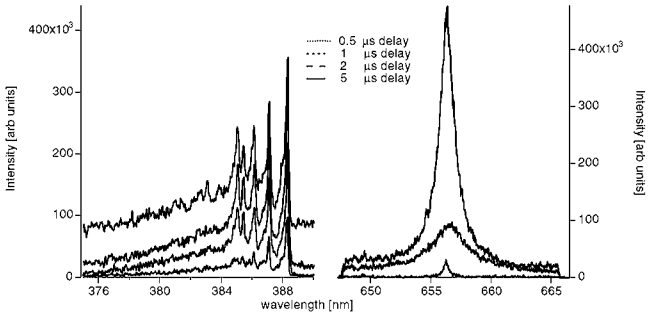

Fig. 3: Time dependent decay of the emission peaks of CN Violet (left) and H-Balmer-α (right).

The plasma temperatures were calculated by the simulation of the ro-vibrational spectra of the CN Violet system at 389 nm. The change in the plasma temperature with the delay time is shown in Figure 4a. The energetic polymers had a higher maximum plasma temperature than that of PVC, but they cooled much faster than the almost linear decrease in temperature observed for PVC. Higher laser fluences resulted not only in a lower maximum temperature, but also a slower cooling rate. For all polymers, an increase in the plasma temperature was observed during the first µs after irradiation.

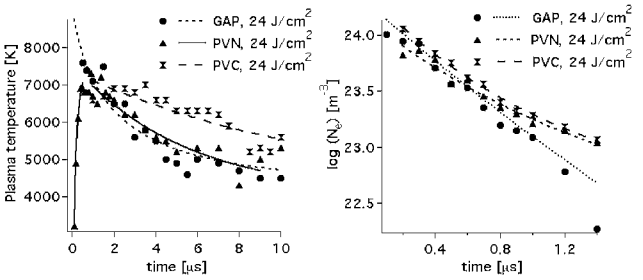

Fig. 4: The decay of the plasma temperature (a) and the electron density (b).

The initial electron density in the plasma was similar for all polymers (Figure 4b). The electron density of GAP decreased faster with delay time than that of PVN and PVC. Increasing the fluences did not influence the initial electron density, but did lead to a slower rate of density reduction. The decay of the electron density in the plasma took place in around 1 µs as did the increase of the plasma temperature.

3 REFERENCE

[1] S.S. Harilal, R.C. Issac, C.V. Bindhu, P. Gopinath, V.P.N. Nampoori, C.P.G. Vallabhan, Spectrochim. Acta A **53**, 1527-1536 (1997).

FABRICATION OF MICRO-OPTICAL COMPONENTS IN QUARTZ AND BaF_2

G. Kopitkovas, T. Lippert, C. David, J. Gobrecht, A. Wokaun

A one step micromachining process, which utilizes laser assisted chemical wet etching, was used to structure UV transparent dielectric materials. The threshold fluence, at which the etching starts, was well below the damage threshold fluence of these materials. The etch rate and the etch roughness of the quartz substrates strongly depended up on the laser fluence. An array of plano convex micro-lenses in quartz and a Fresnel lens in BaF_2 were fabricated by a combination of laser assisted chemical wet etching and projection of a diffractive mask. The array of micro-lenses in quartz was tested for its efficiency for homogenizing high power laser beams.

1 INTRODUCTION

One of the commercial applications of refractive and diffractive micro-lens arrays fabricated in UV transparent dielectric materials, such quartz or BaF_2, is high power laser beam homogenizing. A beam homogenizer consists of two optical components: an array of refractive micro-lenses and a plano convex field lens. The microlens array splits an incoming laser beam in to beamlets. A homogeneous laser beam is achieved at the target plane if it is located at the focal point of the field lens, where the beamlets overlap [1]. Refractive micro-lenses in quartz are fabricated commercially by using a complicated multi step process. An alternative technique for structuring of UV transparent dielectric materials was suggested by Niino et al. [2]. This *one step* process is known as *Laser Induced Backside Wet Etching* (LIBWE). For this method a highly absorbing organic liquid, such as a pyrene solution in acetone or tetrahydrofuran is used as the laser excitable etchant which is in contact with a quartz (or BaF_2) substrate. The laser irradiation passes through the quartz and is strongly absorbed by the solution. The rapid non-radiative relaxation of the excited pyrene molecules generates a temperature jump at the quartz–liquid interface. This fast temperature rise results in several effects, such as heating/melting of quartz as well as boiling and gasification of the solvent. Each of these effects are key elements in the etching process.

2 EXPERIMENTAL

A XeCl excimer laser (25 ns, 308 nm) was used as the irradiation source. The wet etching solution was pyrene in acetone or pyrene in tetrahydrofuran at a concentrations of 0.4 mol/l or 1.4 mol/l. The plano convex and Fresnel micro-lenses in UV transparent materials were fabricated by combining LIBWE and projection of Diffractive Grey Tone Phase Masks, as previously described [3].

3 RESULTS AND DISCUSSION

The etch rate of the quartz determined at various XeCl excimer laser fluences is shown in Figure 1. The threshold fluence above which etching starts is 0.7 J/cm^2, which is much lower than the damage threshold of quartz at this wavelength (20 J/cm^2). The etch rate in the low fluence range (marked as A in Figure 1) is influenced by the formation of carbon deposits,which strongly adhere to the quartz surface.

In the intermediate fluence range (marked as B in Figure 1) molten quartz is removed by a pressure jump, which is produced by the laser induced bubble collapse.

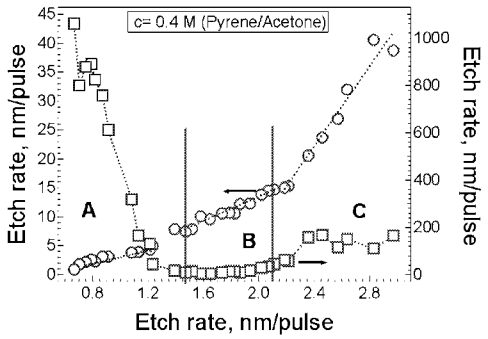

Fig. 1: Etch rate of quartz at different laser fluences.

At higher laser fluences (marked as C in Figure 1) the etching is most probably influenced by a plasma induced process. The lowest etch roughness (≤ 20 nm) is obtained for the fluence range B. This fluence range was used for the fabrication of a plano-convex micro-lens array (shown in Figure 2a) in quartz and a Fresnel lens in BaF_2 (shown in Figure 2b).

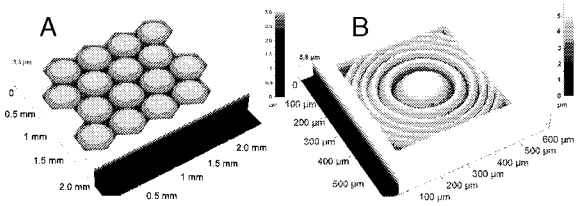

Fig. 2: Image of a plano-convex micro-lens array in quartz (A) and a Fresnel lens in BaF_2 (B)

Arrays of plano-convex micro-lenses have been successfully tested for their ability to homogenize Nd:YAG and excimer laser beams [4].

4 REFERENCES

[1] F.M. Dickey, S.C. Holswade, *Laser beam shaping*, M. Dekker, Inc. (2004).

[2] J. Wang, H. Niino, A. Yabe, Appl. Phys. A **68**, 111-113 (1999).

[3] G. Kopitkovas, T. Lippert, C. David, A. Wokaun, J. Gobrecht, Microelectron. Eng. **67-68**, 428-444 (2003).

[4] G. Kopitkovas, T. Lippert, C. David, S. Canulescu, A. Wokaun, J. Gobrecht, J. Photochem & Photobiol A **166**, 135-140 (2004).

SCIENTIFIC CONTRIBUTIONS FROM THE ELECTROCHEMISTRY LABORATORY FOR THE PSI SCIENTIFIC REPORT 2004, VOLUME VII, SYNCHROTRON RADIATION / MICRO- AND NANOTECHNOLOGY

ISSN 1660-4709

Please note that the following page numbers refer to the original page numbers in the PSI Scientific Report 2004, Volume VII, Synchrotron Radiation / Micro- and Nanotechnology, ISSN 1660-4709

Please cite the following contributions as indicated:

Author, Title, ISSN No., page

For example:

J. Wambach, J. Schneider, Q. Chen, H. Bächli, L. Schulz, R. Abela (PSI), R. Reiniger (Scientific Answers and Solutions, USA)
THE INFRARED BEAMLINE X01DC AT THE SLS
PSI Scientific Report 2004 / Volume VII, ISSN 1660-4709, p. 24

THE INFRARED BEAMLINE X01DC AT THE SLS

J. Wambach, J. Schneider, Q. Chen, H. Bächli, L. Schulz, R. Abela (PSI), and R. Reiniger (Scientific Answers and Solutions, USA)

The SLS Infrared Beamline will represent a bending-magnet-radiation-based, state-of-the-art infrared source with a photon energy range covering the entire infrared (IR) range. Three FTIR spectrometers will be available and will be upgraded as soon as possible with IR microscopes and an IR ellipsometer.

1. GENERAL

Infrared (IR) spectroscopy is widely applied and is a major analytical technique in chemistry, physics, medicine and biology. It is a non-destructive, easy-to-use method based on the excitation of discrete vibrational or rotational states by the absorption of radiation. Fourier transform infrared (FTIR) spectrometers are commonly used.

The use of a synchrotron as an IR radiation source offers several advantages. It is a broadband source with high brightness (two to three orders of magnitude higher than a laboratory source), and as a non-thermal source its Boltzmann noise is well reduced. Synchrotron-based IR spectroscopy has allowed important breakthroughs in two areas, namely in the extension to the lowest energy range (the far infrared regime) and to the study of extremely small samples. IR beamlines are realised or planned at several synchrotron facilities worldwide.

The SLS infrared beamline will represent a state-of-the-art IR source with a photon energy range covering the entire IR regime from the far infrared to the near infrared and partly up to the visible and UV regime (0.001 – ca. 5 eV, 1000 – 0.20 μm, 10 – 45000 cm^{-1}).

2. THE IR RADIATION SOURCE

The source of the IR beamline will be the center dipole magnet "BX01" in the first TBA (triple bend achromat) sector of the storage ring. The design makes use of radiation produced in the homogeneous field of the bending magnet (BMR, see Fig. 1). The calculated extractable IR flux is given by the bold trace in Fig. 2. For comparison the extracted flux from other synchrotron IR beamlines is displayed.

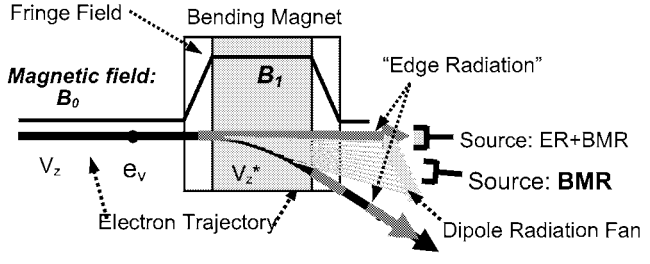

Fig. 1: Sketch of the two possible IR radiation sources: the bending magnet radiation (BMR) and the edge radiation (ER). The latter is always accompanied by some BMR.

Another possible IR radiation source, the radiation produced in the edge (or fringe) field of a bending magnet, the so-called edge radiation (ER) was studied in addition. The ER emits a factor two higher intensity (top trace with circles in Fig. 2), but has a more complicated structure and is always accompanied by some BMR. Besides the flux advantage, the ER exhibited two major disadvantages, namely a) it cannot be focused sufficiently, especially in the FIR regime (see the comparison in Fig. 3), and b) the centre of the focused intensity is moving with the wavelength. These facts suggest the use of the bending magnet radiation as the preferred source.

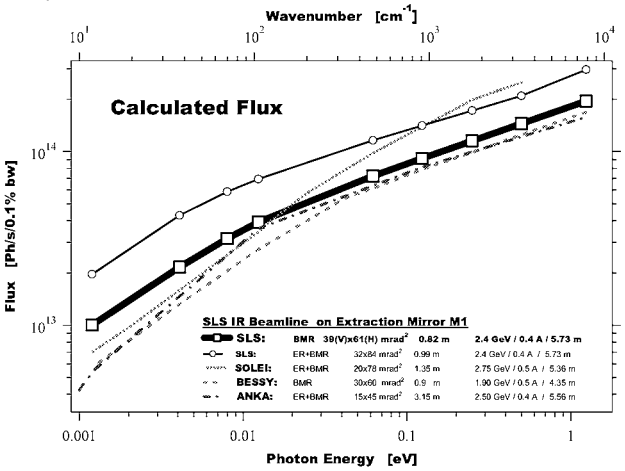

Fig. 2: Extracted IR radiation flux from the SLS ring by sole BM Radiation (squares) and ER+BM Radiation (circles) for several photon energies. The values were calculated on the position of the extraction mirror M1. For comparison the extracted flux from other beamlines are displayed (dashed lines).

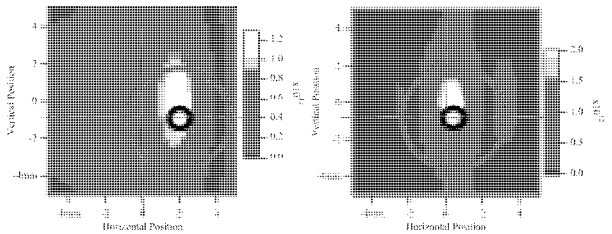

Fig. 3: Intensity distribution (photons/sec) for a photon energy of 4.09 meV (300 μm, 33 cm^{-1}) at the last focal point F4, where the spectrometers expects the focused beam. Left: Edge+BM radiation. Right: BM radiation. The two circles represent an entrance aperture of 5 mm and 1 mm diameter, respectively.

3. THE BEAMLINE

The first ("extraction") mirror M1, positioned at 45° relative to the incident beam, is located directly down-

stream of the dipole magnet at about 0.8 m distance from the source point. Because of the high heat load (max. circa 220 W/mm^2), the mirror will be slotted, allowing the hard radiation to pass on to an absorber. In addition, the mirror will be water cooled.

Mirror M1 will reflect the extracted radiation with a maximum acceptance of 61 mrad (H) x 39 mrad (V) upwards out of the plane of the synchrotron. The optical system will consist of three toroidal mirrors (M2T, M5T, M6T) as optical elements and several flat mirrors (M1, M3, M4, M7, M8). Mirror M6T will be movable and direct the light to one of the three FTIR spectrometers. In addition, three parabolic mirrors (M9P-a, M9P-b, M9P-c) will be used to match the incident IR beam to the angular acceptance of the interferometers.

At the first focal point F1, several IR transparent windows will be positioned, separating the synchrotron UHV from the HV in the rest of the beamline. The total length of the beamline will be ca. 11 m. A CAD drawing of the beamline is given in Fig. 4.

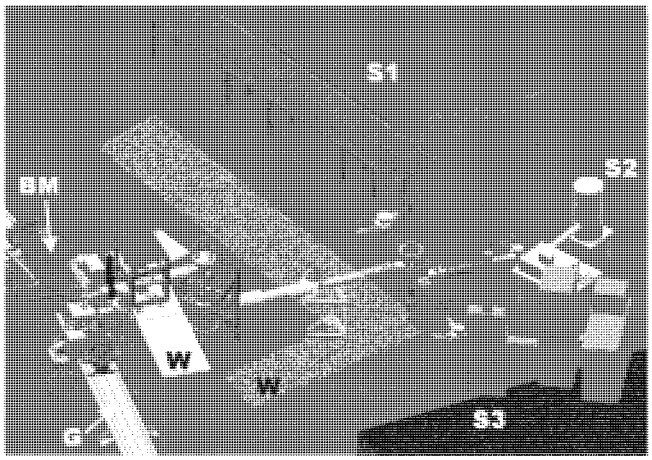

Fig. 4: 3D view of the IR beamline. - **BM:** storage ring magnets (left side), **G:** supporting girders, **W:** radiation shielding walls, **Sx:** the three spectrometers (right hand side).

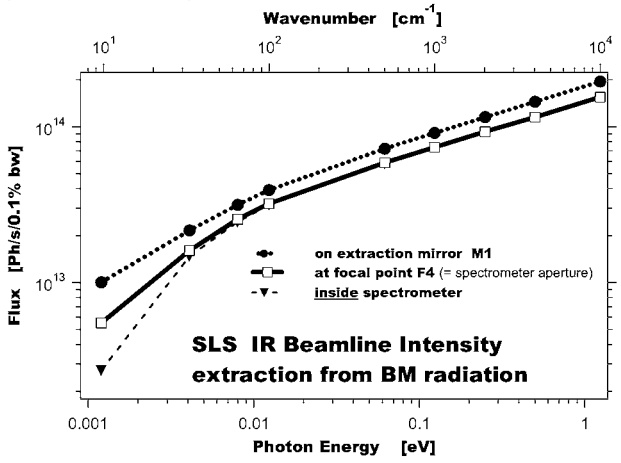

Fig. 5: Comparison of the extracted flux at the first mirror M1 (dots) with the propagated beam at last focal point F4 (squares) and with the flux inside the spectrometers (triangles).

Fig. 5 compares the extracted flux (dots) with the flux of the propagated beam at the last focal point F4 (squares), where the spectrometers expect the IR radiation, and finally with the flux inside the spectrometers (triangles). Only small losses in the propagated flux up to the spectrometer aperture at focal point F4 are observed. However, the relatively large beam sizes at low energies cause losses due to diffraction after having passed the spectrometer aperture.

The brightness of the beamline at the focal point F4 was calculated [1] using an analytical function, which describes the source best (i.e. diffraction limited at low wavelength / photon energies; increasing effect of the extended source at higher wavelengths). The result is displayed in Fig. 5.

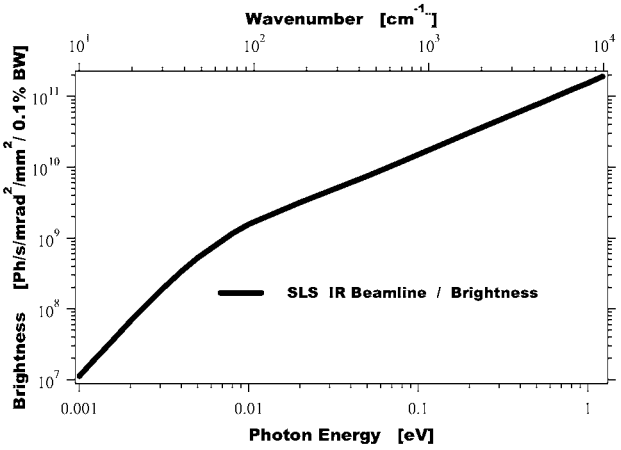

Fig. 6: The expected brightness calculated for the SLS IR beamline [1].

4. END STATIONS

Three FTIR spectrometers of different kind will be installed permanently at the beamline: an ultra-high resolving Bruker IFS125HR, a high resolving BOMEM DA8PC.3SCV and a research-type Bruker IFS66v/S. All spectrometers have a maximum optical range from < 4 cm^{-1} to 55000 cm^{-1}. The maximum resolution will be < 0.001 cm^{-1} for the Bruker IFS125HR, 0.004 cm^{-1} for the BOMEM DA8, and 0.1 cm^{-1} for the Bruker IFS66.

It is envisioned to upgrade the spectrometer in the near future with IR microscopes and with an IR ellipsometer. The beamline and the spectrometers have been designed so that user endstations or additional user's equipment can be mounted easily upon request.

5. TIME SCHEDULE

The beamline will be set-up in the second half of 2005. Regular user operation is envisioned to start in the beginning of 2006.

REFERENCES

[1] R. Reininger, *Scientific Answers and Solutions*, 5708 Restal St., Madison, WI 53711, USA.

THE STUDY OF GRAPHITE NEGATIVE ELECTRODES FOR LITHIUM-ION BATTERIES WITH THE HELP OF *IN SITU* X-RAY DIFFRACTION METHODS

A. Würsig, H. Buqa, W. Scheifele, M. Holzapfel, D. Goers, B. Schmitt, J. Vetter, P. Novák

In situ x-ray diffraction was performed on graphite used as negative electrode material in lithium-ion batteries. The influence of the electrolyte and the conducting salt on the stability of different types of graphite is shown.

INTRODUCTION

Graphite is widely used as negative electrode material in lithium-ion batteries because of its highly reversible specific charge of 372 $mAhg^{-1}$. The nature of the electrolyte strongly influences the cycling stability of the graphite. Ethylene carbonate (EC) permits reversible lithium intercalation by the formation of a stable passivating layer (Solid Electrolyte Interphase, SEI). But also the crystallinity and morphology of the surface as well as the nature of the surface group chemistry of polycrystalline graphite affect the stability of a graphite electrode [1]. These properties can be controlled, e.g., by thermal treatment of the graphite. In this study a non-treated graphite (TIMCAL SLX50), with a BET specific surface area of 4.0 m^2/g and a rhombohedral fraction of 23%, and a heat-treated one (TIMCAL SLX50-HT; BET: 2.6 m^2/g, rhombohedral fraction: 0%) are compared. The heat-treatment was done for two weeks at above 2500°C under inert gas. For comparison a natural graphite sample (Graphite A) with a BET specific surface area of 4.9 m^2/g and a rhombohedral fraction of 39% will be shown.

RESULTS AND DISCUSSION

Electrochemical experiments show that in the case of SLX50 a protective SEI film is formed on the graphite surface, whereas in the case of SLX50-HT the electrolyte is continuously reduced and no stable passivating layer is formed on the graphite surface. Hence, no lithium can be reversibly intercalated. The different intercalation behaviour should be reflected in a difference in the *in situ* x-ray patterns of the respective materials during the electrochemical cycling. Indeed, as can be seen in Fig. 1, in the case of Graphite A (which behaves comparably to SLX50) the (002)-peak shifts to the left. This indicates the insertion of lithium into the host structure of the graphite under expansion of the lattice. For SLX50-HT, however, the position of the (002)-peak remains unchanged until 200 mV vs. Li/Li^+. This proves that the consumed charge did not result in the intercalation of lithium into graphite, but was consumed due to the reduction of the electrolyte. Upon heat-treatment the number of surface defects diminishes which reduces the reactivity of the electrolyte with the surface. Hence, the co-intercalation of the solvent molecules into the graphite along with lithium can compete with reductive formation of the surface SEI film, and exfoliation occurs upon the reduction of the co-intercalated solvents [1].

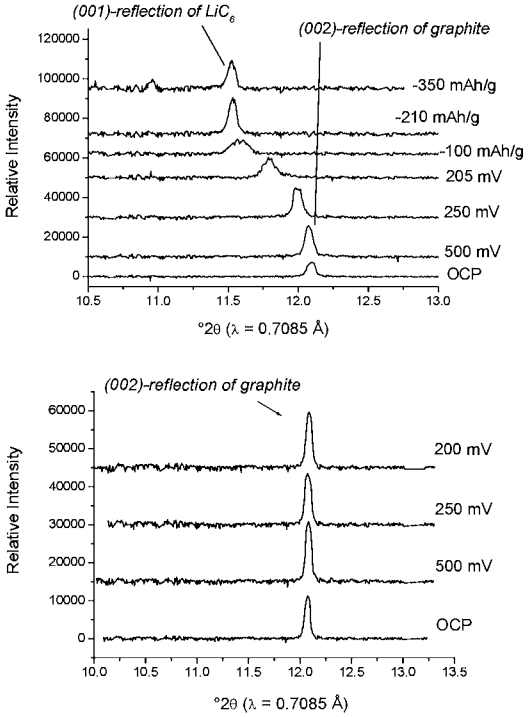

Fig. 1: *In situ* synchrotron x-ray diffraction patterns of Graphite A (top) and SLX50-HT (bottom). Electrolyte: EC:DMC (1:1), 1M $LiPF_6$.

Further, the influence of the electrolyte salt on the cycling behaviour of the graphites was studied *in situ* for SLX50-HT in EC:DMC (1:1), 1M $LiClO_4$. We found that lithium intercalation into the graphite matrix is possible in this case. The different behaviour is due to the different reduction mechanism with $LiClO_4$ compared with $LiPF_6$, which permits the formation of a passivation film in this case, in spite of the lower reactivity of the heat-treated graphite.

ACKNOWLEDGMENTS

M. Morcrette, LRCS Amiens (France), is acknowledged for his valuable aid in the preparation of the plastic cells and M. Spahr, TIMCAL Ltd. (Bodio), for providing graphite samples.

REFERENCE

[1] M. E. Spahr, T. Palladino, H. Wilhelm, A. Würsig, D. Goers, H. Buqa, M. Holzapfel, P. Novák, J. Electrochem. Soc. **151**, A1383 (2004).

Paul Scherrer Institut, 5232 Villigen PSI, Switzerland
Tel. +41 (0)56 310 21 11, Fax +41 (0)56 310 21 99
www.psi.ch